# Effect of Polar Structure on Photocatalytic Properties of Oxide Powders and Films

**Yaqiong Wang**

**Submitted in partial fulfilment of the requirements of the Degree of Doctor of Philosophy**


**School of Engineering and Materials Science,**

**Queen Mary, University of London**

**London, United Kingdom**

**September 2018**

## Declaration

I, Yaqiong Wang, confirm that the research included within this thesis is my own work or that where it has been carried out in collaboration with, or supported by others, that this is duly acknowledged below and my contribution indicated. Previously published material is also acknowledged below.

I attest that I have exercised reasonable care to ensure that the work is original, and does not to the best of my knowledge break any UK law, infringe any third party's copyright or other Intellectual Property Right, or contain any confidential material.

I accept that the College has the right to use plagiarism detection software to check the electronic version of the thesis.

I confirm that this thesis has not been previously submitted for the award of a degree by this or any other university.



Yaqiong Wang

September 2018

## Acknowledgement

Firstly, I would like to give special thanks to my supervisor, Dr. Haixue Yan, for his invaluable guidance and support during my Ph D study. His passion for research, critical thinking and professional character has inspired me a lot and taught me how to become a qualified researcher. Secondly, I would like to thank my co-supervisor, Pro. Steve Dunn, for giving me the fabulous opportunity to start my Ph D study under his guidance. The research skills and logical thinking I learnt from him will benefit me all my life. I also want to express my appreciation to my second supervisor, Dr. Joe Briscoe, for his brilliant suggestions and caring support both in the lab and in the thesis writing.

My sincere thanks also go to Dr. Rory Wilson, Mr. Russell Bailey, Mr. Maurizio Leo and Dr. Armando Lacerda, who helped me in materials characterisation and lab work. Further more, I would like to thank my colleagues and friends, for their help, support and encouragement in the past four years.

I also would like to thank Chinese Scholarship Council for providing me with financial support for my PhD program.

My final and great thanks go for my family, for their endless love, understanding and support during my Ph D study. I also would like to give my special thanks to my husband, Ye Zhang, who is also finishing his Ph D study this year. We went through ups and downs all together in the past four years, it is his love and companionship that makes the Ph D life in UK such a wonderful and unforgettable experience.

## Abstract

Semiconductor photocatalysis has gained increasing research interests in the application of solar fuel production and wastewater treatment. A key challenge for these applications is to reduce the photogenerated charge carrier recombination losses. Materials with polar structure such as the ferroelectrics are promising to address this challenge owing to the efficient separation of charge carriers by the internal electric filed present in ferroelectric materials. In this thesis, the composition and ferroelectric effect on the photocatalytic properties of $BiFeO_3$ and $Ba_xSr_{1-x}TiO_3$ have been investigated.

$BiFeO_3$ thin films were synthesized and employed as photoelectrodes for photocatalytic studies. Fundamental studies have been carried out to understand the complex nature of $BiFeO_3$ and the corresponding photocatalytic performance. A bias-dependent switchable photocurrent direction in $BiFeO_3$ thin films was observed. The $BiFeO_3$ photoelectrode exhibits either cathodic or anodic photocurrents depending on the applied bias, presenting both the characteristics of p and n type semiconductor photoelectrodes. This phenomenon was attributed to the specific bandgap structure of the as-prepared $BiFeO_3$, in which the depletion region can arise following both upward and downward band bending at the electrode/electrolyte solution interface. Determination of the bandgap structure of $BiFeO_3$

photoelectrodes from its photoelectrochemical (PEC) performance suggests strategies for probing semiconductor electronic structure by PEC method and provides fundamental insight on understanding of the switchable photocurrent direction in semiconductor photoelectrodes with Fermi level position not close to the conduction/valence band edges.

Meanwhile, $Bi_2Fe_4O_9$, one of the parasitic phases of $BiFeO_3$, has been found to be a promising photoelectrode material with high visible light photocatalytic activity and good stability for the first time when conducting study of the compositional effects on bismuth ferrite. Phase pure $Bi_2Fe_4O_9$ (Indirect $E_g \sim 2.05$ eV) thin films have been prepared by the chemical solution deposition (CSD) method. It shows a photocurrent of 0.1 mA/cm$^2$ at 1.23 V vs NHE under simulated AM1.5G illumination and 0.05 mA/cm$^2$ under visible light ($\lambda > 420$ nm). The addition of $H_2O_2$ as a hole scavenger increased the photocurrent to 0.25 mA/cm$^2$ under full AM1.5G illumination, indicating hole injection is one limiting factor to the performance.

Single-domain $Ba_xSr_{1-x}TiO_3$ powders were prepared to further demonstrate the effect of ferroelectricity free from the domain wall contribution. Two compositions of $Ba_xSr_{1-x}TiO_3$ powders, $Ba_{0.2}Sr_{0.8}TiO_3$ and $Ba_{0.8}Sr_{0.2}TiO_3$ were obtained by molten salt method and their composition, structure and photocatalytic activity have been

investigated. Photodegradation of organic dye molecules has been carried out to evaluate the photocatalytic activity of the $Ba_xSr_{1-x}TiO_3$ powders. The results showed that $Ba_{0.8}Sr_{0.2}TiO_3$ with polar structure has a degradation rate of almost twice of that of $Ba_{0.2}Sr_{0.8}TiO_3$ with non-polar structure, demonstrating that the internal electric field resulting from the ferroelectric polarization can speed the photoexcited charge carrier separation and improve the photocatalytic efficiency.

This research reveals the characteristic photocatalytic behaviors of the Bismuth- and Barium-related perovskite structure materials, which will benefit the future work on ferroelectric photocatalysts.

# Table of Contents

Table of Contents

## List of Figures

# List of Figures

## List of Tables

# Chapter 1 Introduction

## 1.1. Background

Development of renewable energy resources is one of the most important tasks in this century for human beings, due to the global depletion of fossil fuels, increasing energy demand and the environmental concern. Solar energy is the most abundant and clean renewable energy resource from nature, and how to convert and store it as other energy forms such as chemical or electrical energy has received tremendous attention in the past decades[1].

Semiconductor materials have been utilized as photocatalysts for harvesting solar energy, which can transform absorbed solar energy into excited charge carriers. When a semiconductor is under solar light illumination, electrons can be excited from the valence band to the conduction band, leaving holes with the equal number in the valence band. The photoexcited electrons and holes will have a chance to migrate to the semiconductor surface and conduct redox reactions with adsorbates molecules from the outside environment. Different products can be obtained from this procedure depending on the species reacted with the photoexcited charge carriers. For example, solar fuels like

hydrogen can be obtained by water splitting and hydrocarbon can be obtained by $CO_2$ reduction. In addition, for the application of photodegradation of organic dyes, the dye molecules can be oxidized or reduced to degrade to smaller molecules. Despite the electrons and holes migrated to the semiconductor surface, there will be a high chance for them to recombine with each other in the bulk before reaching the surface. This part of energy will be lost by a form of heat or emitted light.

Charge recombination losses during solar energy conversion procedure has been a key challenge for the improvement of light utilization efficiency. To minimize the charge recombination losses after light absorption, different methods such as the use of heterojunctions and electric fields have been introduced to the photocatalysts to create band bending/polar fields to speed the photoexcited charge carrier separation inside the catalysts and drive photoexcited carriers to different surface sites of the photocatalysts. One route to achieve this is to use ferroelectric materials, the polar structure of which can create internal electric field within the material and speed the photoexcited charge carrier separation.

A ferroelectric material possesses a polar structure, in which spontaneous polarization is produced by the displacement of individual positive and negative charges in the crystal

structure. The spontaneous polarization induces the internal electric field and surface band bending, which can have a significant influence on the migration of photoexcited charge carriers. Photoexcited electrons and holes will be driven to opposite directions under the force of the internal electric field, and migrate to separate surface sites for the later reactions. The surface band bending can act as thermal barriers which can further inhibit electrons and holes recombination. The unique property of ferroelectric material has aroused increasing interest for their application in solar energy conversion. Investigation of photocatalytic performance of the ferroelectric material and a fundamental understanding of the influence from ferroelectric polarization are expected to contribute to the development of next generation photocatalysts.

## 1.2. **Thesis Structures**

This thesis has 7 chapters and they can be summarised as below:

Chapter 1: This chapter is an introduction to the research background and a summary of the thesis structures.

Chapter 2: This chapter is the literature review. It gives an overview of the semiconductor

photocatalysis and the application of ferroelectric materials as photocatalysts. The history, basic principles and characterisation of semiconductor photocatalysis have been reviewed. The definition of ferroelectric materials and their unique properties benefitting the application in photocatalysis have been reviewed. 3 materials used in the research has been introduced and the aim and objectives of this research have been justified.

Chapter 3: This chapter gives the details of material synthesis and characterisation methods used in this work.

Chapter 4: This chapter investigates origin of the switchable photocurrents in the as-prepared $BiFeO_3$ film electrode. The PEC performance and band diagram of the $BiFeO_3$ film have been studied. The relationship between the band diagram and switchable photocurrents has been investigated and explained. The specific Fermi level position of the $BiFeO_3$ film is believed to lead to the switchable photocurrent under different applied bias.

Chapter 5: This chapter reports a novel photoanode material – $Bi_2Fe_4O_9$, which shows high visible light photoresponse. The PEC performance and band structure of the $Bi_2Fe_4O_9$ have been studied. The as-prepared $Bi_2Fe_4O_9$ film has a narrow band gap with

the band positions straddling the reduction and oxidation potential of water, making it a good candidate material for overall water splitting reaction.

Chapter 6: This chapter investigates the effects of ferroelectricity on photocatalytic activity of single grain single domain $Ba_xSr_{1-x}TiO_3$ (x = 0.8, 0.2 ) powders. The structure, composition and optical properties of the as-prepared barium strontium titanate powders have been studied. The polar structure dependence on grain size of the powders and temperature has been investigated to confirm the two samples used for studying the effect of ferroelectricity on photocatalytic activity are polar and non-polar structure respectively. The advantage of the polar structure on photocatalytic performance has been discussed.

Chapter 7: This chapter gives a summary of conclusions and suggests future work that can be done to further the current research work.

# Chapter 2 Literature Review

## 2.1. Semiconductor Photocatalysis

### 2.1.1. Overview and history

The diminishing supply of fossil fuels and growing environmental problems is becoming a more and more serious challenge. Developing and utilization of the sustainable and renewable energy resources is one of the most important tasks for scientific researchers nowadays. As a clean, reliable and renewable source of energy, solar energy has gained extensive attention for its promising application as the next generation energy resource.

To absorb, transfer and store the energy from the sun, it calls for specific materials that can work as the energy transformation media. Inspired by photosynthesis, people have been pursuing materials that can work like a plant, converting and storing solar energy into chemical bonds and/or electricity. The first breakthrough was reported by Fujishima and Honda in 1972[2]. They demonstrated that it is feasible to conduct photo-assisted water splitting using an n-type $TiO_2$ photoelectrode by band-gap excitation. $H_2$ can thus be produced from water splitting. In 1979, photocatalytic reduction of $CO_2$ to organic hydrocarbon compounds was reported by the same group[3]. Later it was found that $TiO_2$

can also be used to degrade organic dye pollutants in wastewaters[4]. However, $TiO_2$ has a large band gap of 3.2 eV and can only absorb ultraviolet (UV) light that is < 5% of solar light, resulting in a low theoretical solar energy conversion efficiency[1]. Significant efforts have been made since then to find out the candidate materials or material systems with visible-light activity to achieve higher efficiency in the applications of hydrogen production from water splitting, hydrocarbon generation by photoreduction of $CO_2$ and wastewater treatments[1,5,6]. The study of semiconductor photocatalysis has provided new avenues to produce sustainable solar fuel and solve environmental problems by making use of the expansively available sunlight.

### 2.1.2. Electronic band structure of semiconductors

The concepts of the band model is developed in order to describe electron transfer to or from a solid electrode. The band model of solids stems directly from the picture of atomic energy levels. A band is composed of a continuum of energy levels from atomic orbitals[7]. The orbitals occupied by the valence electrons is called the valence band (VB) and the band associated with the first excited state, normally unoccupied by electrons, is called the conduction band (CB)[8]. The energy gap between the lower edge of the conduction band and the upper edge of the valence band is defined as band gap ($E_g$)[7].

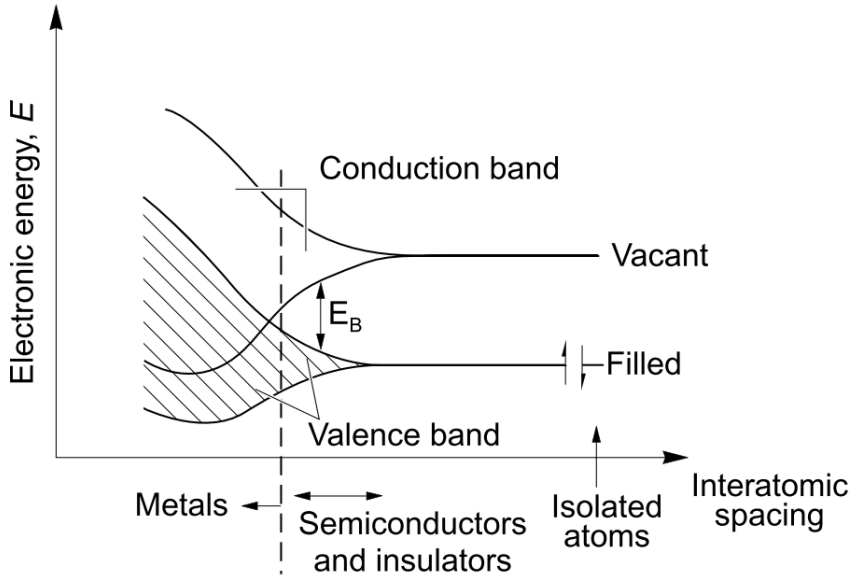


**Figure 2.1 The band model of solids[9].**

Conductivity of a solid requires the conduction band being partially occupied. This can be realized by promoting electrons from the valence band to the conduction band. In insulators, the band gap is too large for electrons to be promoted. While in metals, the conduction and valence bands overlap and the conduction band is readily occupied. If the band gap is within a certain range, the material is defined as semiconductors, in which the electrons can absorb external energy and be excited to the conduction band. A schematic view of the band model of solids is shown in Figure 2.1.

The Fermi energy and the Fermi-Dirac distribution are used to accurately describe the distribution of electrons and holes in a solid. The Fermi function *f*, which is defined as

the probability that a level at energy $E$ is occupied by an electron[8], is given by:

$$f = 1/[1+ \exp(E - E_F)/kT] \qquad \text{Eqn (2.1)}$$

where $E_F$ is the Fermi energy, $k$ is the Boltzman constant, and $T$ is the temperature. If the energy level $E$ is at the Fermi energy, the probability of occupancy is exactly 50%, according to equation 2.1.

The position of the Fermi energy can be varied dependent on the concentration of electrons and holes in the semiconductor. In an intrinsic semiconductor, electron concentration in the conduction band is equal to hole concentration in the valence band, so the Fermi energy is in the middle of the band gap (Figure 2.2a). In an extrinsic semiconductor, the carrier concentration can be changed by the doping level and one type of carriers will predominate, thus the Fermi energy moves depending on the majority carriers. An n-type semiconductor is defined as in which electrons are the majority carriers, with the Fermi level more close to the conduction band (Figure 2.2b). And a p-type semiconductor has holes as the majority carriers, with the Fermi level more close to the valence band (Figure 2.2c).

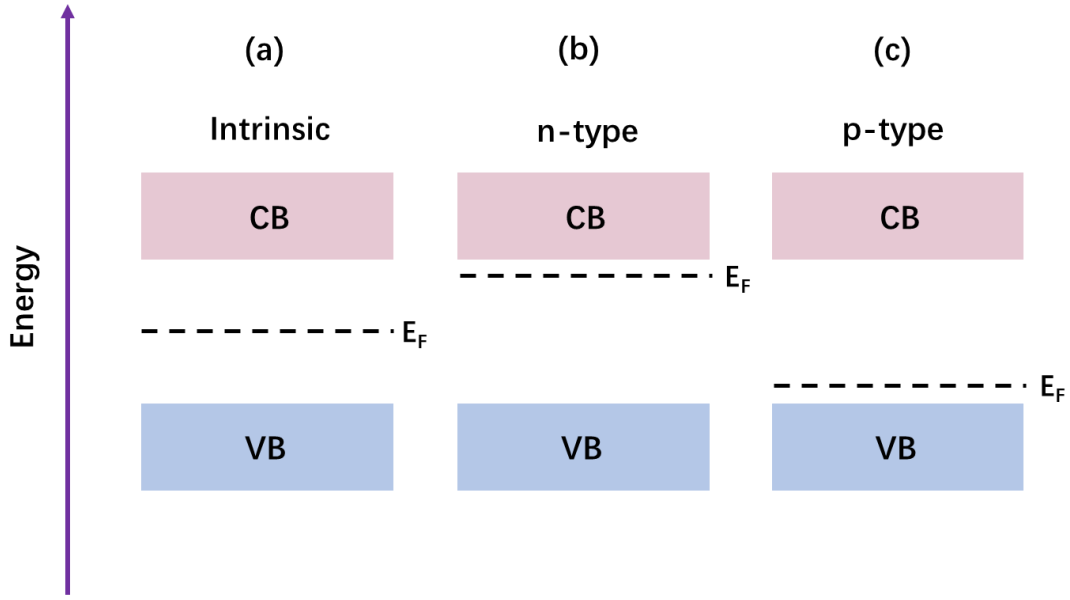


**Figure 2.2 Fermi energy of intrinsic semiconductor (a) and extrinsic semiconductor (b) n-type and (c) p-type.**

### 2.1.3. Basic principle for semiconductor-based photocatalysis

The fundamental steps in the photocatalysis procedure can be summarized as: charge generation by photo absorption, charge separation and redox chemistry at the interface. As shown in Figure 2.3, under illumination, electrons in valence band can be promoted to the conduction band and leave mobile holes in the valence band. The photogenerated electrons and holes will have several pathways to go, as depicted in the scheme. They can either migrate to the surface, or recombine in the bulk. Those arrived to the surface can take part in the redox reactions, while there's still a big chance for them to recombine at

the surface simultaneously. Recombination of the photogenerated electrons and holes will loss the absorbed photoenergy as heat or light, which will significantly limit the photocatalytic efficiency.

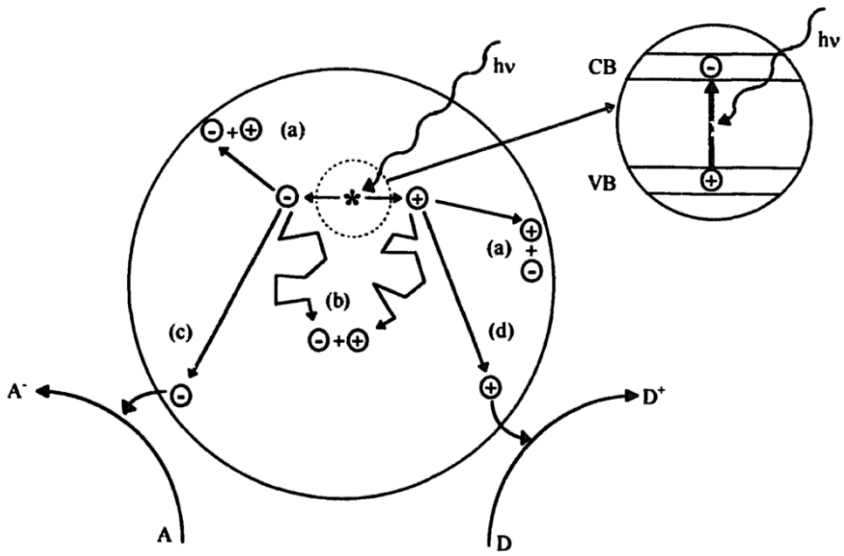


**Figure 2.3 Schematic illustration showing the photocatalysis procedure in a semiconductor. (a) Charge carrier recombination at the semiconductor surface (b) Charge carrier recombination in the semiconductor bulk. The electrons and holes will take part in the redox reactions at the surface, shown in (c) and (d). A is an electron acceptor and D is an electron donor[10].**

### 2.1.4. Photochemistry on the semiconductor surface

The photochemical process, which happens near/on the surface of the photocatalysts, is the pivotal part of the whole photocatalytic procedure. The study of photochemistry

involves that of: (1) the energy levels in the semiconductor and electrolyte solution, (2) junction formation at the semiconductor/electrolyte interface, and (3) the light absorption and charge transport.

#### 2.1.4.1. The energy levels in the semiconductor and electrolyte solution

Understanding the energy levels in the semiconductor and electrolyte solution is of importance before further study of the system performance under illumination. The electrochemical potential of electrons is determined by the Fermi level in the semiconductor and that of the electrolyte solution is determined by the redox potential of the redox couples present in the electrolyte. Generally, an energy diagram is used to give the energy levels information of electrons in solids and their relation to redox couples in the solution. Figure 2.4 is a schematic of the semiconductor band diagrams presented against the vacuum level and the normal hydrogen electrode. The energy scale in Figure 2.4 uses the vacuum level and the normal hydrogen electrode (NHE) as a reference. They are the two common energy scales used in chemical physics. In the vacuum scales of energy, the zero energy is the energy of an electron at infinity, and in electrochemistry, the zero energy is the Fermi energy of the hydrogen reference electrode under standard conditions[11]. The hydrogen reference electrode energy is considered to be very close to

4.5 eV below the vacuum level. The two energy scales are usually used together to give a clear description of the semiconductor and electrolyte solution energy levels.

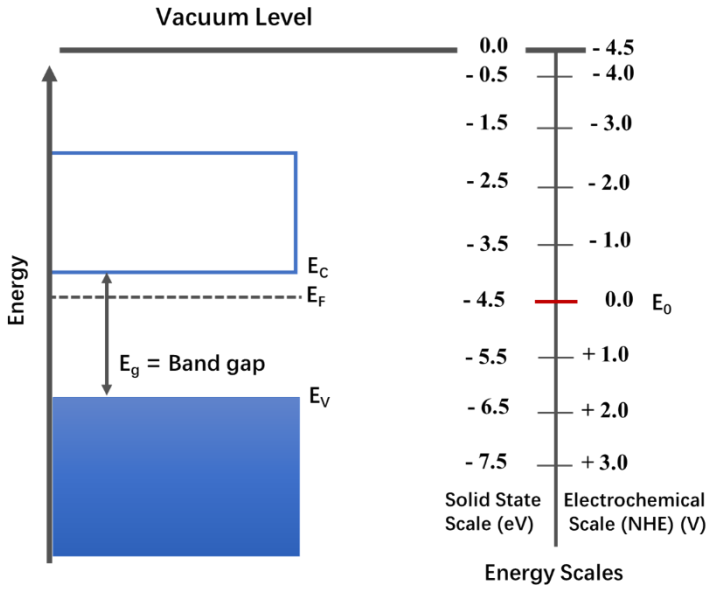


**Figure 2.4 Schematic illustration of the semiconductor band diagrams presented against the vacuum level and the normal hydrogen electrode. ($E_c$ is conduction band, $E_v$ valence band, $E_F$ the Fermi level, $E_g$ the band gap, $E_0$ the energy of a free electron at the $H_2$ redox potential)[12].**

### 2.1.4.2. Junction formation at the semiconductor/electrolyte interface

When a semiconductor comes into contact with an electrolyte solution, electrons will transfer in or out the semiconductor to make their electrochemical potential be the same between the two phases. An equilibrium will then be reached at the semiconductor/electrolyte interface. Resulting from charge transfer, an excess of charges

will locate adjacent to the semiconductor surface and form a charge region called the space charge region, the width of which is about 100-1000 Å. Band bending at the semiconductor surface will arise simultaneously with the formation of the space charge region.

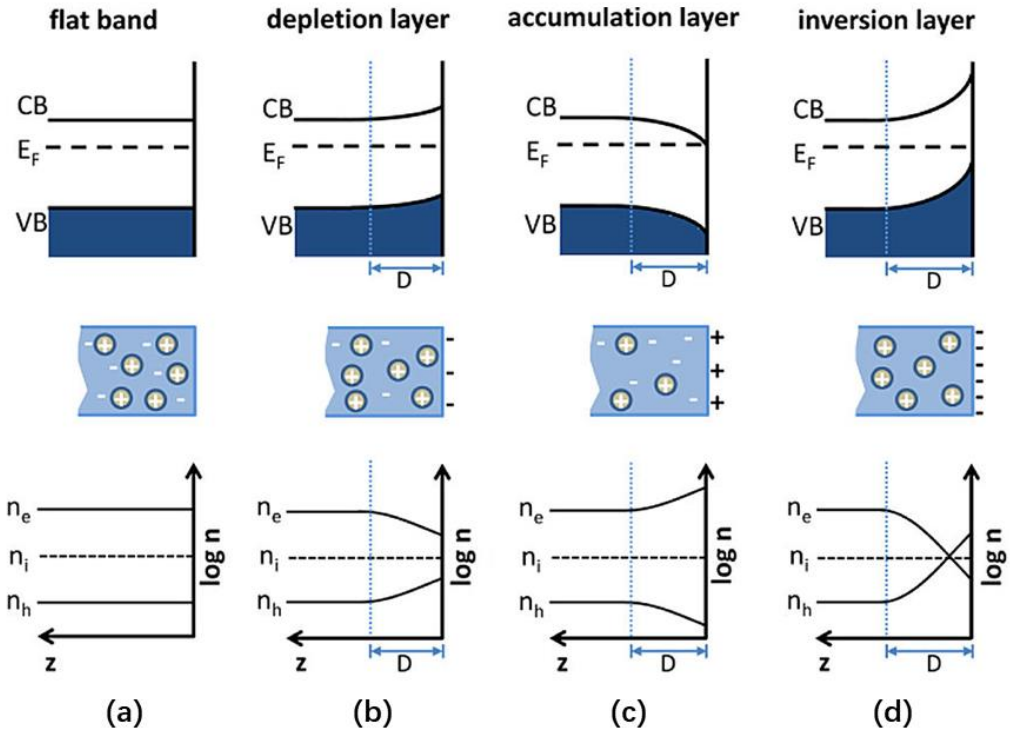


**Figure 2.5 Schematic diagrams of the energy levels and charge densities from an n-type semiconductor surface to the bulk. *D* is the width of the space charge region, $n_e$ is free electron density, $n_h$ is free hole density and $n_i$ is intrinsic carrier density[13].**

If taking an n-type semiconductor as the example, the space charge region of three forms

can be presented in the following schematic diagrams (Figure 2.5). The three forms of space charge region are named as depletion region (Figure 2.5b), accumulation region (Figure 2.5c) and inversion region (Figure 2.5d), respectively. They are used to describe the band bending at the semiconductor/electrolyte solution interface and give out the information of the charge carriers in the space charge region. For an n-type semiconductor, its Fermi level is normally above the electrolyte solution redox potential (typically the water redox potential). Thus the equilibrium between the two phases can be reached by transfer of electrons from the semiconductor to the electrolyte solution and this produces a positive space charge region in the semiconductor, which is named the depletion region because the surface region is 'depleted' of the majority carriers. Correspondingly, the conduction and valence band edges will bend and a potential barrier will be formed to stop further electron transfer into the electrolyte, as shown in Figure 2.5b. The other situations can occur when the semiconductor works as an electrode in a PEC cell, where bias can be applied to shift the semiconductor Fermi level and thus the associated space charge region type.

When the applied potential drives the Fermi energy of the semiconductor equal to the electrolyte solution redox potential, there will be no band bending at the semiconductor surface. This potential is termed as the flatband potential, $E_{fb}$. This is illustrated in Figure

2.5a. When a potential positive of the flatband potential is applied to the semiconductor, the Fermi level will shift positively with the upward band bending arising at the surface. The depletion region arise. If, the applied bias is sufficiently large and drives the Fermi level below the intrinsic level ($n_i$), electrons will be extracted from the valence band, the space charge region will become an inversion layer then (as shown in Figure 2.5d). When a potential negative of the flatband potential is applied to the semiconductor, an excess majority charge carrier (electrons) will be injected into the space charge region, an accumulation region will be formed, this is the situation in Figure 2.5c. An inverse but analogous situation goes for a p-type semiconductor.

Under dark conditions (no illumination), when the semiconductor and the electrolyte solution achieve equilibrium and the depletion layer is formed near the semiconductor surface, there will be few charge carriers available for charge transfer. But if an accumulation layer is formed under applied bias, the semiconductor electrode will behave as a metallic electrode, since an excess of majority charge carrier exists.

#### 2.1.4.3. Light absorption and charge transport

The light absorption and charge transport procedure can be well revealed from the I-V curve of a semiconductor photoelectrode, which is the plot of the current density vs

applied bias. A typical I-V curve for an n-type semiconductor electrode in the dark and under illumination is presented in Figure 2.6. It is composed of three regions depending on the applied bias. At bias negative of the flatband potential (Region I), currents will be generated no matter under dark or illumination due to the existence of the accumulation layer. The electrode acts as a cathode in this case. At bias equal to the flatband potential, there will be no current either under dark or illumination (Region II). At bias positive of the flatband potential (Region Ⅲ), there will be no current under dark and photocurrents will be generated under illumination. In this situation the depletion layer exists and the electrode works as a photoanode, with holes moving to the interface and electrons extracted from solution species.

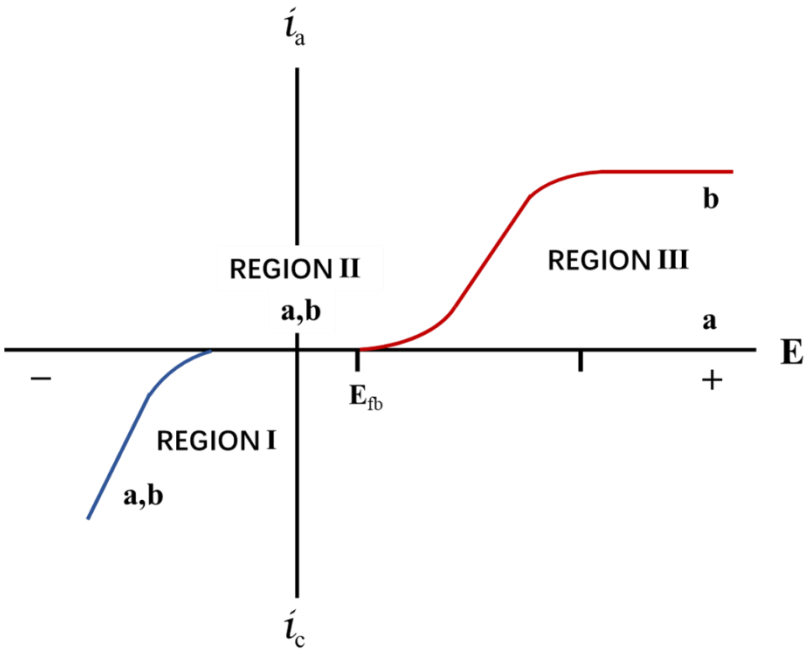


**Figure 2.6 Typical I-V curves for an n-type semiconductor (a) in the dark and (b) under illumination. $i_a$ is anodic current density, $i_b$ is cathodic current density[7].**

### 2.1.5. Main factors affecting photocatalytic efficiency

Photocatalytic efficiency refers to the overall solar-to-current or solar-to-chemical conversion efficiency[14]. The solar-to-current conversion efficiency for photo(electro)catalytic systems is usually assessed by two calculations: the applied-bias photo-to-current efficiency (ABPCE) and the incident photo-to-current efficiency (IPCE)[15]. The solar-to-chemical conversion efficiency refers to the solar-to-hydrogen conversion efficiency (STH) in water splitting, while it can have other forms dependent

on the different chemicals obtained[15].

Both intrinsic and extrinsic factors can contribute to the photocatalytic efficiency. The intrinsic factors refer to the physical characteristics of semiconductor photocatalysts, and the extrinsic factors relate to the material characteristics that are inherited from the synthesis procedure and thus can be varied.

#### 2.1.5.1. Intrinsic factors

Intrinsic factors include mainly three aspects. The first is the band-gap energy of the photocatalysts. The light absorption ability of a photocatalyst is determined by its bandgap. If the absorption spectrum of a photocatalyst is large, it will be able to absorb more sunlight and improve the conversion efficiency. As a result, it requires a photocatalyst to have smaller band gap, that is to say, a wider light absorption spectral range. The bandgap of a semiconductor should be smaller than 2.35, 2.11 or 1.93 eV, to achieve an theoretical efficiency of 10 %, 15 % or 20 %, respectively[14]. Figure 2.7 is an illustration of the theoretical maximum solar-to-hydrogen (STH) efficiency dependent on the semiconductor band gaps[1].

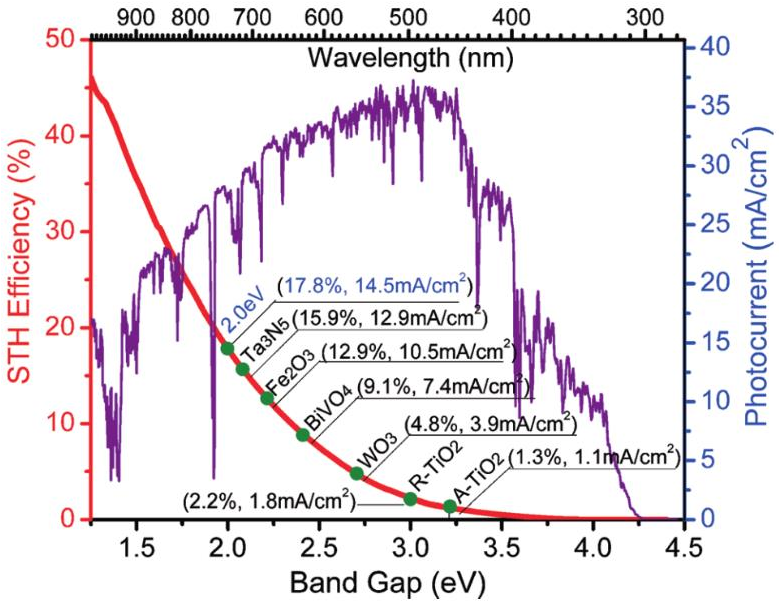


**Figure 2.7 Illustration of the STH efficiency and photocurrent density of photoelectrode dependence on the band gap[1].**

Secondly, the band edge positions of the photocatalyst need to be appropriate in order to carry out effective reduction/oxidation reactions with the target chemicals, which means the CB and VB edges should straddle the redox potential of the photocatalytic reaction. That is, in the water splitting reaction, the CB edge needs to be higher than the water reduction potential and the VB edge need to be lower than the water oxidation potential to promise the overall water splitting. A schematic example of a photocatalyst with preferable bandgap structure for water splitting is shown in Figure 2.8. The band edge positions of some representative semiconductors are shown in Figure 2.9.

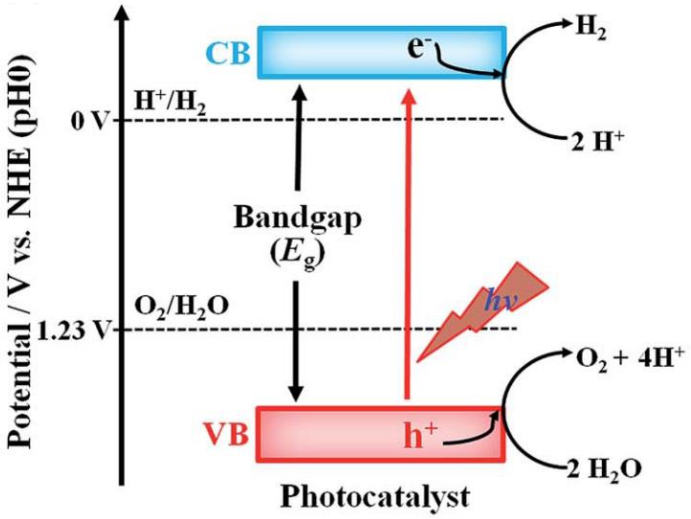


**Figure 2.8 Energy diagram of a semiconductor photocatalyst capable of conducting unassisted-water splitting[16].**

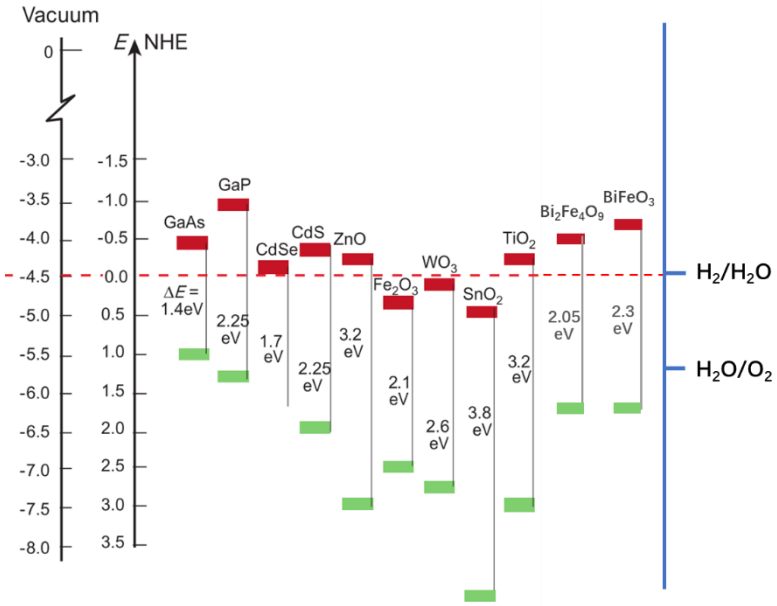


**Figure 2.9 Band positions of several representative semiconductors with the energy scale against the normal hydrogen (NHE) and the vacuum level as a reference[17].**

The third intrinsic issue limiting photocatalytic efficiency is the recombination of photogenerated charge carriers. Recombination can happen both in the bulk and on the surface of the semiconductor. The photoenergy will be lost in the form of heat or light if electrons and holes recombine with each other, which is unfavorable for photocatalysis. Charge recombination is related to the intrinsic carrier diffusion length of the semiconductor, $L_D$, which is a function of the charge mobility $\mu$, and the carrier lifetime $\tau$:

$$L_D = (kT\mu\tau/e)^{0.5} \qquad \text{Eqn (2.4)}$$

Reported $L_D$ values of typical semiconductor photocatalysts range from a few nanometers (such as $Fe_2O_3$[18] and $TiO_2$[19]) to a few tens of nanometers (such as $BiVO_4$[20]), thus they usually suffer from a high recombination rate[14].

The recombination issue can be mitigated by the use of internal electric field in photocatalysts[12]. Internal electric field exists in the p-n junctions, polar surface terminations, polymorph junctions and ferroelectric phenomena[12]. The electric fields presented in the first three sources originate from the energy level differences at phase boundaries and the last one arise from the spontaneous polarization in ferroelectrics. A schematic illustration of these internal field sources are shown in Figure 2.10.

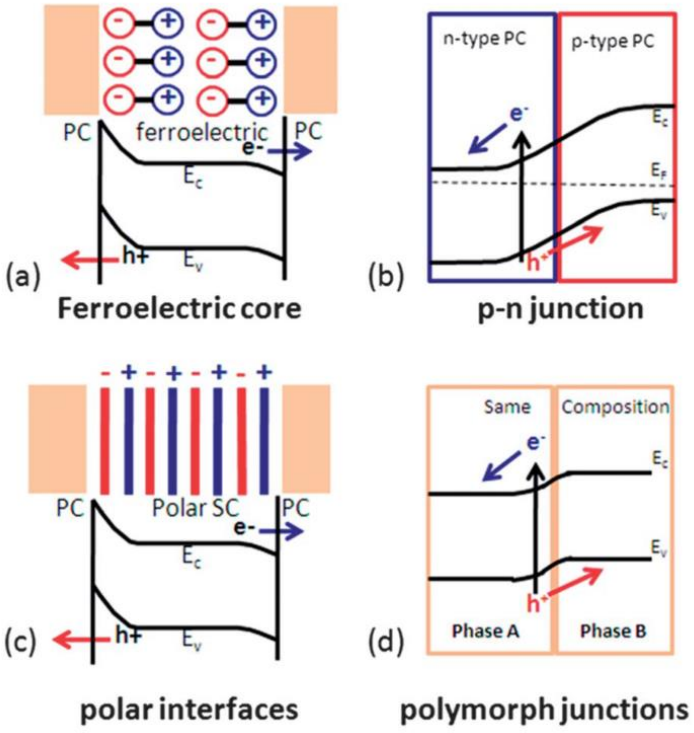


**Figure 2.10 The internal electric field in the photocatalysts which arising from: (1) Ferroelectric polarization (2) p-n junction (3) polar interfaces (4) polymorph junctions[12].**

### 2.1.5.2. Extrinsic factors

Extrinsic factors usually include the particle size, particle shape, crystallinity, defect structures and so on. Particle size determines the surface-to-volume ratio of the photocatalysts and can affect the reaction rate. In the photocatalytic procedure, the carriers will be firstly generated in the bulk and then migrate to the surface to carry out further catalytic reactions. Smaller particle sizes allow for a larger specific surface area and hence more reactive sites, and meanwhile a shorter carrier migrating distance from

the bulk to the surface, which is beneficial for the overall reaction rate. While from the perspective of the electronic structure, if the particle size is too small, sufficient space charge regions can not be generated at the semiconductor/electrolyte solution interface[21]. Thus, the electric field over the space charge region will be smaller in small particles[22].

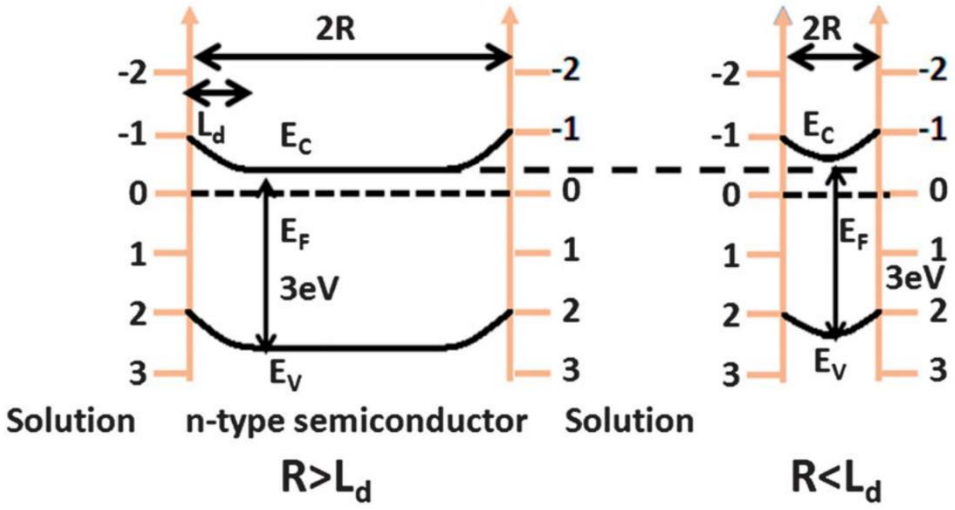


**Figure 2.11 Illustration of the band bending for an n type semiconductor in electrolyte solution. (a) R is larger than $L_d$ (b) R is smaller than the $L_d$[12].**

A schematic illustration of the band structure of two particles (supposed to be spherical particles) with the radius, R, smaller and larger than width of the space charge region, is shown in Figure 2.11[12]. Thus the particle size of a photocatalyst should be chosen as a compromise between the aforementioned pros and cons. A particle size around twice of the space charge region width of the particular semiconductor photocatalyst has been

suggested to be appropriate[12,21].

The shape of the photocatalysts also has an influence on the catalytic efficiency. The study of effects from catalysts shape can be grouped mainly to two kinds. The first focuses on the development of one-dimensional nanostructured photocatalysts such as nanorods, nanowires, nanosheets and so on. It has been demonstrated in several 1D nanostructured materials such as CdS[23], ZnO[24] and GaN[25] that increasing the aspect ratio can lead to an activity enhancement, possibly due to enhanced charge carrier transport from bulk to the surface along the axis directions[26]. The second relates to the reactivity difference of different facets of single crystals. One representative example is the work by Li *et. al*[27] on the selective deposition of oxidation and reduction products based on faceted $BiVO_4$ crystals. It was found that Pt (reduction) and $MnO_x$ (oxidation) were preferably loaded onto the {010} and {110} facets respectively, indicating that electrons and holes tending to migrate to different crystal facets. As a result, efficient charge separation can be achieved. Figure 2.12 shows SEM images of $BiVO_4$ crystals with the photo-deposited Pt and $MnO_x$ on different facets[27]. This phenomenon has been attributed to the electrochemical potential differences possibly existed on different surfaces/directions.

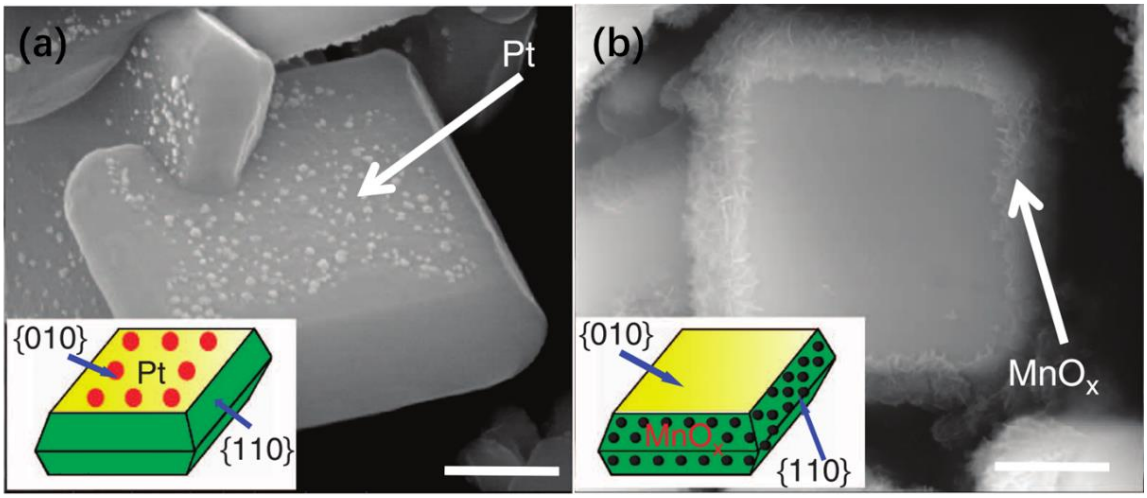


**Figure 2.12 SEM images of $BiVO_4$ with single metal/oxide deposited on different facets. (a) $Pt/BiVO_4$ (b) $MnO_x/BiVO_4$[27].**

The degree of crystallinity and associated defects content of the photocatalysts is another important factor. Crystal defects such as grain boundaries and dislocations can act as recombination centers of carriers and have an negative influence on the photocatalytic efficiency. Therefore, improved crystallinity is beneficial for improved bulk transport and reduced recombination in photocatalysts. Generally, prolonged thermal treatment can reduce the non-equilibrium defects and increase the crystallinity degree. However, this is usually accompanied by the growing of the particle and even phase transformation of the catalysts, which will in turn offset the advantage. For example, in the study of $TiO_2$, increasing the crystallinity of the anatase phase by post-annealing will cause the generation of the rutile polymorph phase which has lower reactivity[28,29]. Thus, it is

important to consider the effects of size, shape and crystallinity with caution when designing and processing the material/material systems for photocatalyst application.

### 2.1.6. Photocatalytic activity characterisation

Photocatalysts are normally in two forms, either films or powders. Film photocatalysts are usually applied as photoelectrodes in a PEC cell. Powdered photocatalysts are more commonly used for organic pollutants degradation. A brief illustration of how the two forms of photocatalysts take part in the photocatalytic procedure is presented in Figure 2.13.

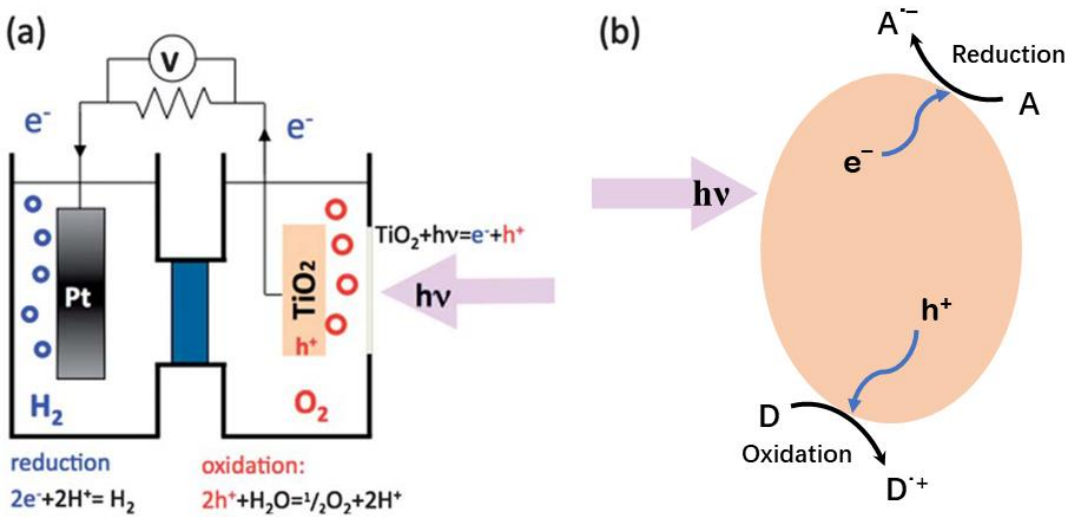


**Figure 2.13 Schematic illustration of (a) photoelectrochemical cell and (b) powdered photocatalysts[12].**

For film catalysts applied in a PEC cell, the most common method to assess the photocatalytic activity is to measure the photocurrent density. The amount of the produced chemical products (typically gases) can also be measured to give more accurate calculation of the solar to energy transformation efficiency. The mechanism of how a PEC cell works has been discussed in the last section. The photoexcited charge carriers can be separated in the depletion region efficiently, migrating to opposite directions and participating in the redox reactions separately on the surface of the working electrode and the counter electrode. An external bias can be applied on the working electrode, which can change the Fermi level position of the semiconductor and lead to more band bending and thus more driving force to separate the charge carriers.

Particulate photocatalysts are often used in photodegradation of organic dyes due to their high specific surface area. Organic dyes are one of the most common water pollutants from industry discharge due to their widely use in textiles, paper, cosmetics, food and many more applications. The dye degradation rate can reveal the activity of the photocatalysts. The photocatalytic dye degradation can be generally summarized as four steps: photoexcitation, ionization of water, oxygen ionosorption and protonation of superoxide. The mechanism of photocatalytic degradation of organic pollutants is shown as below. Taking $TiO_2$ as the photocatalyst and Rh B as the organic pollutant for the

example[30].

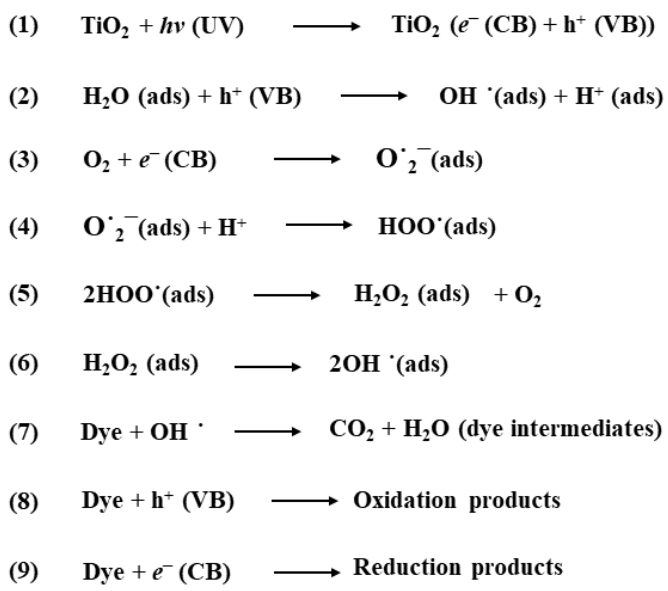


There are also other methods to study the photocatalytic performance of semiconductor photocatalysts, involving the gas phase pollutants for air treatment, photocatalytic disinfection, and photocatalysis for organic synthesis such as the photoreduction of $CO_2$ to hydrocarbon products[5,31]. The characterisation methods used in this study are the PEC cell and dye-degradation, thus we will give no detailed discussion of the other methods or applications here.

## 2.2. **Ferroelectric Materials**

### 2.2.1. Definition

The origin of ferroelectricity comes from the unique crystal structure. In the 32 point groups, 11 are centrosymmetric and thus cannot exhibit polar properties. Of the remaining 21 non-centrosymmetric groups, 20 classes are termed as piezoelectric crystals, which have the property that polarization can be induced under applied mechanical stress, and conversely, mechanical deformation can be produced with the application of an electric field. Among the 20 piezoelectric classes, 10 have a unique axis of symmetry (are polar)

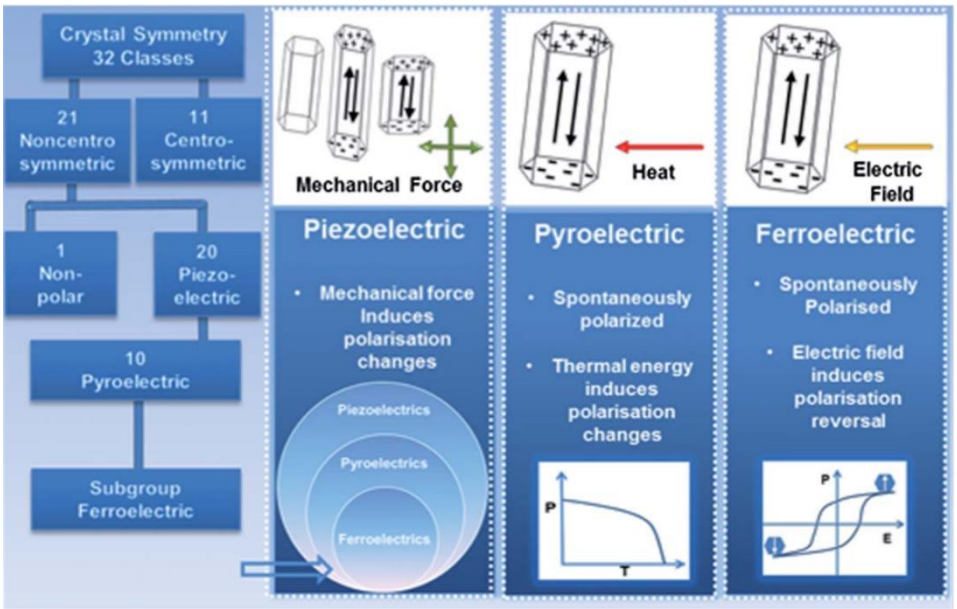


**Figure 2.14 Schematic illustration of piezoelectric, pyroelectric and ferroelectric materials[32].**

and electric polarization exists in the absence of an applied field (named spontaneous polarization). The spontaneous polarization in these polar materials changes with temperature, thus crystals belonging to these 10 classes are called pyroelectric materials. If the spontaneous polarization direction of a pyroelectric material can be reversed by the application of an electric field, this pyroelectric material is called ferroelectric. Figure 2.14 shows the relationship among piezoelectric, pyroelectric and ferroelectric materials.

A simple definition for a ferroelectric material is: A ferroelectric is a crystal that possesses reversible spontaneous polarization as exhibited by a ferroelectric hysteresis loop[33], and it can be characterised by three features: Curie Point ($T_c$), Spontaneous Polarization ($P_s$) and Domain Wall (DW).

### 2.2.2. FE Curie point

The spontaneous polarization in a ferroelectric material changes with temperature. It exists in the low-temperature non-centrosymmetric phase and disappears when transformed to a high-temperature centrosymmetric phase. The temperature at which the spontaneous polarization disappears is called the Curie Temperature, $T_c$. The relative properties of the ferroelectrics, such as the dielectric, thermal and elastic performances,

usually become abnormal around $T_c$.

Ferroelectric materials can have more than one phase transformation. For example, one of the most well-known ferroelectrics, barium titanite ($BaTiO_3$), has four phases with temperature change. Above $T_c$ (393 K), it has a cubic structure where there is no polarization. Below $T_c$ (393 K), it transforms to a tetragonal phase which has a polarization direction along the [100] direction. When it is cooled further, the phase will change to orthorhombic as it reaches ~ 278 K, with the polarization direction along [011]. And then the rhombohedral below 183 K, with the polarization direction along [111]. A schematic illustration of the phase transformation of $BaTiO_3$ with temperature is shown in Figure 2.15, together with the dielectric permittivity change.

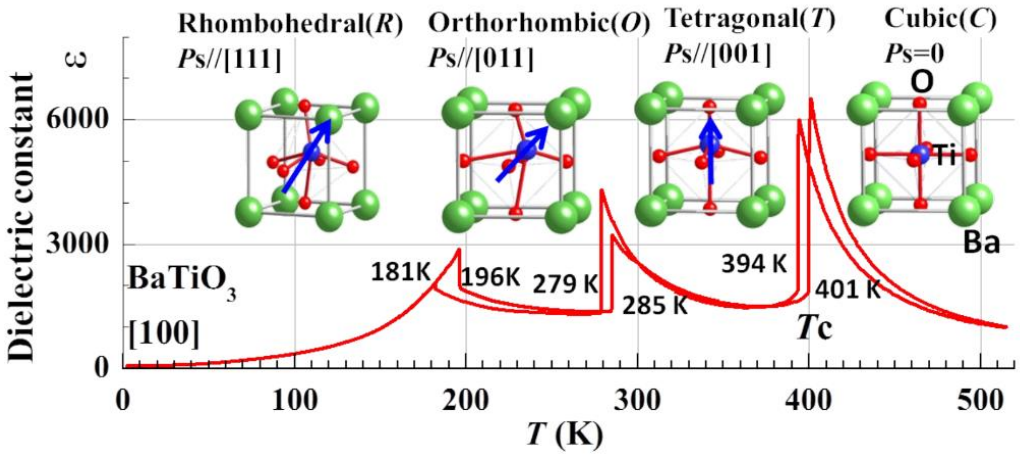


**Figure 2.15 Schematic of $BaTiO_3$ phase transformation with temperature.**

### 2.2.3. Spontaneous polarization and screening

Spontaneous polarization is the key characteristic feature of a ferroelectric. It comes from the displacements of individual positive and negative charges in the crystal structure of a ferroelectric material. Take $BaTiO_3$ as the example to introduce the polarization effect. The schematic graph of two $BaTiO_3$ crystal structures at temperatures below and above $T_c$ are shown in Figure 2.16[34]. When T > $T_c$, the crystal has a cubic structure and no spontaneous polarization exists (Figure 2.16a). When T < $T_c$, the octahedral cages of oxygen distort and the Ti and Ba sublattices are shifted relative to the negatively charged oxygens, producing a polarization. This shift breaks the cubic symmetry, resulting in six symmetry-equivalent variants with polarization along the x, y, and z axes. The specific shift of atoms along <100>, happened between the temperature ranging from 278 K to 393 K, results to a crystal structure transformation from cubic to tetragonal (Figure 2.16b and c), which is the phase concerned at room temperature.

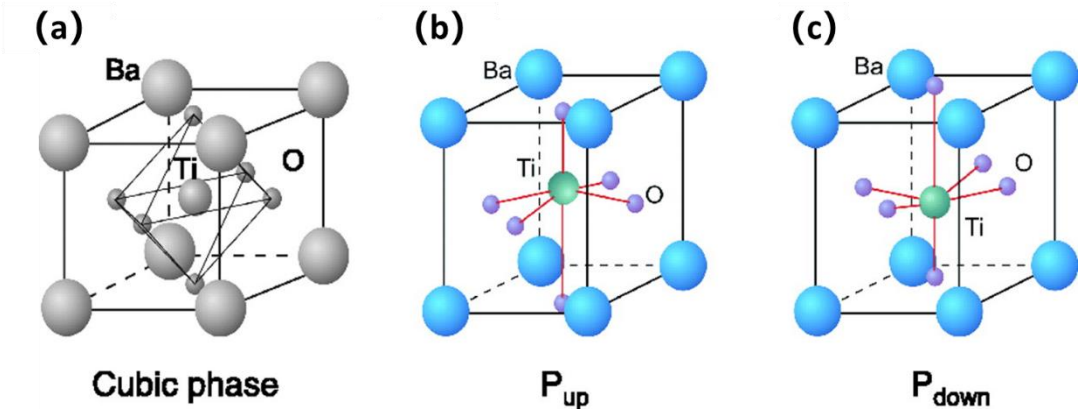


**Figure 2.16 Crystal structure of $BaTiO_3$. (a) above $T_c$, cubic phase. (b) and (c) at RT, tetragonal phases, with up and down polarization[34].**

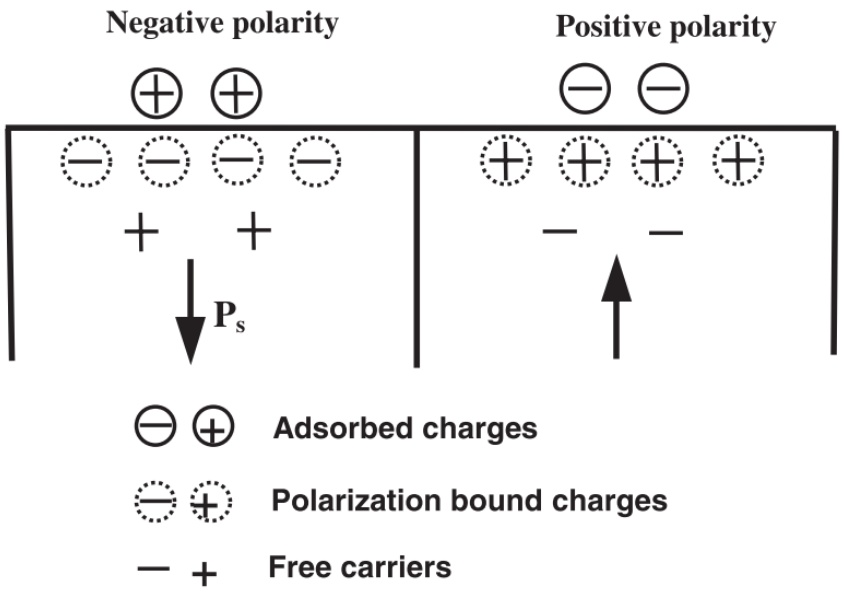


**Figure 2.17 Schematic illustration of spontaneous polarization induced surface charge and screening under different polarization orientations. $P_s$ is the spontaneous polarization[35].**

Spontaneous polarization will induce bound charges on the surface of ferroelectrics[35].

These charges can be compensated by internal and external screening effects. An electric field will be generated following the screening effect, the direction of which is opposite to the internal electric field induced by the spontaneous polarization. This electric field is termed as the depolarization field and it tends to destroy the spontaneous polarization in the ferroelectrics[36]. Figure 2.17 gives a schematic illustration of the spontaneous polarization induced surface charges and the screening results in a ferroelectric material.

### 2.2.4. Ferroelectric domain

A ferroelectric domain is defined as a region in which the spontaneous polarization direction is all aligned. In a virgin macroscopic crystal it is unlikely that the direction of the polarization will be the same through out. It is energetically more favorable for the crystal to break up into domains, which are macroscopic regions of homogeneous polarization only different in the polarization directions[33].

Domain walls are defined to describe the boundaries between the domains. Figure 2.18 shows a schematic figure of the domain and domain wall. Two kinds of domain walls can usually be generated, the 180° domain walls and the non-180° domain walls (typically the 90° domain walls). The physical origin of the 180° domain is to reduce the energy

caused by depolarization field and the non-180° domain is to minimize the strain energy caused by the lattice distortion during the phase transition and depolarization field. The electrostatic energy results from formation of the depolarization field. The formation of the domain/domain wall with the polarization vectors arranging in certain directions (head to tail across the 90° domain and parallel but opposite across the 180° domain) in the adjacent domains allows minimization of the energy and thus help to make the crystal stable.

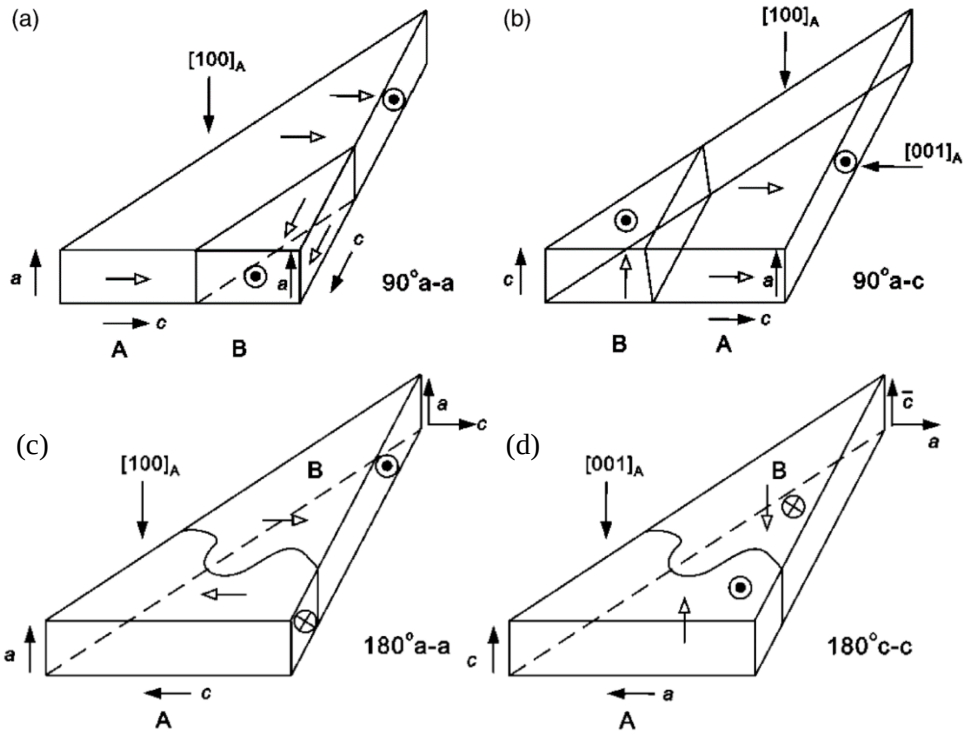


**Figure 2.18 Schematic of domain in a ferroelectric crystal[37].**

The motion and interaction of domain walls can have significant influence on the ferroelectric properties. In $BaTiO_3$, for example, high permittivity and piezoelectricity was achieved with grain size around 1 μm and this has been attributed to the 90° domain wall displacements under different electric fields[38]. Some characteristic optical and electronic behavior of ferroelectric materials have been attributed to the effects from domain walls as well[39-41]. For example, domain walls have been demonstrated to contribute to the anomalous photovoltaic effect in $BiFeO_3$ thin films, in which open circuit voltages ($V_{oc}$) larger than the material band gap have been generated. And by controlling conductivity of domain walls, $V_{oc}$ as high as 50 V has been achieved[39]. In the review paper by J. F. Scott et. al[42], the importance of domain walls in nanoelectronics has been stated based on the previous theoretical and experimental results, and the authors pointed out that regarding the ferroic device applications, the domain walls can be the main active element rather than the domains. Therefore, it is important to take the domain walls contribution into account when designing and evaluating the properties of ferroelectric materials.

### 2.2.5. Size effect on ferroelectric materials

Size effect on ferroelectric materials refers to the dependence of the structure and phase

transformation on the grain size in ferroelectric materials. The study of size effect on ferroelectric materials has been conducted for more than 50 years since the first report by Kneikamp and Heywang on the dielectric properties of $BaTiO_3$ ceramic[43], and the idea of a critical size for ferroelectricity has long existed[44]. Generally, it was recognized that the dielectric permittivity, $\varepsilon$, which is the amount of polarization change that can be induced under the application of an electric field, increased when the grain size decreased to micro level. The reported values of the 'critical size' vary in different ferroelectrics and are also related to the material forms (bulk ceramics, thin films or free particles). For example, $BaTiO_3$ ceramic has a well accepted critical size (the grain size) of around 400 nm[44-46], for $BaTiO_3$ film it has been predicted to have a much smaller critical size of ~ 40 nm[47], and that of $PbTiO_3$ particles is reported to be ~ 100 nm[48].

Grain-size effect on the ferroelectric properties of bulk ceramics is the firstly and mostly studied subject in this area. One early finding is the anomalously high dielectric permittivity observed in fine grain $BaTiO_3$ ceramics. In the study by Arlt in 1985[49], the grain size dependence of $\varepsilon$ has been demonstrated through experimental work, with the critical size observed at ~ 1 μm (as shown in Figure 2.19).

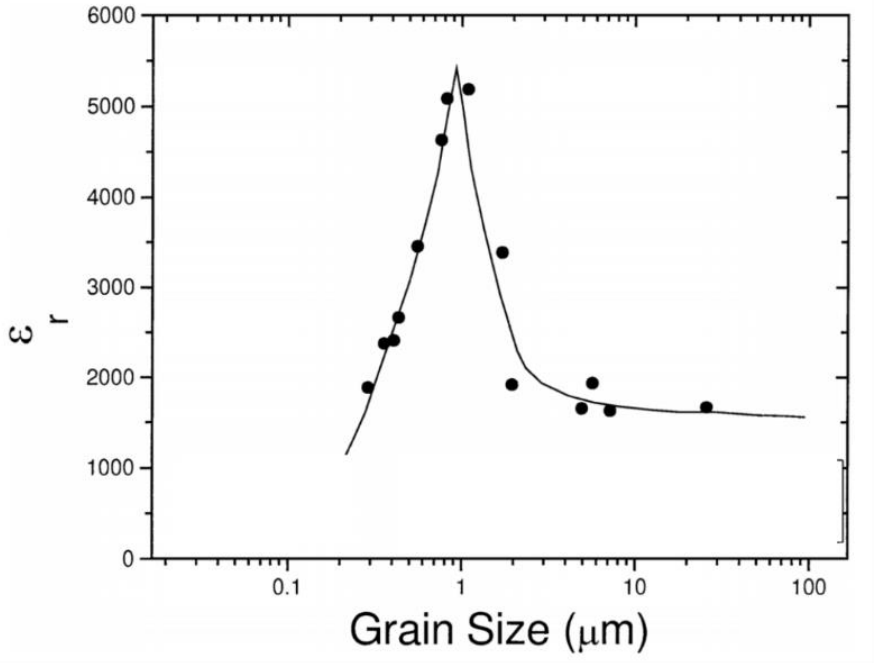


**Figure 2.19 Crain size dependence of the permittivity of $BaTiO_3$ ceramics[49,50].**

The later work by Zhao *et al*. in 2004 reported the $T_c$ and $\varepsilon$ dependence on grain size of $BaTiO_3$ ceramics[45]. The $T_c$ kept at ~ 120 °C when the grain size decreased from 1200 nm to 400 nm and declined sharply when grain size reduced below 400 nm (Figure 2.20b). The $\varepsilon$ peak value decreased with decreasing grain size and strongly depressed in samples with fine grains (< 300 nm, Figure 2.20a). The critical grain size of ~ 400 nm has been reported in other studies and is well accepted since then[46].

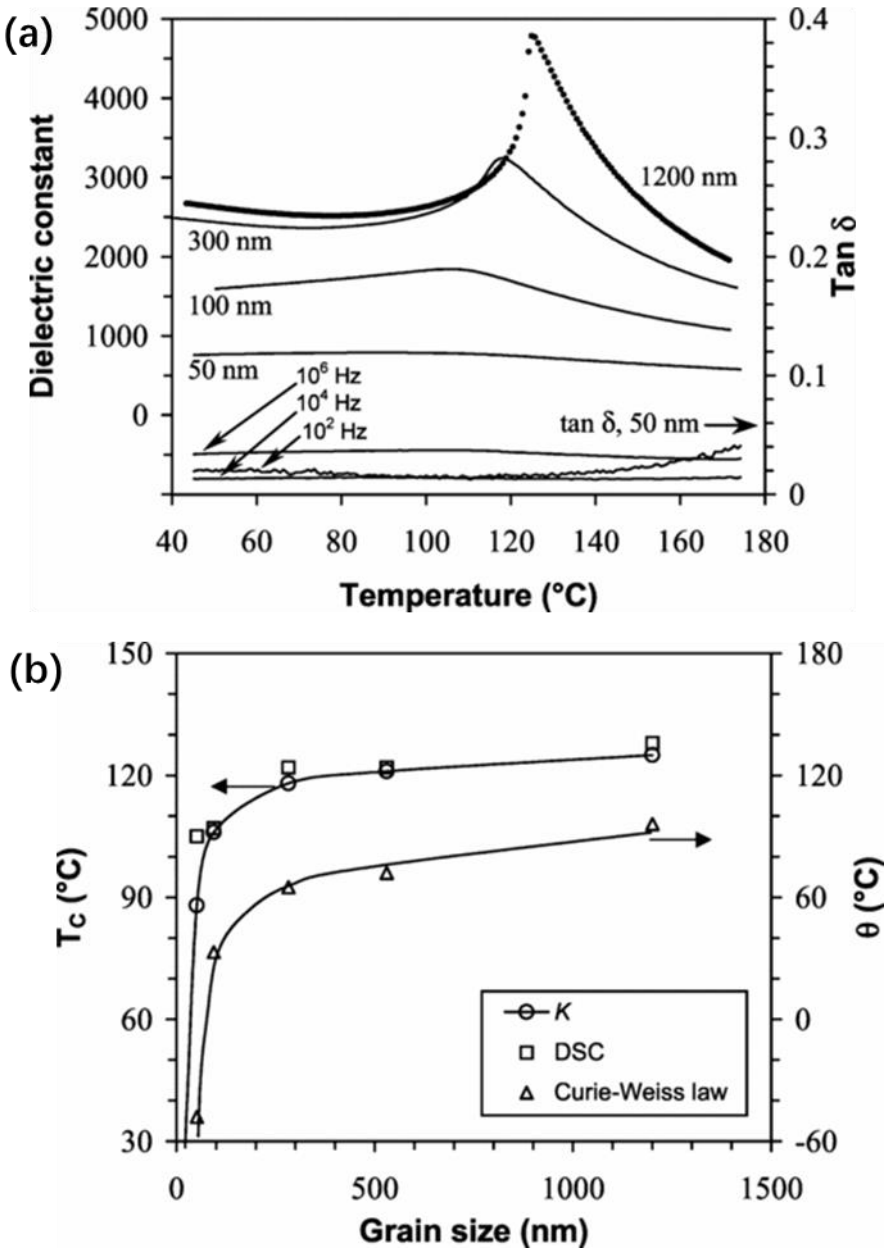


**Figure 2.20 (a) Relative dielectric permittivity (ε) and loss tangent (tan δ) of $BaTiO_3$ ceramics as a function of temperature. (b) Critical temperatures of $BaTiO_3$ ceramics as a function of grain size[45].**

The competition between contributions from domain/domain walls and grain boundaries

has been used to explain the size effect in ferroelectric ceramics[46,50,51]. It is well known that when the phase transformation occurs in ferroelectric material on cooling, the internal stress produced in the polar structure can be relieved by the formation of polydomain subgrain structure (mainly the 90° domains). Thus in large-grained ceramics, the contribution from 90° domain walls to the dielectric constant dominates[46]. With decreasing grain size, the single domain single grain structure becomes energetically favorable. Therefore the fraction of grain boundary volume increases with decreasing grain size, leading to a reduced dielectric constant since the grain boundary has much lower permittivity[46]. Accordingly, the dielectric constant of ferroelectric ceramics will reach a maximum when the grain size reduces to a specifically value, and then decrease as the grain size further reduced.

When it comes to lower dimensions, *i.e.*, thin films and nanoparticles, investigation of the size effect in ferroelectrics becomes more challenging due to the difficulties existed in the sample preparation and characterisation with high precision in nanoscale. A deep understanding of it has been built up in recent years, though no conclusive agreement yet, owing to the development in the preparation of high-quality, monocrystalline ferroelectric nanomaterials and the advanced measurement techniques. The understanding of the nanoscale ferroelectricity has been evolving from the earliest views of complete

suppression of ferroelectric behavior[48,52] to the more recent reports that demonstrating enhancement of local ferroelectric distortions with a decline in the long-range polar distortions[53,54].

The most often reported size effect in nanoscale ferroelectrics is the shifting of $T_c$ towards lower temperatures with decreasing grain size. This has been interpreted as suppression or disappearance of ferroelectricity in finite-sized materials in earlier studies, with a range of investigations done previously aiming to find out the critical sizes for different nanoscale ferroelectric materials. For example, study by Uchino *et al.* based on XRD results indicated that the phase transformation of $BaTiO_3$ nanoparticles from tetragonal to cubic occurred at a critical size of 120 nm at room temperature[55]. With more methods applied to study this issue and more aspects understood, the reported critical size decreased from hundreds of nanometers to a few nanometers, or even smaller. Calculations made by Spanier *et al*. using theoretical modeling estimated that the critical size for a $BaTiO_3$ sphere to be 4.2 nm[56]. And the more recent research by Polking *et al*. demonstrated room-temperature polarization switching of $BaTiO_3$ down to ~ 5 nm by PFM characterisation, with the presence of a single-domain polarization state observed by TEM technique[54].

By far, there is no agreed conclusion for the changing of ferroelectric behavior at finite dimensions. Though possible causes include the depolarization effects[57], the absence of long-range cooperative interactions[53], structural defects[58] and elastic constraints[46] have been widely considered and accepted. And it has also been realized that for the study of size effect, it is important to characterise the nanoscale ferroelectricity on different time and length scales to make a full picture of the material structural feature[44].

Common experimental methods used to investigate the size effect in ultra fine ferroelectrics include that of X-ray diffraction, Raman spectroscopy and differential scanning calorimetry. XRD technique relies on coherent scattering from numerous unit cells and can thus provide the information of the average and static symmetry of the products, but it can not distinguish between the average and local structure. While Raman spectroscopy can show the local and dynamic symmetry around the scattering sites. Existence of tetragonal symmetry in small-dimension-ferroelectric has been demonstrated by Raman spectra, even though when it was not distinguished by XRD[59,60]. DSC thermal test can reveal the dependence of phase transformation thermal characteristics on grain size by giving out the values of the transition enthalpy. The orthorhombic-tetragonal and tetragonal-cubic transformations in $BaTiO_3$ polycrystals in a size range of 10 μm to 35 nm have been observed in the DSC data in the work by

M. H. Frey[44] (as shown in Figure 2.21), and it also revealed the polydomain to single-domain structure transformation characterised by the broadening and weakening thermal peaks following the decreasing grain size.

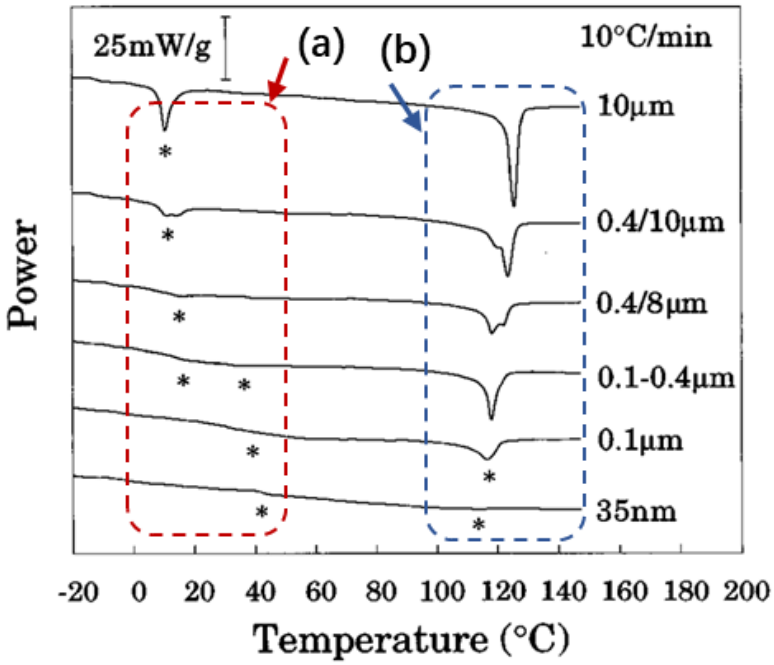


**Figure 2.21 DSC data of $BaTiO_3$ polycrystals, showing the dependence of phase transition thermal characteristics on grain size (a) first order orthorhombic-tetragonal transformation (b) tetragonal-cubic transformation[44].**

In the work by Smith *et al.*, XRD, Raman spectroscopy and theoretical calculations have been employed to investigate crystal structure and the phase transition of various sizes of nanocrystalline $BaTiO_3$[53]. In this study both XRD and Raman results demonstrated phase transition in nanoscale $BaTiO_3$ with temperature changing. Peak splitting has been

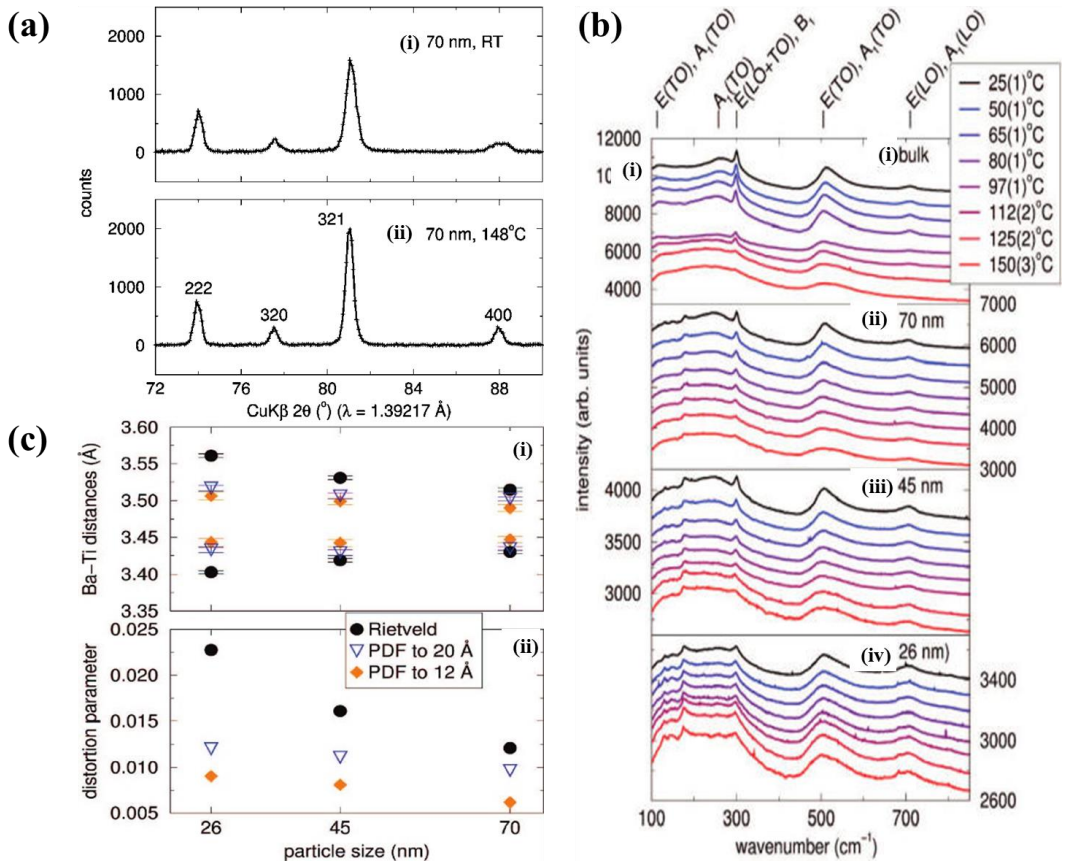


**Figure 2.22 (a) XRD data of 70 nm $BaTiO_3$ particle recorded at (i) room temperature; (ii) at 148 °C. (b) Raman spectra at different temperatures for different sized-$BaTiO_3$. Temperatures increase from top to bottom in each panel. (c) (i) Long and short Ba-Ti distances and (ii) distortion parameter, results from synchrotron Rietveld refinements and PDF analysis[53].**

observed in the XRD pattern, with the (004) reflection in the cubic phase widen and losing intensity at RT (Figure 2.22a). This is attributed to the change of lattice parameters (a and c) when the cubic structure transformed to tetragonal structure. In the tetragonal phase, the c/a ration is larger than 1, the (004) reflection shifts to a lower 2θ value, thus the (400) reflection is correspondingly divided into (400/040) and (004) peaks, resulting in a

broadening peak.

It is worth noticing that despite the changes in symmetry, the cubic-tetragonal structure transformation can be possibly not well resolved in XRD results of nanosized ferroelectrics due to the inherent line broadening resulting from the small particle size. In the Raman spectra (Figure 2.22b), two peaks which are characteristic of the polar structure (tetragonal phase) at ~ 300 and 750 $cm^{-1}$ are observed in all samples (from bulk to 26 nm sample), demonstrating the exist of polar structure. The two peaks decrease rapidly as the temperature increasing through the curie point, which is interpreted as an indication of the phase transformation. Besides, the broadening Raman peaks in smaller sized samples suggest that the tetragonal structure is present with a significantly decreased structural coherence. Meanwhile the Rietveld and PDF (pair distribution function) analysis suggested increased distortions with decreasing particle size (shown in Figure 2.22c). Thus it was suggested by the work that it is the decreased coherency of the distortions rather than the structural distortions in smaller particles that leads to the size effect in nanostructured-$BaTiO_3$.

Since the current work aims to investigate the effect of ferroelectricity on photocatalytic performance in ferroelectric materials, the size effect must be taken into consideration

when evaluating the ferroelectric properties in nanoscale products.

### 2.2.6. Ferroelectric materials in the application of photocatalysis

The study of ferroelectric materials applied as photocatalysts dates back to the 1970s, when the photochemistry of $BaTiO_3$ was reported by Nasby and Quinn[61]. After that, extensive studies have been focused on the surface photochemistry of ferroelectrics trying to find out the relationship between the ferroelectric nature and the influence that may have on the surface photochemistry. In recent years, there have been a growing interest in the study of ferroelectric materials in the application of solar energy conversion owing to some unique properties of the ferroelectrics.

Compared to traditional semiconductors, semiconducting ferroelectrics exhibit several special properties that attract significant interest in its application in solar energy conversion. These properties can be concluded mainly as three aspects: (1) abnormal photovoltaic effects, (2) polarization-dependent surface properties and (3) the internal electric field.

**(1) abnormal photovoltaic effects**

The abnormal photovoltaic effect (APV) was observed in ferroelectric Rochelle salt crystal in 1939 by Brady *et al*[62]. Photovoltage that can be a few orders of magnitude larger than the bandgap of the ferroelectric materials has been observed in $LiNbO_3$[63], $BaTiO_3$[64], $Pb(ZrTi)O_3$[65] and $BiFeO_3$[66] in the later studies. For a typical semiconductor, it is well known that the photovoltage produced cannot exceed its band gap. Ferroelectric materials is the only group of materials that can produce a photovoltage larger than its band gap. The mechanism behind it is still under study[42,67,68]. Though the ferroelectric material can have large photovoltaic output, its application in solar energy application is limited by low photocurrent output resulted from its poor bulk conduction. Thus, use of ferroelectric material with improved carrier transport property will be promising to achieve higher energy conversion efficiency.

**(2) polarization-dependent surface properties**

The polarization-dependent surface property of ferroelectrics is correlated with the spontaneous polarization. It has been reported that the polarized surface of ferroelectric material can have interactions with metal ions and organic species, allowing for spatial separation of the reduction/redox reactions on the surface[69-71]. One representative example of the poled surface resulted selective deposition of metal ions is the work by

Rohrer *et al.*[72]. It was observed that $Ag^{+}/Pb^{2+}$ was reduced/ oxidized preferentially on the positive ($C^{+}$)/negative ($C^{-}$) charged domains.

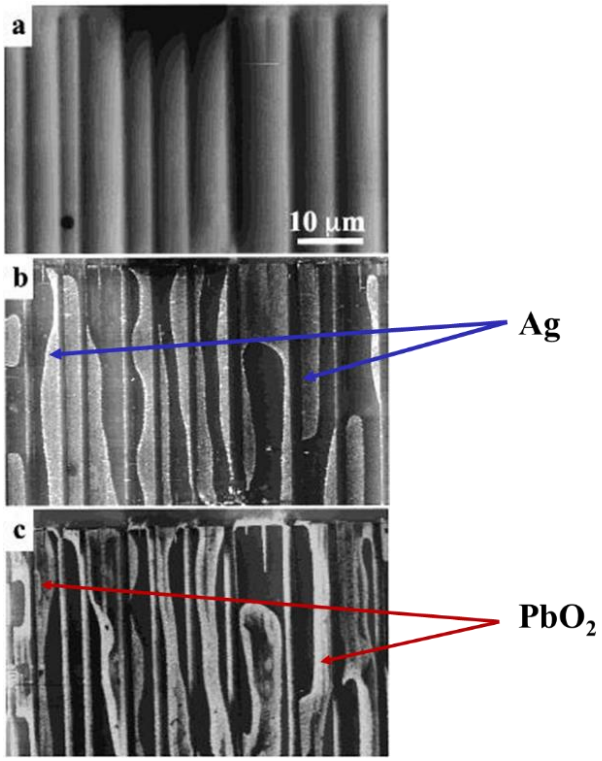


**Figure 2.23 AFM images of a $BaTiO_3$ single crystal (a) before and (b) after illumination in a $AgNO_3$ solution. The white contrast is Ag. (c) The same area after it was cleaned and illuminated in a $Pb(CH_3COO)_2$ solution. The white contrast is $PbO_2$ deposits[72].**

The AFM images of the single-crystal $BaTiO_3$ before and after light illumination in the presence of $AgNO_3$ and $Pb(CH_3COO)_2$ solution were shown in Figure 2.23. It was explained that driven by the electric field, electrons in $C^{+}$ domains would transfer to the surface and reduce $Ag^{+}$ to Ag nanoparticles and holes in $C^{-}$ domains would transfer to the

surface to oxidize $Pb^{2+}$ to $PbO_2$.

These findings demonstrated that the polarization-dependent surface of ferroelectrics can be manipulated to conduct selective redox reactions on separated surface sites, which is beneficial when applied as photocatalysts since it can separate the oxidation and reduction products spatially thus inhibiting the back reactions and increasing the solar energy transition efficiency.

**(3) the internal electric field**

The internal electric field within ferroelectric materials has been demonstrated to be able to aid the spatial separation of photogenerated charge carriers following the light absorption, thus enhance the charge separation efficiency in the photocatalytic procedure[12,73,74]. As stated in the previous section, spontaneous polarization will induce an electric field, which is termed as the internal electric field. The direction of spontaneous polarization is defined as pointing from the negative bound charge to the positive bound charge, and the internal electric field will have the opposite direction. The surface region with positive bound charges is called a $C^+$ domain, and that with negative bound charges is called a $C^-$ domain. Due to the screening results, negative charges will

gather at the $C^+$ domain and lead to downward band bending and positive charges will gather at the $C^-$ domain and lead to upward band bending. A schematic is shown in Figure 2.24.

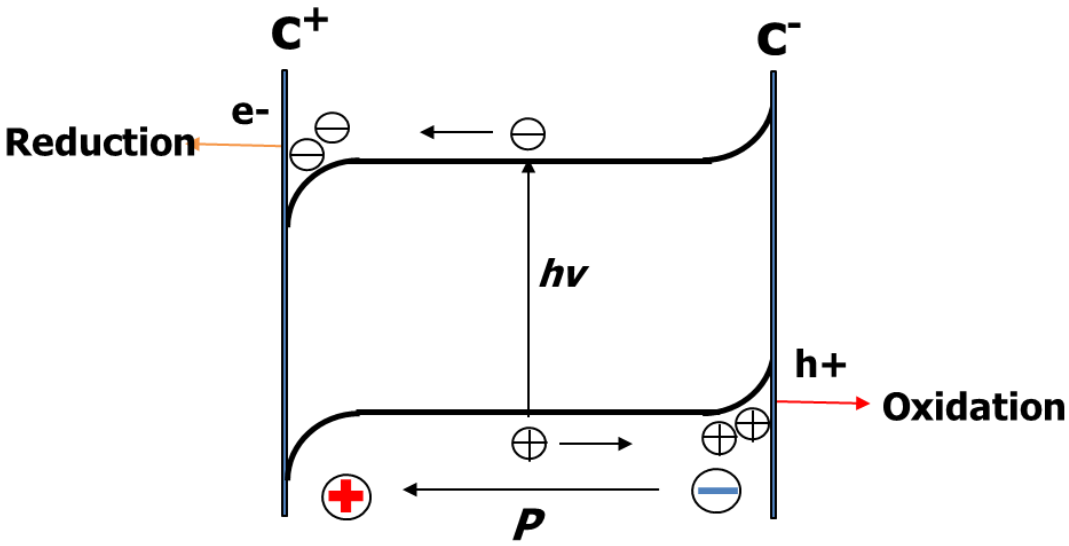


**Figure 2.24 Schematic of a ferroelectric material showing the band bending on the $C^+$ surface and $C^-$ surface, respectively. The moving of a pair of photogenerated electron and hole toward opposite directions under the internal electric field is illustrated. *P* is the spontaneous polarization[73].**

The application of ferroelectrics in photocatalysis and the influence of the internal electric field on the photocatalytic performance have been investigated by different characterisation methods. The paper by Cui *et al*. in 2013 reported a study on the effect of ferroelectricity on the photocatalytic activity of $BaTiO_3$[73]. Two structures of $BaTiO_3$, cubic (non-polar) and tetragonal (polar), have been employed to investigate their

photocatalytic activity in dye degradation. It showed that enhanced dye degradation rate was achieved by using tetragonal $BaTiO_3$, compared to the cubic one.

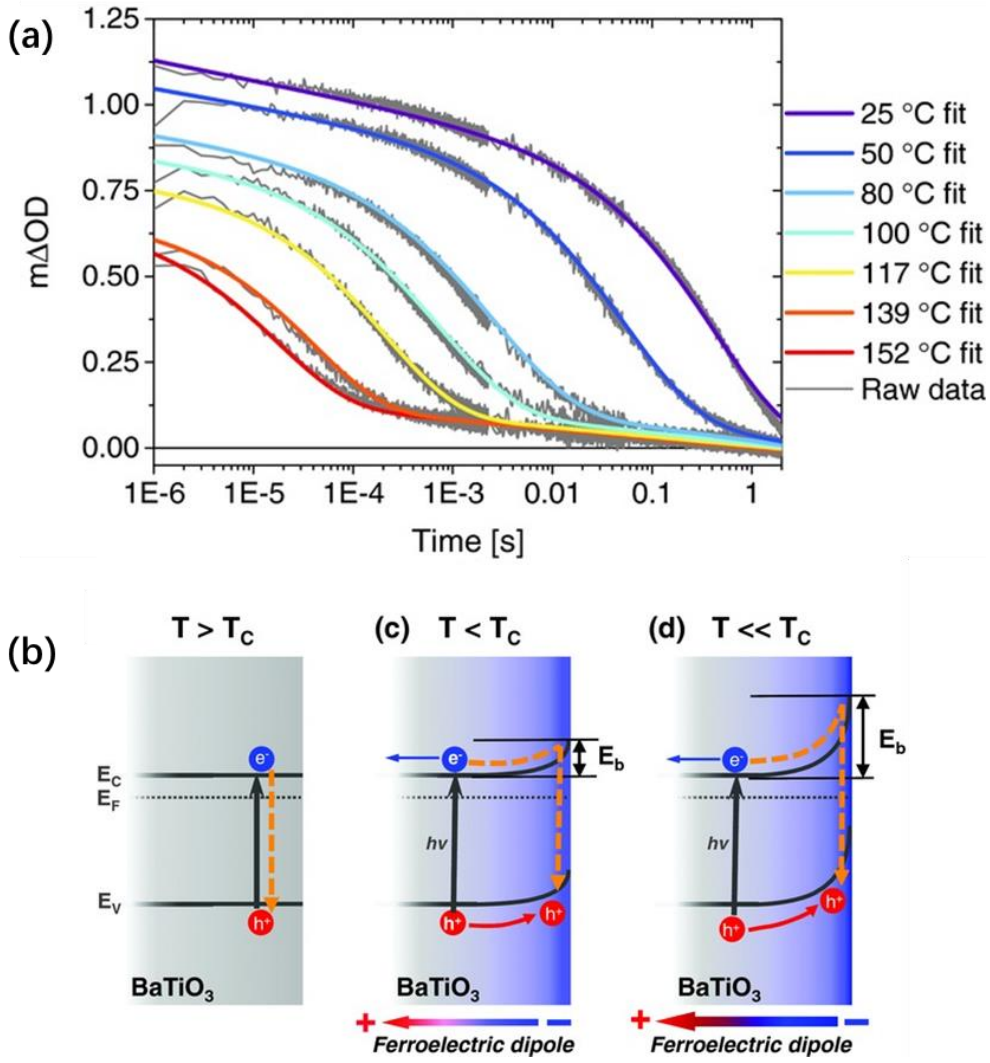


**Figure 2.25 (a) Dependence of transient absorption decays of $BaTiO_3$ on temperature (b) Schematic of polarization-induced band bending changing with temperature[74].**

The work later on by Morris *et al*. furthered the study by exploring the charge carrier

dynamics of $BaTiO_3$, in which transient absorption spectroscopy was used to probe the correlation between ferroelectric polarization and carrier lifetimes[74]. Long lived carriers have been observed ($t_{50\%}$ =0.12s) in tetragonal $BaTiO_3$ and the carrier life time rapidly decreased ($t_{50\%}$ < 100 μs) in cubic $BaTiO_3$. In addition, results of the variable-temperature TAS showed a strong lifetime dependence on temperature, with a significant acceleration of the charge carrier decay dynamics observed under heat treatment from 25 °C to 152 °C (as shown in Figure 2.25a). The results indicated that the carrier decay dynamics is in close relation to the dipolar crystal structure which is temperature dependent. A schematic representation of polarization-induced band bending changing with temperature was shown in Figure 2.25b.

Besides the study on particulate ferroelectrics, the effect of internal electric field on ferroelectric film in the application as photoelectrodes have also been investigated in recent years. Compared to powdered samples, film samples can be polarized by external bias, allowing for study of the effects from not only the existence of internal electric field but also manipulation of the polarization direction of it on the photocatalytic performance. A switchable charge-transfer phenomenon has been reported by Cao *et al* in 2014, in which the $BiFeO_3$ film was used as the target ferroelectric[75]. When the pretreatment poling bias changed from - 8 V to + 8 V, the observed photocurrent switched from

0 μA/cm$^2$ to 10 μA/cm$^2$ at 0.2 V vs NHE, indicating that by manipulating the internal electric field, the band bending at the surface of the ferroelectric electrodes can be switched and utilized to drive both reduction and oxidation reactions according to the remnant polarization orientation.

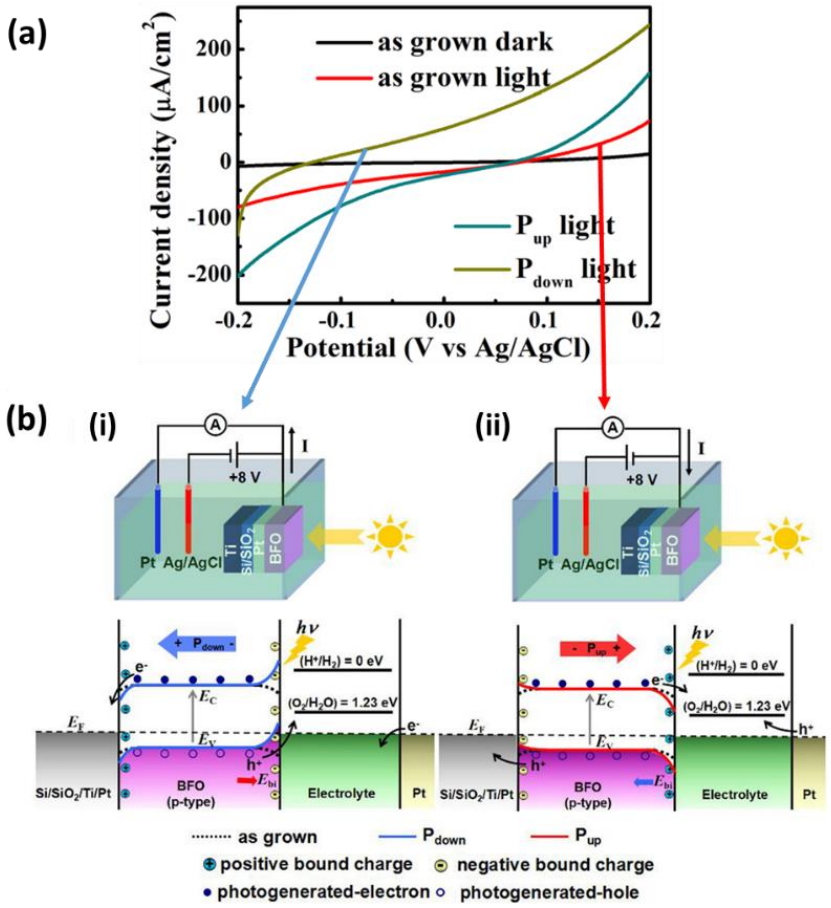


**Figure 2.26 (a) Photocurrent curves obtained with applied potential, under different ferroelectric polarization conditions. (b) Schematic representations of the energy band diagrams and the operational principle of the PEC cell under different poling conditions: (i) negative polarization with associated upward band bending (ii) positive polarization with associated downward band bending[76].**

A later work by Liu *et al*. also observed the polarization-dependent PEC properties of $BiFeO_3$ films, which has been attributed to the modulation of band structure at the $BiFeO_3$/electrolyte interface by the polarization[76]. The I-V curves of the $BiFeO_3$ films after poling treatment by + 8 V and – 8V bias is shown in Figure 2.26a, and the corresponding schematic of the energy band diagrams under different poling conditions is shown in Figure 2.26b. The as-grown $BiFeO_3$ film is p-type, thus has a downward band bending in the electrolyte under equilibrium, analogous to that of a conventional p-type semiconductor. When poled by an applied bias which is large enough to switch the domain orientation, the film will be poled and the domains will have the same orientation, leading to a strong depolarization field and thus a strong band bending in the surface. The addition or subtraction of the internal electric field raised band bending on the original band bending then determined the transferring direction of the photogenerated electrons and holes, which resulted to the switchable photocurrents.

The effects of ferroelectric polarization on photocatalytic performance are also reported in other ferroelectrics such as $Pb(Zr,Ti)O_3$ (PZT)[77] and $LiNbO_3$[78]. A positively poled PZT has been reported to show much higher hydrogen production efficiency than negatively poled PZT during photocatalysis[77]. And the investigation of photocatalytic degradation of organic dyes by $LiNbO_3$ showed that high rate degradation was observed despite the

wide band gap of $LiNbO_3$ (3.7 eV), owing to the spatial separation of redox reactions resulting from the ferroelectric polarization[78]. Ferroelectric materials can be promising in the use as photocatalysts owing to their specific properties which can be used to break the limits imposed by conventional semiconductors. Though the photocurrent they can achieve is limited in the current stage due to their insulating bulk nature, the specific properties they showed in the photocatalytic applications are attractive and promising in the future use.

## 2.3. **Photocatalysts Used in this Research**

Three materials, $BiFeO_3$, $Bi_2Fe_4O_9$ and $Ba_xSr_{1-x}TiO_3$ (x = 0.2 and 0.8), have been synthesized and used as the target materials in this research. $BiFeO_3$ was chosen because of two main reasons: its narrow band gap which allows for visible light absorption and its ferroelectric polar structure which can contribute to the photoexcited charge carriers separation. The investigation of $Bi_2Fe_4O_9$ as a photocatalyst is inspired by the work of $BiFeO_3$, as another typical member of the bismuth ferrite family which also owns a narrow band gap. Nanoscale $Ba_xSr_{1-x}TiO_3$ (x = 0.2 and 0.8) single crystals are prepared to investigate the effect of ferroelectric polar structure on photocatalytic performance.

### 2.3.1. $BiFeO_3$

Ferroelectric materials have gained increasing interests in photocatalytic and photovoltaic applications during the past few years due to the unique properties they exhibit such as the enhanced photoexcited charge separation and the above-band-gap photovoltage, which has been attributed to their ferroelectric nature[74,79].

Bismuth ferrite ($BiFeO_3$) is one of the few visible light driven photoactive ferroelectric materials, with a narrow band gap of 2.1 to 2.8 eV[80]. The potential application of $BiFeO_3$ in solar energy conversion has been extensively investigated, including that in organic dye photodegradation, water splitting and solar cells[81-83]. Effect of ferroelectricity on its semiconductor behavior has also been reported in previous studies, as discussed in the last section. Though extensively studied, there still exist many controversies and ambiguities in the research work on $BiFeO_3$ to date. Understanding the complex characteristics of $BiFeO_3$, specifically the electronic structure and the associated optical property is of great importance for its future use in solar energy conversion.

The structure of $BiFeO_3$ at room temperature is rhombohedral (point group $R3c$)[84], as shown in Figure 2.27 for a schematic view. It has a Curie point of $T_c$ = 830 °C.

Spontaneous polarization of $BiFeO_3$ can reach up to 100 μC/cm$^2$ as suggested by theoretical calculations[85]. The large ferroelectric polarization is mostly caused by the displacement of $Bi^{3+}$ ion, with the lone pair of 6s electrons as the driving force of the ferroelectric distortion[86].

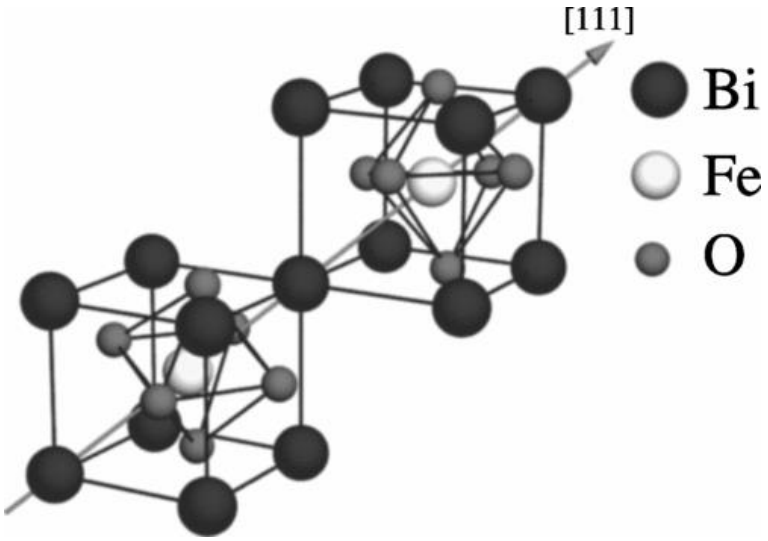


**Figure 2.27 Schematic view of the *R3c* structure of $BiFeO_3$ [87].**

The electrical property of $BiFeO_3$ is a complex topic, either for the application as a ferroelectric material or for the application as a semiconductor photocatalyst. There exist the possibility of Bi loss during annealing procedure due to the high volatility of Bi, and the loss of O which is common in perovskite film synthesis and by the associated reduction of $Fe^{3+}$ to $Fe^{2+}$.[88,89]. Loss of Bi will lead to Bi vacancies which will cause p-type

conductivity and loss of O will lead to O vacancies which will cause n-type conductivity. Meanwhile, the fluctuations between $Fe^{3+}$ and $Fe^{2+}$ makes the situation more complex[90]. Thus, the conductivity type of $BiFeO_3$ depends on the intrinsic defects of its crystal structure[91-93].

A wide range of band gap from 2.1 eV to 2.8 eV has been reported for $BiFeO_3$ thin films, with both indirect/direct band gap observed[80]. Previous reports indicated that the band gap of $BiFeO_3$ film can be sensitive to epitaxial strain and/or synthesis conditions such as temperature, atmosphere and pressure, while a more recent study based on more than forty $BiFeO_3$ thin films suggested that the band gap of $BiFeO_3$ depends more on the surface roughness as well as film thickness rather than the processing parameters[94]. Following the tremendous literature data, it indicates that evaluation and comparison of optical properties of $BiFeO_3$ thin films should be proceeded with caution.

Despite the numerous reports and the attractive properties, there are still a lot of unresolved aspects of $BiFeO_3$. The complicated phase transitions resulted difficulty in pure phase synthesis of $BiFeO_3$, the argue in the direct/indirect optical band gap, and the complexity in understanding the mechanism behind some unexpected behaviors, all making it an interesting and challenging material to investigate.

### 2.3.2. $Bi_2Fe_4O_9$

$Bi_2Fe_4O_9$ is another member of the bismuth ferrite family. Previous studies showed that it is a promising candidate for use as semiconductor gas sensors, owing to its high sensitivity to ethanol and acetone vapors[95]. In addition, it can catalyze the ammonia oxidation to NO thus can be used as a cheaper replacement of the current catalysts which are based on expensive platinum, rhodium, and palladium[96]. The crystal structure of $Bi_2Fe_4O_9$ is orthorhombic (space group *Pbam*), a schematic view is shown in Figure 2.28.

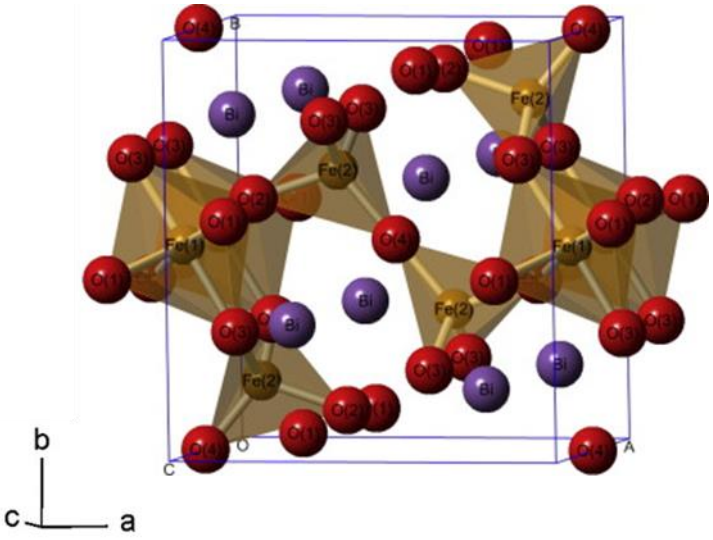


**Figure 2.28 Crystal structure of $Bi_2Fe_4O_9$[97].**

Akin to many other Bi-based compounds, $Bi_2Fe_4O_9$ exhibits a narrow band gap with

reported values ranging from ca. 1.9 to ca. 2.1 eV, which is highly visible-light active with a near-infrared absorption. The small band gap makes it a promising material for photocatalytic application. Till now, particular $Bi_2Fe_4O_9$ as photocatalysts has been reported in several papers, in which the $Bi_2Fe_4O_9$ nanoparticles showed excellent photocatalytic activity in oxidation of phenol and aqueous ammonia and degradation of the organic contaminants such as methyl orange and Congo Red[98-100]. The outstanding photocatalytic performance of the $Bi_2Fe_4O_9$ nanoparticles indicates its promising utilization in PEC water splitting in a form of thin film electrode. But till now there's no report on the $Bi_2Fe_4O_9$ film as photoelectrode. Thus it is of our interest to prepare the $Bi_2Fe_4O_9$ film and investigate the photocatalytic behavior of it.

### 2.3.3. $Ba_xSr_{1-x}TiO_3$

Barium strontium titanite is a ternary perovskite oxide with the stoichiometric formula of $Ba_xSr_{1-x}TiO_3$ ($0 < x < 1$). It is a continuous solid solution containing $BaTiO_3$ and $SrTiO_3$ over the entire composition range. The $Ba_xSr_{1-x}TiO_3$ solid solution showed various potentials in the application of electronic devices such as voltage-tunable capacitors, passive memory storage devices, transducers and sensors, due to its high dielectric constant, low dielectric loss, good thermal stability and high frequency

characteristics[101,102]. Despite the application in piezoelectric and ferroelectric devices, $Ba_xSr_{1-x}TiO_3$ compounds have been also reported as wide-band-gap semiconductors used for solar energy conversion. The band gap and band positions of $BaTiO_3$ and $SrTiO_3$ have been studied as well. Both $BaTiO_3$ and $SrTiO_3$ have a UV light absorption, with a band gap of around 3.2 eV, close to that of $TiO_2$ (as shown in Figure 2.29). The conduction and valence band edges of $BaTiO_3$ and $SrTiO_3$ straddle the redox potential of water, allowing for unassisted photocatalytic water splitting in principle[103].

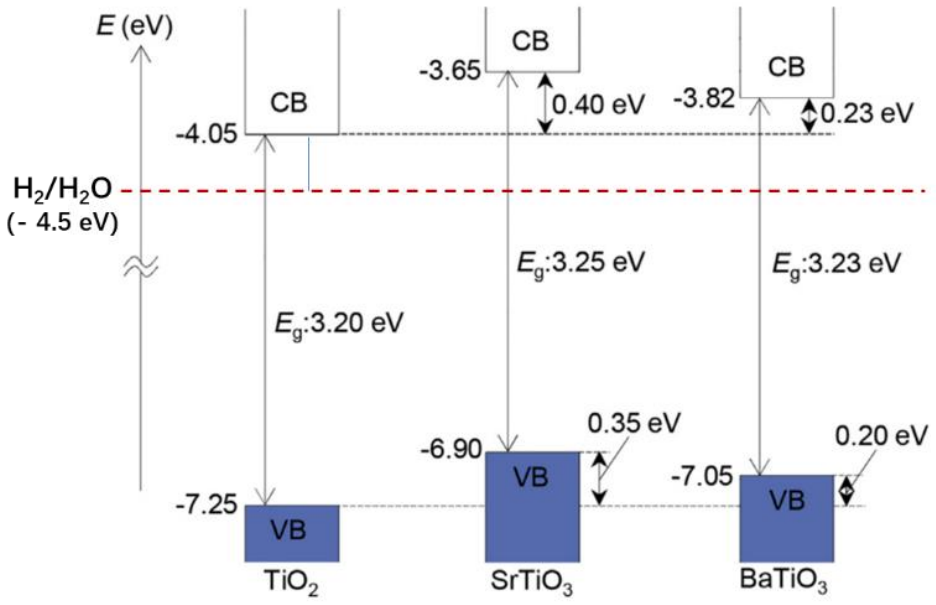


**Figure 2.29 Energy level diagram of $TiO_2$, $SrTiO_3$ and $BaTiO_3$[103]**

The properties of $Ba_xSr_{1-x}TiO_3$ are strongly dependent on the composition and

characteristics of its constituent materials. The structure and dielectric properties of $Ba_xSr_{1-x}TiO_3$ ceramic solid solutions have been studied since an early time and a systematical picture of its dielectric properties has been established based on the whole composition range[104]. When x = 1, it is $BaTiO_3$. As it has been described previously, $BaTiO_3$ has a Currie Temperature of 120 °C (393 K). Thus it has a tetragonal structure and is ferroelectric at room temperature[105]. When x = 0, it is $SrTiO_3$. $SrTiO_3$ has a Currie Temperature of ~ approx. -240 °C[106], thus it has a cubic structure at room temperature and is paraelectric. At room temperature, Ba-rich $Ba_xSr_{1-x}TiO_3$ compounds have a tetragonal structure as $BaTiO_3$ and are ferroelectric, whereas Sr-rich $Ba_xSr_{1-x}TiO_3$ compounds have a cubic structure as $SrTiO_3$ and are paraelectric. The substitution of the Ba by Sr will give a range of solid solutions of $Ba_xSr_{1-x}TiO_3$, the Curie temperature of which is composition-dependent, decreased with increased Strontium content[107].

Two compositions of $Ba_xSr_{1-x}TiO_3$, $Ba_{0.2}Sr_{0.8}TiO_3$ and $Ba_{0.8}Sr_{0.2}TiO_3$, have been chosen as the target material in this study. $Ba_{0.2}Sr_{0.8}TiO_3$ has a $T_c$ of ~ -148 ℃ (125 K) and $Ba_{0.8}Sr_{0.2}TiO_3$ has a $T_c$ of ~ 72 ℃ (345 K) (as shown in Figure 2.30), which allows us to study the effect of spontaneous polarization on photocatalytic behavior since they are supposed to have non-polar and polar structure respectively at room temperature[104].

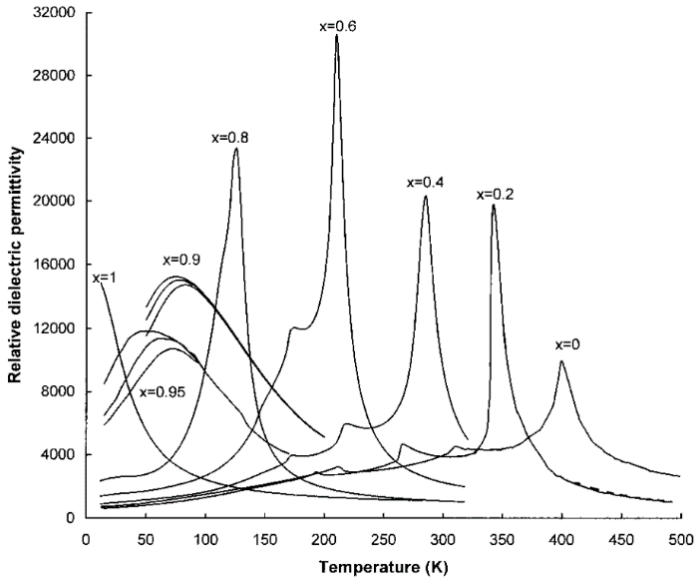


**Figure 2.30 Relative dielectric permittivity as a function of temperature for $Ba_{1-x}Sr_xTiO_3$ ceramics[104].**

## 2.4. **Aims and Objectives**

The aim of this research is to investigate photocatalytic performance of bismuth ferrite thin films and nanoscale barium strontium titanate powders for understanding of the unique properties ferroelectric photocatalysts exhibit and the effect of the ferroelectric polar structure on photocatalytic activity.

$BiFeO_3$ was chosen as the target material because it is ferroelectric at room temperature and has a narrow band gap which allows it to absorb visible light and thus potentially has

a higher solar light conversion efficiency compared to other wide-band-gap ferroelectric materials. When conducting the compositional study of $BiFeO_3$, $Bi_2Fe_4O_9$, one of the parasitic phases of $BiFeO_3$, has been found to be a promising photoelectrode material with high visible light photocatalytic activity. Thus the PEC performance and band structure of $Bi_2Fe_4O_9$ film as a photoelectrode have been studied and reported for the first time. $Ba_xSr_{1-x}TiO_3$ (x = 0.2 and 0.8) powders were selected to carry out the study of effect of polar structure on photocatalytic activity. $Ba_{0.2}Sr_{0.8}TiO_3$ has a curie temperature of ~ – 148 ℃ and $Ba_{0.8}Sr_{0.2}TiO_3$ has a curie temperature of ~ 72 ℃. At room temperature, $Ba_{0.2}Sr_{0.8}TiO_3$ has a cubic structure (non-polar) and $Ba_{0.8}Sr_{0.2}TiO_3$ has a tetragonal structure (polar-structure). This allows the study of effect of spontaneous polarization on photocatalytic behavior by comparing the photocatalytic activity of the two samples.

The main objectives are:

1. Study the photoelectrochemical performance of $BiFeO_3$ thin film applied as photoelectrode, including the synthesis of pure phase $BiFeO_3$ film by the chemical solution deposition method, characterization of band structures and associated optical properties, probing of the switchable photocurrent polarity under various applied potentials exhibited by the as-obtained $BiFeO_3$ photoelectrode.

2. Study the photoelectrochemical performance of $Bi_2Fe_4O_9$ thin film which has been applied as photoelectrode for the first time, including the film synthesis by CSD method, structure and composition characterisations and the understanding on the charge transfer mechanism at the photoelectrode surface by adding of a hole scavenge.

3. Study the effect of ferroelectricity on photocatalytic activity using single-grain-single-domain barium strontium titanate powders, including the synthesis of nanoscale $Ba_xSr_{1-x}TiO_3$ (x = 0.2 and 0.8) powders by molten salt method, characterisation and demonstration of the single-domain structure and assessment of photocatalytic activity of the two samples by photodegradation of Rh B.

# Chapter 3 Experimental Procedure

## 3.1. Materials Synthesis

Material synthesis in this thesis comprises the thin film synthesis by chemical solution deposition (CSD) method and the nanoscale powder synthesis by molten-salt method.

### 3.1.1. Bismuth ferrite thin film preparation process

Bismuth ferrite thin films, including $BiFeO_3$ and $Bi_2Fe_4O_9$, have been prepared by the CSD method for application as photoelectrodes. The film synthesis was conducted following 3 steps: (1) precursor preparation, (2) film deposition, and (3) film heat treatment.

#### 3.1.1.1. Precursor preparation

Bismuth nitrate ($Bi(NO_3)_3 \cdot 5H_2O$) and iron nitrate ($Fe(NO_3)_3 \cdot 9H_2O$) were used to provide the metal source of Bi and Fe. 2-methoxyethanol (2-MOE) was used as the solvent since it has good solubility for bismuth and iron nitrates and also it has suitable viscosity and surface tension for spin-coating deposition. Acetic anhydride works as the chelating agent in the solution, it can dehydrate the water of crystallization from the metal salts, which is

helpful in control of the extent of hydrolysis and gelation. The precursor preparation route is shown schematically in Figure 3.1. The precursor with Bi : Fe ratio of 1:1 was used for the production of $BiFeO_3$ and the ratio of 0.5:1 was used for the production of $Bi_2Fe_4O_9$. The $BiFeO_3$ precursor solution was prepared by dissolving 8 grams (4 grams for the $Bi_2Fe_4O_9$ synthesis) of bismuth nitrate and 6 grams of iron nitrate in 20 ml 2-methoxyethanol. The solution was stirred for 30 mins to dissolve the powders. 10 ml acetic anhydride was added later and stirred for 60 mins. The whole process was carried out in an ambient atmosphere at room temperature.

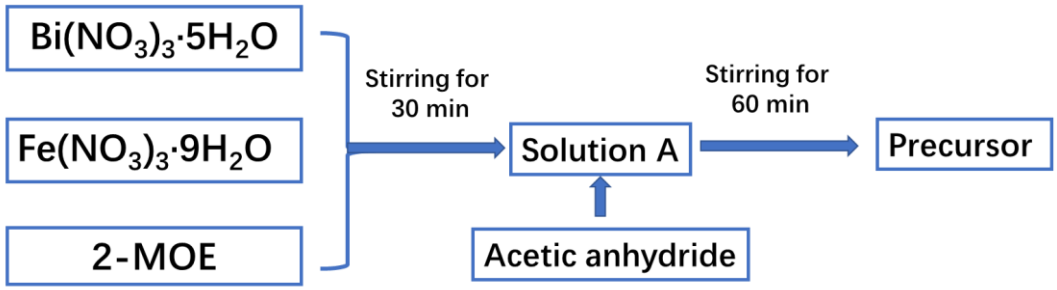


**Figure 3.1 Flow chart of precursor preparation for bismuth ferrite thin films synthesis.**

Chemicals used for preparation of the precursor solutions are listed in Table 3.1. The nitrates (bismuth and iron) were stored in a vacuum desiccator to avoid absorption of water into the chemicals.

**Table 3.1 Chemicals for bismuth ferrite precursor preparation**

| Chemical Name | Chemical Formula | Specification | Supplier |
|---|---|---|---|
| Bismuth nitrate pentahydrate | $Bi(NO_3)_3 \cdot 5H_2O$ | ≥ 98% | Sigma-Aldrich, UK |
| Iron nitrate nonahydrate | $Fe(NO_3)_3 \cdot 9H_2O$ | ≥ 98% | Sigma-Aldrich, UK |
| 2-Methoxyethonal (2-MOE) | $C_3H_8O_2$ | 99.8% | Sigma-Aldrich, UK |
| Acetic anhydride | $C_4H_6O_3$ | ≥ 99% | Sigma-Aldrich, UK |

### 3.1.1.2. Film deposition

The substrate used in this thesis for film deposition is fluorine doped tin oxide coated float glass (FTO, Tec 15 Pilkington). The FTO glass was cut to 1 cm *1.5 cm and cleaned by sonication in acetone and 2-proponal for 15 min each before dried with nitrogen flow. Bismuth ferrite gel films were prepared by dropping 50 μL of precursor solution onto the FTO glass and then spin-coating at 3000 rpm for 30 s. A digitally-controlled spin coater (G3P Spin Coater, Specialty Coating Systems Inc.) was used in this thesis. The spin coater uses a vacuum specimen stage to secure the substrate for spinning as well as a programmable control system for spin velocity and duration. After deposition, the sample was removed from the spin coater and heated in air on a hot plate at 90 ℃ for 1 min for gelation and then subsequently heated at 350 ℃ for 5 minutes for drying. After then it was cooled down at 90 ℃ for 1 min again. This step was repeated 5 times to get a desired

film thickness (of ~ 150 nm).

#### 3.1.1.3. Film heat treatment

Heat treatment of the film was done in a tube furnace. The samples were transferred into a tube furnace after heat treatment at 350 ℃ and heated up by 5 ℃/min to 450 ℃ with a dwell time of 30 min before heating to 650 ℃ with a ramp rate of 5 ℃/min and held for 1 hour. The samples were then cooled down within the furnace naturally. Different atmospheres have been applied depending upon the experiment requirements. The illustration of the key steps for film preparation is shown in Figure 3.2.

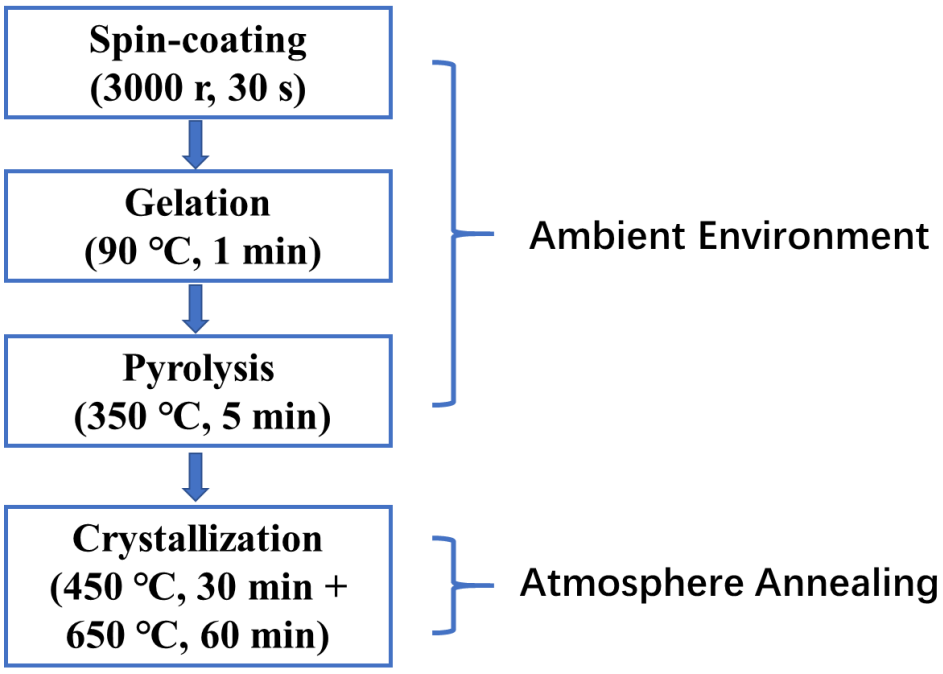


**Figure 3.2 Flow chart of the bismuth ferrite film deposition and annealing treatment procedure.**

### 3.1.2. Barium strontium titanate powder synthesis

Molten-salt synthesis (MSS) method was used to prepare barium strontium titanate powder in this thesis. In a typical synthesis procedure of $Ba_{0.8}Sr_{0.2}TiO_3$, 0.08 mol of $BaC_2O_4$ and 0.02 mol $SrC_2O_4$ along with 20 mol NaCl and 20 mol KCl were mixed together. The mixture was mixed thoroughly by ball milling for 4 h with adding of ethanol. And then the mixture was dried out at 100 ℃ over night. The processed mixture was placed in a ceramic crucible, heated at a ramp rate of 5 ℃/min to an annealing temperature at 750 ℃ for 1 h, and cooled thereafter to room temperature within the furnace. Samples were then washed several times with hot distilled water and filtered by vacuum suction. The as-prepared powders were collected and dried at 80 ℃ in an oven overnight. Preparation of $Ba_{0.2}Sr_{0.8}TiO_3$ powders was employed using different molar ratios of the initial precursors. $Ba_{0.8}Sr_{0.2}TiO_3$ samples prepared at 750 ℃ were post-annealed at 950 ℃, 1200 ℃ and 1350 ℃ to investigate the effect of grain size on the domain structure later. The post-annealing treatment was conducted by heating the $Ba_{0.8}Sr_{0.2}TiO_3$ samples up to the desired temperature by a rate of 10 ℃/min and held for 10 hours, followed by cooling down in a rate of 5 ℃/min. If not noticed specifically, the $Ba_{0.8}Sr_{0.2}TiO_3$ samples mentioned in the later chapter refer to the original samples processed at 750 ℃. A flow chart illustrating the steps of MSS method and the factors influencing the molten-salt synthesis of metal oxide materials is shown in Figure 3.3.

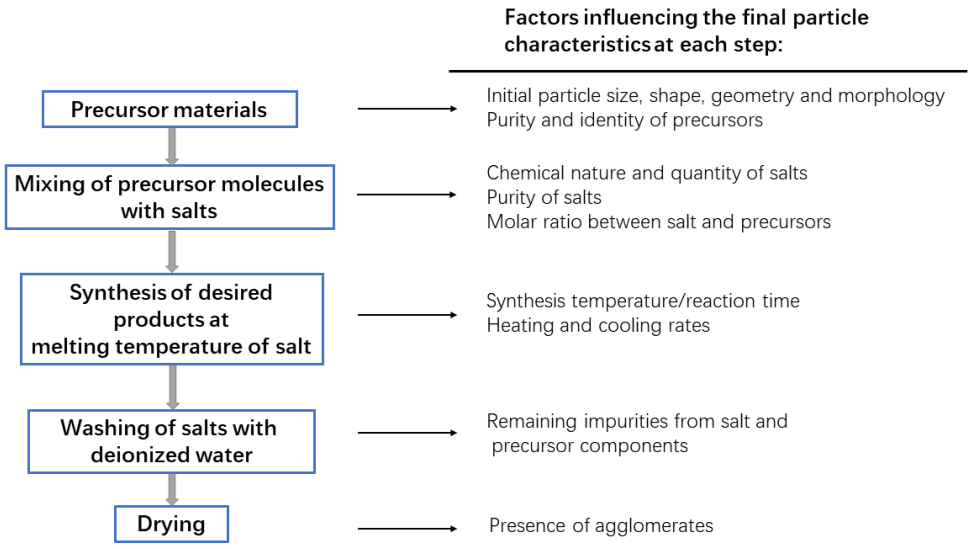


**Figure 3.3 Flow chart illustrating factors influencing the molten-salt synthesis of metal oxide materials[108].**

**Table 3.2 Chemicals for $Ba_xSr_{1-x}TiO_3$ synthesis**

| Chemical Name | Chemical Formula | Specification | Supplier |
|---|---|---|---|
| Barium oxalate | $BaC_2O_4$ | 99.999% | Alfa Aesar, UK |
| Strontium oxalate | $SrC_2O_4$ | 95% | Alfa Aesar, UK |
| Sodium chloride | NaCl | 99.0% | Alfa Aesar, UK |
| Potassium chloride | KCl | 99% | Alfa Aesar, UK |

Chemicals used for preparation of the $Ba_xSr_{1-x}TiO_3$ nanopowders are listed in Table 3.2. The barium and strontium oxalate were stored in a vacuum desiccator to avoid absorption of water into the chemicals.

## 3.2. **Materials Characterisation Techniques**

### 3.2.1. Scanning electron microscope

Scanning electron microscope (SEM, FEI Inspect F) is used to provide the sample information include the morphology, chemical composition and crystalline structure. It uses a focused beam of high-energy electrons to form a range of signals at sample surface. SEM can detect the sample from a micrometer (μm) to nanometer (nm) scale.

Morphologies of the as-prepared bismuth thin films and barium titanate powders were characterised by SEM. For bismuth ferrite film samples, both of the top view and cross section view were characterised. For the top view characterisation, the sample was attached on top of the carbon tape with the conductive edge of the FTO glass connected to the carbon tape, without further surface treatment. For the cross section view, the sample was cut in the middle and attached to the carbon tape with the section facing up. A thin layer of gold was deposited on the top then by plasma deposition method for better scanning image. For $Ba_xSr_{1-x}TiO_3$ powders, they were attached onto the carbon tape with further sputtering of gold as well.

### 3.2.2. Transmission electron microscopy

Transmission electron microscopy (TEM, JEOL 2010) provides imaging and diffraction characterisation of the sample. It is a microscopy technique which uses a high energy beam of electrons to transmit through a ultrathin sample. The interactions between the electrons and the atoms can give out the information of the crystal structure on the atomic scale. Information about local structure, average structure and chemical composition can be collected simultaneously.

TEM technique was used in this study to characterise the crystallographic structure of the as-prepared $Ba_xSr_{1-x}TiO_3$ samples. The samples for TEM characterisation were prepared by dispersing a small amount of the $Ba_xSr_{1-x}TiO_3$ powders into ethanol and followed by ultrasonication for 15 min. Then the suspension was dropped on the copper grid and left at room temperature to dry.

### 3.2.3. X-ray diffraction analysis

X-ray diffraction (XRD, Panalytical Xpert Pro diffractometer) is used to study the crystal structure and phase composition of the crystalline materials. It can identify phases through comparison with data from known structures and quantify changes in the

structural parameters. X-radiation is electromagnetic radiation which has a wavelength between ~ 0.1 Å to 100 Å (Cu Ka = 1.54 Å is commonly used). It is in the same magnitude of the interatomic distances in a crystal, making it convenient for crystal structures to diffract X-rays. The interaction of the incident X-rays with the sample generates constructive interference when conditions satisfy Bragg's Law:

$$n\lambda = 2d_{hkl} \sin \theta \qquad \text{Eqn (3.1)}$$

Bragg's Law relates the wavelength of the electromagnetic radiation to the diffraction angle and the lattice spacing in a sample. By scanning the sample through a range of 2θ angles, all possible diffraction directions of the lattice can be attained and the associated diffracted X-rays can be recorded. Figure 3.4 shows a schematic view of the X-ray diffraction from the crystal lattice planes.

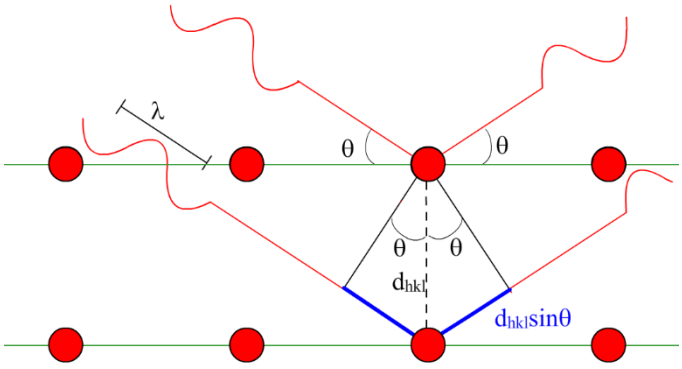


**Figure 3.4 The schematic illustration of X-ray diffraction in crystal lattice following the Bragg's Law.**

The phase composition of the bismuth ferrite films and $Ba_xSr_{1-x}TiO_3$ powders were investigated by XRD using with Cu-Ka radiation in this study. A continuous scan mode was used for all the sample characterisation.

### 3.2.4. X-ray photoelectron spectroscopy

X-ray Photoelectron Spectroscopy (XPS, Thermo Scientific K-Alpha) is a technique used to analyze the surface chemistry of a material. It can reveal the elemental composition, chemical state and electronic state of the elements within a material. When a material is irradiated under the X-ray beam, electrons will emit from the material surface (the top 1-10 nm) and their kinetic energy can be measured and recorded. The XPS spectra are then obtained by recording ejected electrons over a range of electron kinetic energies.

The XPS spectra of the bismuth ferrite films and $Ba_xSr_{1-x}TiO_3$ powders were analysed using the CasaXPS software. All the binding energies were calibrated to C 1s peak at 284.6 eV.

### 3.2.5. Kelvin Probe (KP) and ambient pressure x-ray photoelectron spectroscopy (APXPS)

Kelvin Probe (KP) and ambient pressure x-ray photoelectron spectroscopy (APXPS) have

been used to make an accurate measurement of the band structure of $BiFeO_3$ film. APXPS can determine the VBM of a material and KP can measure the surface Fermi level of the sample. The same sensor is used for both KP and APXPS measurements. A schematic view of the KP (a) and APXPS (b) measurements is shown in Figure 3.5.

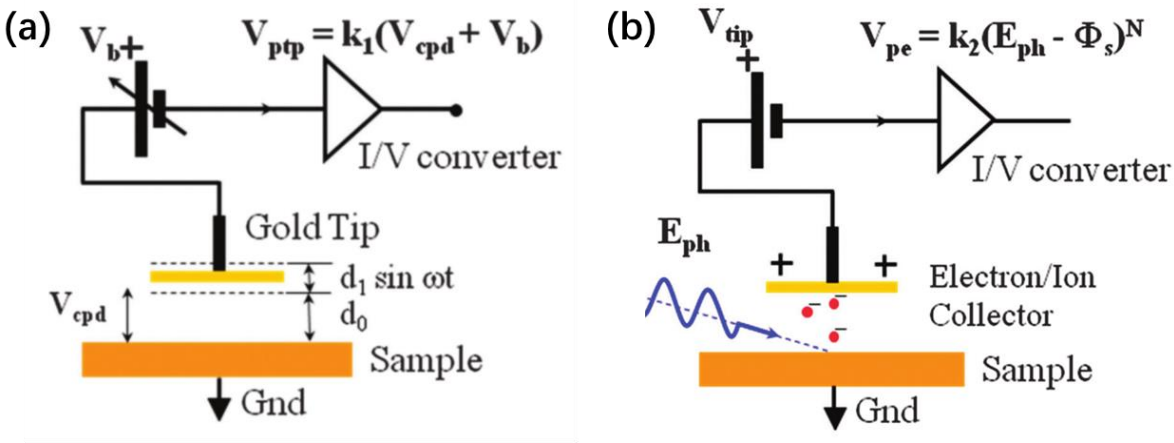


**Figure 3.5 (a) Kelvin probe measurement (b) Ambient pressure x-ray photoelectron spectroscopy[109].**

Kelvin probe measurement can give out the Fermi level position of a material by measuring the contact potential difference ($V_{cpd}$) between the inner face of the vibrating tip and the sample surface. APXPS is a x-ray photoelectron spectroscopy conducted at near-ambient pressure. Different from conventional XPS, which usually carried out under a high vacuum condition ($10^{-6}$ – $10^{-10}$ mbar), the APXPS works under near-ambient pressure in a range of $10^{-4}$ – $10^{2}$ mbar. Under ambient pressure, the photo-emitted electrons have very short mean free path (~ 1 μm) and can not reach the detector. So the

electrons will be stopped close to the sample surface and a cloud of charge will build up (ions such as $N^{2-}$ , $OH^-$ and $O^{2-}$). These ions can go to the sensor electrode to create a measurable current, which is the emitted photocurrent and then gives out the value of VBM.

### 3.2.6. Brunauer-Emmett-Teller surface area measurement

The Brunauer-Emmett-Teller surface area measurement (BET, Micromeritics Gemini VII) is used to measure the specific surface area of a material by physical adsorption of gas molecules on the solid sample surface.

The BET surface area of $Ba_xSr_{1-x}TiO_3$ powders were analyzed in this study. The samples were dried for more than 12 hours at 200 ℃ in $N_2$ atmosphere and then loaded into separated tubes. An empty tube was used as a reference. $N_2$ atmosphere was used during the whole measurement.

### 3.2.7. UV-Vis spectroscopy

UV-vis Spectrometer (Perkin Elmer, Lamda 950) was used to obtain the absorption and reflectance spectra of the as-prepared bismuth ferrite films, $Ba_xSr_{1-x}TiO_3$ powders and the dye solution used in photo degradation tests. The UV-vis spectra can give out the light

absorption/reflectance information of bismuth ferrite and $Ba_xSr_{1-x}TiO_3$, thus the derived band-gaps of the materials. It can also give out the light absorption information of the dye solution which can be used to monitor its concentration changes during the degradation test.

For bismuth ferrite films, the absorption spectra data was used as obtained. And the optical band gap ($E_g$) of the samples was calculated using the Tauc relationship[110]:

$$(ahv)^n = A(hv - E_g) \qquad \text{Eqn (3.2)}$$

where $A$ = constant, $hv$ = light energy, $E_g$ = optical band gap energy, $a$ = measured absorption coefficient, n = 0.5 for indirect band gap and n = 2 for direct band gap materials.

For $Ba_xSr_{1-x}TiO_3$ powders, reflectance spectra were obtained first and then converted to absorbance spectra using the Kubelka Munk transformation equation:

$$F(R) = (1-R)\ (1-R)/2R = K/S \qquad (R = \%R\ /100) \qquad \text{Eqn (3.3)}$$

And the optical band gap was obtained by plotting F(R) against energy $hv$, the same procedure as that used for bismuth ferrite films.

For dye solution (Rhodamine B used in this study), absorption spectra of the solution of different concentration were first obtained and then related to its concentration change. Typically, 1.5 ml of the dye solution sample was put into a cuvette (semi-micro, PMMA) for the UV-vis test.

### 3.2.8. Raman spectroscopy

Raman spectroscopy (Horiba Lab-RamiHR550 spectrometer) is used to provide information of the structure, symmetry, electronic environment and bonding of the molecules[111]. It is an optical technique based on inelastic scattering of the light, known as the Raman effect. The scattered light has a different frequency from the incident light in the inelastic scattering, and this will lead to a shift in wavelength depending on the chemical structure of the molecules responsible for scattering.

A schematic diagram of the Raman effect is presented in Figure 3.6. When a molecule is under irradiation of a monochromatic light, two types of light scattering can happen. Most of the scattering is an elastic process with no change in energy, termed as the Rayleigh scattering. A small percentage of the scattering is an inelastic process and it is termed as Raman scattering (Raman effect). The Raman scattering can have two forms. One is the Stokes Raman scattering (Figure 3.6b) and the other is the Anti Stokes Raman scattering

(Figure 3.6c). The scattered light in the former one has an lower energy than the incident light while that in the later one has an higher energy than the incident light.

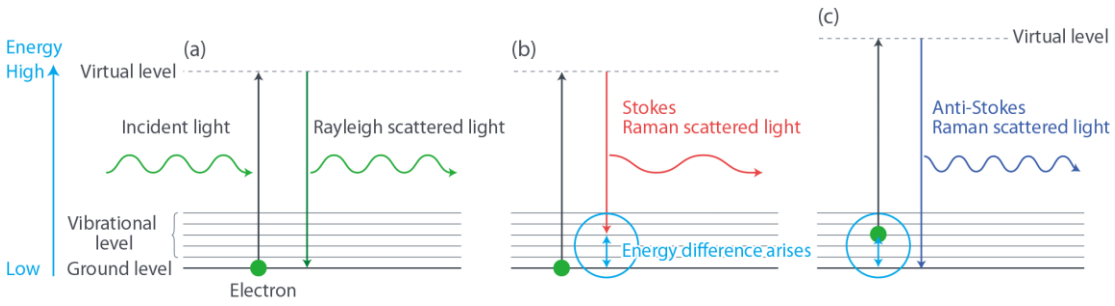


**Figure 3.6 Schematic illustration of Rayleigh scattering (a) and Raman scattering (b) and (c).**

### 3.2.9. Differential scanning calorimetry

Differential Scanning Calorimeter (DSC, Perkin Elmer TA Instruments DSC 25) is used to detect the physical or chemical transitions happened during material heating or cooling process such as melts, glass transitions and phase changes. It is a thermal analysis technique that measures the heat flow rate to or from a sample when it is subjected to a controlled temperature program in a controlled atmosphere.

The dependence of phase transition behavior on grain size of barium strontium titanate particles was investigated by DSC measurements in this thesis. The specimens were prepared by placing 10 – 20 mg sample powders into the aluminum DSC pans. The samples were heated from – 20 ℃ up to 140 ℃ by a rate of 5 ℃/min and held for

2 minutes, a cooling down process was followed then with a rate of 5 ℃/min to - 20 ℃ and held for 5 minutes as well. The whole procedure was repeated again for an accurate measurement.

### 3.2.10. Piezoresponse Force Microscopy (PFM)

Piezoresponse Force Microscopy is used to characterise the piezoelectric or ferroelectric properties of the materials, specifically the domain structure of $BiFeO_3$ film in this study. The PFM facility is constructed by an Atomic Force Microscope (AFM, NT-MDT, Russia) and piezo-response accessories. A Pt coated probe (Windsor Scientific Limited, UK) with a spring constant of 5 N/m was used in contact mode. Figure 3.7 shows the principle of PFM operation. Electrical stimulus will be applied to the sample surface and in response to it, the sample will expand or contract. A laser beam is focused on the backside of the cantilever and reflected to a photodiode detector. When the sample surface is scanned by the probe, the mechanical response will induce a displacement of the cantilever, the associated displacement of the laser spot will be recorded by the detector. In this way the piezoelectric response of the sample can be detected and imaged. The polarization switching in ferroelectrics can be achieved by applying a DC bias on the tip, which can locally pole the sample and probe the corresponding electromechanical responses.

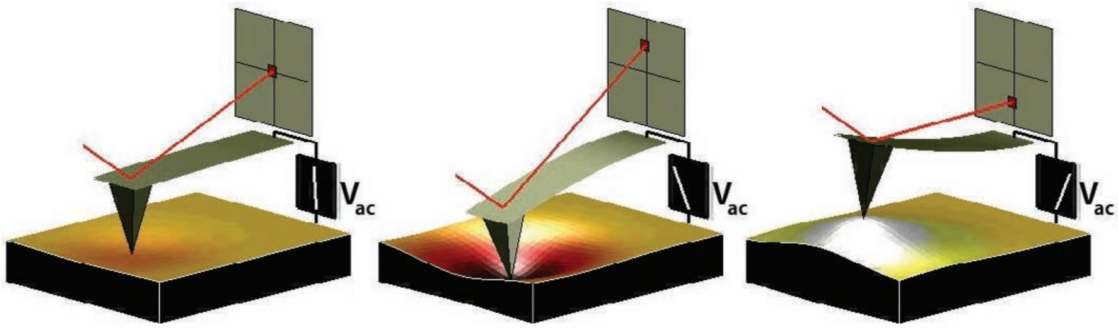


**Figure 3.7 Principle of PFM operation[112].**

## 3.3. Photocatalytic Activity Characterisation

### 3.3.1. Photoelectrochemical measurements

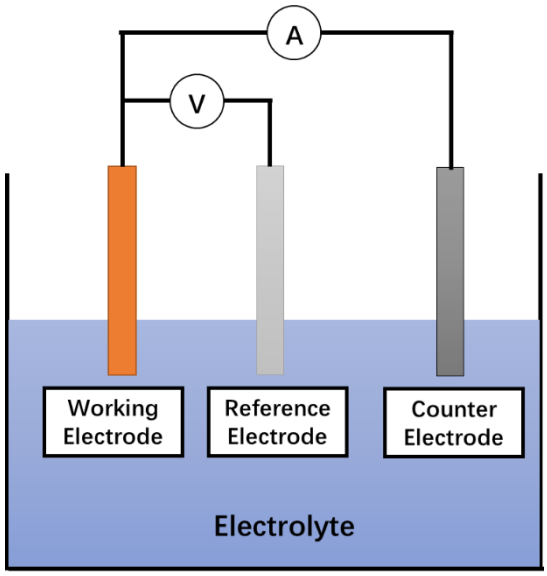


**Figure 3.8 Schematic illustration of a potentiostat with three electrodes.**

All photoelectrochemical measurements were conducted using a potentiostat (Gamry

Interface 1000). A three-electrode cell system (Figure 3.8) was used with the as-prepared bismuth ferrite films as the working electrode, Ag/AgCl as the reference electrode and a Glassy Carbon Rod as the counter electrode. $Na_2SO_4$ solution was used as the electrolyte (0.2 M, pH equals 6.5). A solar simulator (Sciencetech, Class: ABA) with an AM 1.5 filter was used for illumination of the system.

Mott-Schottky measurements were obtained from the following equation[11]:

$$\frac{1}{C^2} = \left(\frac{2}{e\varepsilon\varepsilon_0 N_d}\right)[V_a - V_{fb} - kT/e] \qquad \text{Eqn (3.4)}$$

where $C$ is the space charge layer capacitance, $\varepsilon$ is the dielectric constant of the material, $\varepsilon_0$ is the permittivity of the vacuum, e is the elemental charge, $N_d$ is the concentration of the charge carriers, $V_a$ is the applied potential, $V_{fb}$ is the flat band potential, $k$ is Boltmann's constant, and $T$ is temperature. The flat band potential ($V_{fb}$) was determined by taking the x intercept of a linear fit to the Mott-Schottky plot, $1/C^2$, as a function of applied potential ($V_a$) .

The measured potential vs. the Ag/AgCl reference electrode was converted into the normal hydrogen electrode (NHE) scale after electrochemical measurements using the Nernst equation:

$$E_{NHE} = E_{Ag/AgCl} + E_{Ag/AgCl}^{0}$$

$$E_{Ag/AgCl}^{0} \text{ (3.0 M KCl)} = 0.209 \text{ V at } 25\ ^{\circ}C$$

The cell used for the PEC test was designed specially, which consists of two parts (Figure 3.9): a metal plate to attach the sample and a Teflon chamber for the electrolyte solution. The bismuth ferrite film samples were attached onto the metal plate with the film side facing upside by a silver paint. One edge of the substrate had been covered by the Kapton tape during spin coating to leave the space for the silver paint. A small hole was designed on the chamber for the electrolyte to touch the sample, which is the actual working area of the sample. A rubber o-ring was placed into the hole to prevent electrolyte leakage. The metal plate was fixed to the chamber by two screws.

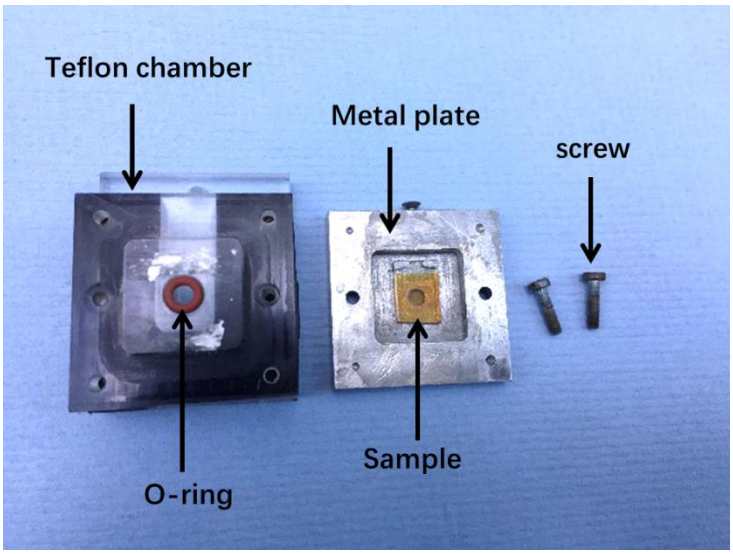


**Figure 3.9 PEC cell**

The cell was clamped to a retort stand and placed with the metal side facing the solar simulator. The diameter of the hole is 4 mm, which is an area of 0.125 $cm^2$. An illustration

of the PEC test system including the PEC cell, potentiostat and the solar simulator and their connection configuration is shown in Figure 3.10.

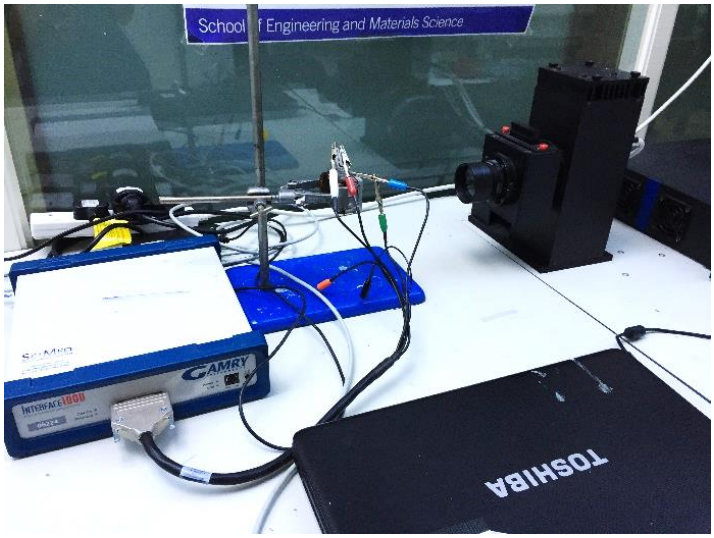


**Figure 3.10 Illustration of the PEC test system.**

### 3.3.2. Dye degradation

Photodegradation of Rhodamine B (Rh B) was used to evaluate the photocatalytic activity of the barium strontium titanate. The chemical structure of Rh B is shown in Figure 3.11. The Rh B solution with a concentration of 10 ppm was used. Degradation of Rh B was conducted in a quartz petri dish. 0.15 g barium strontium titanate powder was mixed with 50 ml of the dye solution (Figure 3.12). The mixture was stirred under dark for 30 minutes firstly. And then it was placed under the solar simulator (Newport, class ABB) for degradation test. An amount of 1.5 ml of the solution was taken for sampling at fixed

intervals. And centrifugation was carried out later to remove the catalyst powders from the degradation samples. Generally a program of 10000 rpm for 15 minutes was used for the centrifugation.

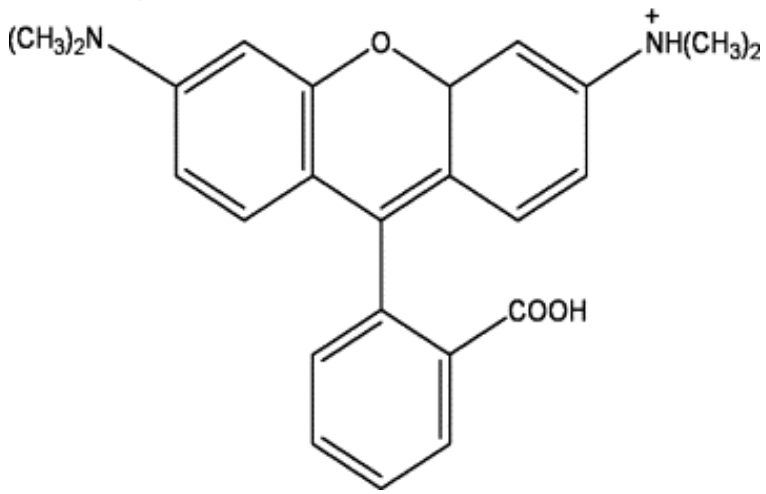


**Figure 3.11 Chemical structure of Rh B.**

**Figure 3.12 Degradation of Rh B using $Ba_xSr_{1-x}TiO_3$ powders.**

# Chapter 4 Origin of the Switchable Photocurrent Direction in $BiFeO_3$ Thin Films

## 4.1. Introduction

Application of ferroelectric semiconductors in solar energy conversion has aroused increasing interests in recent years. The internal electric field present in ferroelectric materials can help to aid the separation of photoexcited charge carriers and improve the energy conversion efficiency. As reviewed in section 2.3.1, $BiFeO_3$ is a room temperature ferroelectric, and has a narrow band gap of c.a. 2.1 to 2.8 eV, making it the most interested ferroelectric photocatalyst. Previous studies on the structural, optical and electrical properties of $BiFeO_3$ showed that it is an intriguing and complex material with a range of contradictory information reported such as the varying band positions, indirect/direct band gap and p or n type conductivity. Unlike typical semiconductor photoelectrodes, which can only produce one type of photocurrents – either anodic or cathodic, both of $BiFeO_3$ photoanodes and photocathodes have been reported previously. It is of great interest to investigate the photocatalytic behavior of $BiFeO_3$ photoelectrode – whether it is an n-type or p-type semiconductor and the underlying origin of its unique performance. In this chapter, $BiFeO_3$ thin film was deposited on conductive FTO glass substrate for the application as a photoelectrode and its photocatalytic behavior has been investigated.

# Chapter 4

Switchable photocurrent was observed in the as-prepared $BiFeO_3$ photoelectrode and the origin of the ambipolar behavior has been studied.

Switchable photocurrent polarity under various stimuli is an important subject for the development of advanced optoelectronic systems, logic devices and selective energy conversion approaches[113-116]. This specific property usually can be realized in molecular, hybrid, and inorganic nanoparticle material systems[114,115,117,118]. For example, it was demonstrated that molecular photodiode systems can switch photocurrent direction under different wavelength irradiating light[115], and hybrid systems such as composites of Titania nanosheets and polyaniline layers exhibited an n- to p-type switchable photoelectrode behavior by varying the applied potentials[117]. Semiconductor thin film photoelectrode consisting of n-type $Fe_2O_3$ and p-type $CuFeO_2$, which are phase separated into microdomains, also showed tunable photoresponses under varying bias[114]. The principle behind this is the control of charge carrier separation directions based on different interfaces such as substrates, surfaces and the junctions formed between them.

In a PEC system with photoelectrode of single phase material, switchable photocurrents are rarely observed. This is because for a typical n-type or p-type semiconductor, only one direction of band bending at the semiconductor/electrolyte solution interface (upward band bending for n-type and downward for p-type) can arise to form sufficient depletion

region for charge carrier separation[9,119,120]. Combination of the two features in one electrode with ease of fabrication and active PEC performance remains a challenge due to complexities existed in multi-material systems design and fabrication.

## 4.2. **Characterisation of $BiFeO_3$ Thin Film**

The surface morphology of the $BiFeO_3$ film is presented in Figure 4.1. The SEM image shows that the grains are approximately 50-200 nm in size and form a homogeneous and compact layer on the substrate. XRD pattern of the $BiFeO_3$ film is shown in Figure 4.2, which indicates that the as-prepared film is of high phase purity with a rhombohedral structure (ICDD 14-0181; space group: *R3c*).

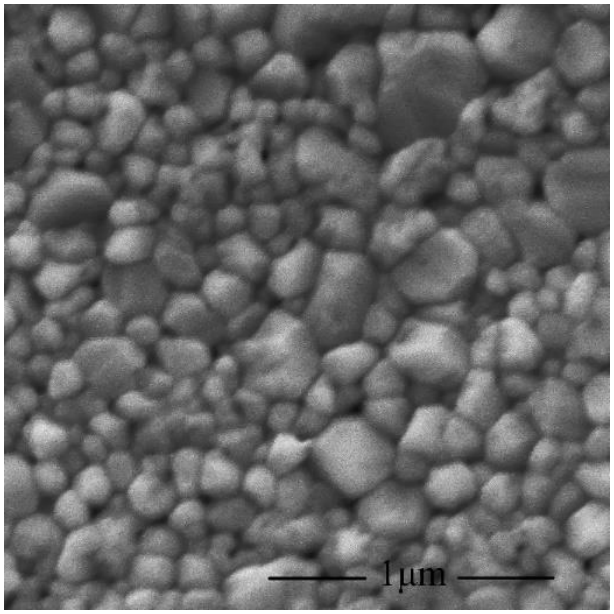


**Figure 4.1 SEM image of the $BiFeO_3$ film**

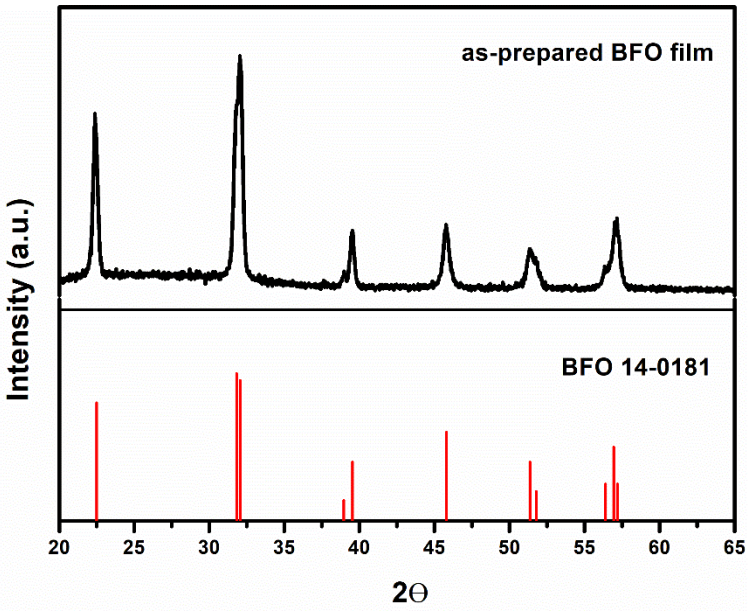


**Figure 4.2 XRD patterns of the $BiFeO_3$ film**

The optical properties of the as-prepared $BiFeO_3$ film were investigated by UV-vis spectroscopy. Figure 4.3a shows the UV-vis absorption spectrum of the $BiFeO_3$ thin film. The absorbance curve goes through a slow increase from a wavelength of about 550 nm then a sharp increase from about 450 nm. The linear regions in the derived Tauc plots (Figure 4.3b) indicate that the indirect and direct allowed band gaps are 2.3 and 2.7 eV.

$BiFeO_3$ can be viewed as a charge-transfer insulator, with the bandgap controlled by the orbital overlap between the O 2p and the Fe 3d levels[80]. According to previous studies[121], the valence band maximum of $BiFeO_3$ is rather flat, whereas the conduction band minimum can be varied due to the possible momentum shift induced by the hybridization

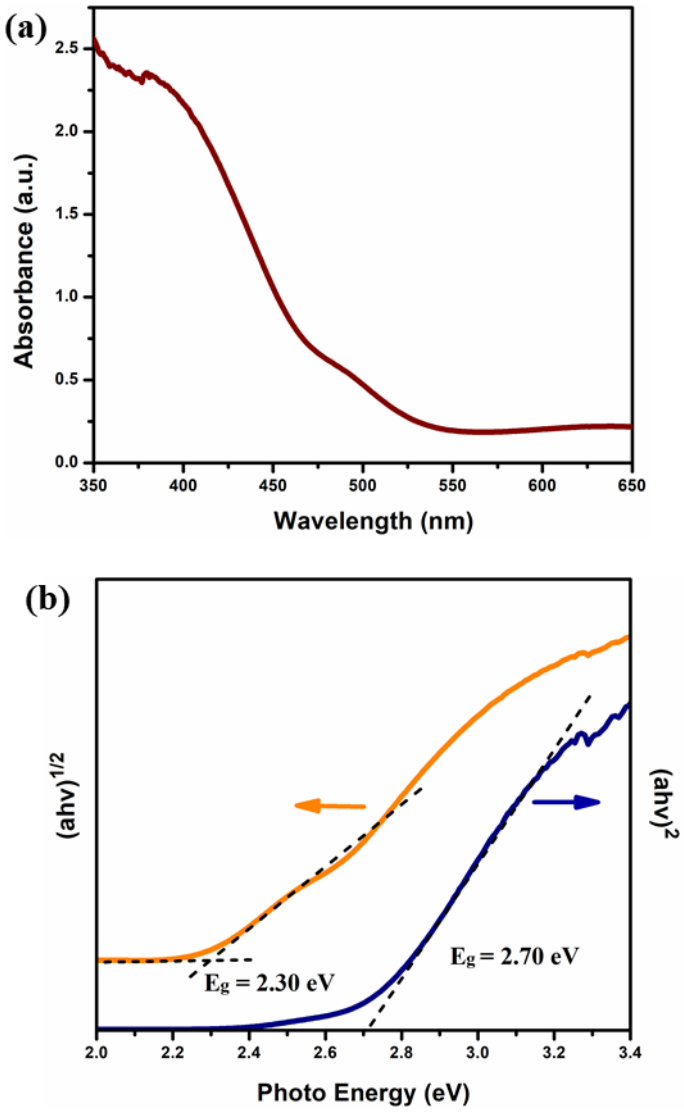


**Figure 4.3 (a) UV-vis absorption spectrum of the $BiFeO_3$ film. (b) Tauc plots for indirect (orange) and direct (blue) allowed transitions.**

between the orbital states and the valence state of Fe, which is dependent on oxygen vacancies and stoichiometry. Therefore, a wide range of band gaps, from 2.1 eV to 2.8 eV, have been reported for $BiFeO_3$ thin films where both indirect/direct band gap characteristics have been observed[121,122]. The study by R. Palai *et. al*[122] showed that at

room temperature (RT) $BiFeO_3$ has an indirect bandgap with direct gap lies only about 0.05 eV above it and the gap becomes more direct with increasing T. It can be interpreted that there exist both direct and indirect photoexcitation of electrons at RT in $BiFeO_3$, with the indirect charge transfer dominating. Therefore the observed indirect optical bandgap of 2.3 eV will be applied in the next part for the bandgap structure discussion.

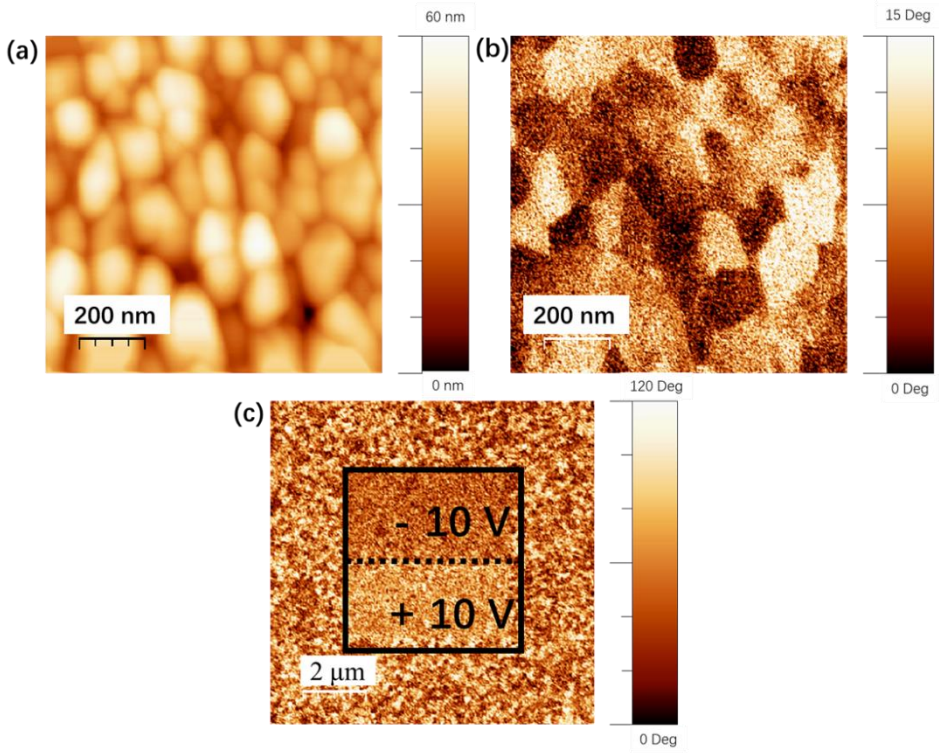


**Figure 4.4 (a) Topography image of $BiFeO_3$ (b) PFM phase image of $BiFeO_3$ (c) PFM phase image of a polarization pattern of $BiFeO_3$ film after writing by DC bias with – 10 V and + 10 V.**

Ferroelectric properties of the as-prepared $BiFeO_3$ film were characterised using PFM. Figure 4.4 (a) shows the topography image of the $BiFeO_3$ film. Figure 4.4 (b) shows the

phase image of the $BiFeO_3$ film. It can be seen from the phase image that the as-prepared $BiFeO_3$ has a single-grain single-domain structure. Figure 4.4 (c) shows domain switching behavior of the $BiFeO_3$ film. A 5 μm × 5 μm square region in the center of the image was switched by applying a DC bias of + 10 V on the bottom half part and – 10 V on the top half part, demonstrating the ferroelectric nature of the as-prepared $BiFeO_3$ film.

## 4.3. **Photoelectrochemical Measurements**

Current density *vs.* applied potential plots under chopped light for $BiFeO_3$ electrode in $Na_2SO_4$ and $Na_2SO_4$-$H_2O_2$ electrolytes are presented in Figure 4.5. Surprisingly, both cathodic and anodic photocurrents were observed in the applied potential ranging from - 0.3 to 1.7 $V_{NHE}$. $H_2O_2$ was chosen here as a hole scavenger, with higher rate constant for oxidation than water and a relatively negative reduction potential ($E^0$ = +0.68 $V_{RHE}$ for the $O_2/H_2O_2$ couple) than that of water ($E^0$ = 1.23 $V_{RHE}$ for the $O_2/H_2O$ couple)[18]. By efficiently collecting all holes arrived at the electrode/electrolyte interface, the addition of $H_2O_2$ in electrolyte can help to find out the on-set potential of the photocurrents, the value of which is usually shifted anodically due to the slow carrier transfer kinetics in aqueous electrolyte solution. With the addition of $H_2O_2$, the photocurrents switch point, which is the on-set potential for both of the anodic and cathodic photocurrents, can be seen from the plot, with a value of 0.3 $V_{NHE}$. On-set

potential of the photocurrents is correlated to the flat band potential of the photoelectrode, which indicates the starting position of band bending. Therefore, the switch point potential here can indicate the Fermi level position of the as-prepared $BiFeO_3$ electrode, which is roughly around 0.3 $V_{NHE}$.

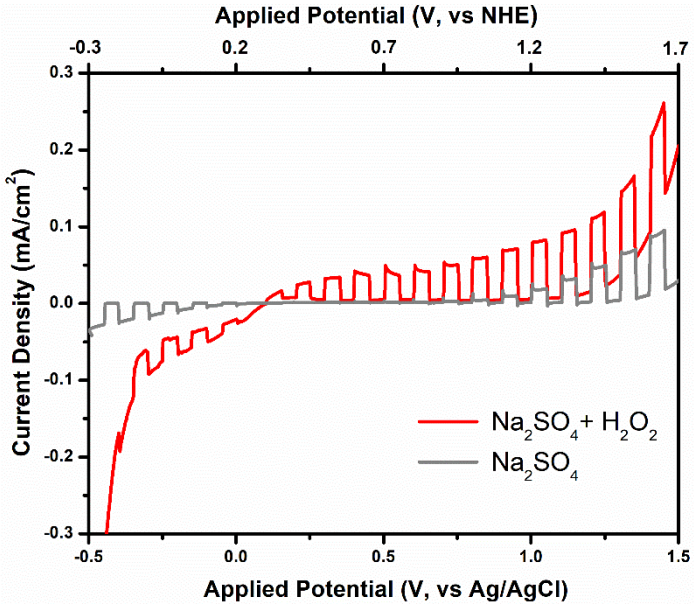


**Figure 4.5 Current density vs. applied potential plots under chopped light of the $BiFeO_3$ electrode in either 0.2 M $Na_2SO_4$ or 0.2 M $Na_2SO_4$-0.5 M $H_2O_2$.**

Generally, cathodic photocurrents can be generated in p-type semiconductors and anodic photocurrents in n-type semiconductors. The reason that no cathodic photocurrents generation in an n-type semiconductor is that in a typical n-type semiconductor, the Fermi level position is very close to its CBM (~ 0.2 eV)[11,123]. At potentials negative of its flat band potential, the band bending suffices to force the Fermi energy into the band, there

will be excess of majority charge carriers injected to the space charge region and an accumulation region will be formed instead of the depletion region. At this situation, the so-called 'degenerate surface' will be formed and the semiconductor electrode will behave like a metal electrode and have a large carrier transfer no matter in the dark and under illumination, there will be no effective photocurrent generated[9,119,124,125]. An inverse but analogous situation occurs in a p-type semiconductor.

However, the $BiFeO_3$ photoelectrode here shows both cathodic and anodic photocurrents varying with applied potentials. It indicates that two depletion regions are formed under the varying applied potentials. This is quite different from typical semiconductor photoanodes as that has been reported in the studies of $TiO_2$[126], $BiVO_4$[127], $Fe_2O_3$[128], or representative photocathodes of Cu-based compounds such as $CuBi_2O_4$ and $CuFeO_2$[129,130]. Based on the PEC results, it can be assumed that the as-prepared $BiFeO_3$ film possess a Fermi level position near the middle of the band gap. To verify our assumptions, Kelvin Probe (KP) and ambient pressure x-ray photoelectron spectroscopy (APXPS) characterisation have been carried out to obtain the VBM and Fermi level of $BiFeO_3$ film. The results are shown in Table 4.1. Among them, the band gap was obtained by UV-vis characterisation, VBM was obtained from APXPS and Fermi level was from KP characterisation, and CBM and middle of bandgap were calculated using the other values. The measured Fermi level position of the $BiFeO_3$ film is 0.46 $V_{NHE}$, very close to the

middle of band gap (0.43 $V_{NHE}$). The measured Fermi level position is slightly positive than the evaluated value (0.3 $V_{NHE}$ ) from on-set potential of the photocurrents. The reason for it needs further study. Here we will use the measured value for the discussion of next parts. However, it is worth noted that both of the values support the assumption of the formation of two depletion regions. With these information, a band diagram of the as-prepared $BiFeO_3$ film has been drawn and depicted in Figure 4.6.

**Table 4.1 Band positions of $BiFeO_3$ film**

| Band gap | VBM | CBM | Middle of Bandgap | Fermi level |
|---|---|---|---|---|
| 2.3 eV | - 6.08 $V_{VAC}$/ 1.58 $V_{NHE}$ | - 3.78 $V_{VAC}$/ - 0.72 $V_{NHE}$ | - 4.93 $V_{VAC}$/ 0.43 $V_{NHE}$ | - 4.96 $V_{VAC}$/ 0.46 $V_{NHE}$ |

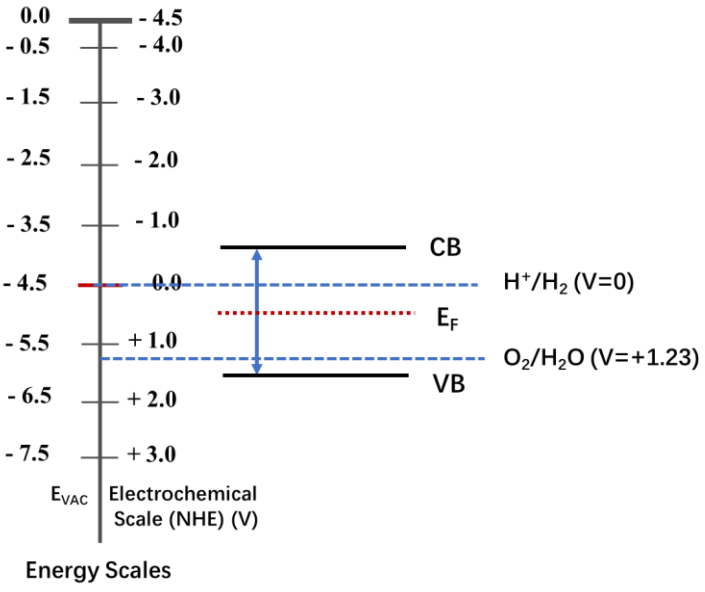


**Figure 4.6 Band diagram of $BiFeO_3$ film.**

With the KP and APXPS results, the schematic band diagrams of the $BiFeO_3$

photoelectrode in an electrolyte ($Na_2SO_4$ solution) can be depicted as that in Figure 4.7 **错误!未找到引用源。. 错误!未找到引用源。**a is the $BiFeO_3$ electrode band positions before its contact with the electrolyte solution, with no charge transfer thus no band bending. When the electrode comes into contact with the electrolyte solution, electrons will transfer from/to the electrolyte to achieve an equilibrium at which the Fermi level of the electrode is the same as the redox potential of the electrolyte. Upward band bending then arises followed by the formation of the depletion region, as it depicted in Figure 4.7b. Under potentials positive of the flat band potential, Fermi level shifts more positively and the upward band bending increases (shown in Figure 4.7c). As a result, the depletion region increases, and the photoexcited charge carriers will be separated more efficiently and increased photocurrents will be observed. Figure 4.7b and Figure 4.7c is the schematic generation of anodic photocurrents from the view of band diagrams variation, which is the typical procedure for an n-type semiconductor. Since the $BiFeO_3$ photoelectrode has a near-middle-bandgap Fermi level position, a depletion region can also be formed by downward band bending, as shown in Figure 4.7d. That means, when the applied bias becomes more negative than the flat band potential, the $BiFeO_3$ electrode will behave as a photocathode, generating cathodic photocurrents and showing characteristic of a ‘p’ type semiconductor.

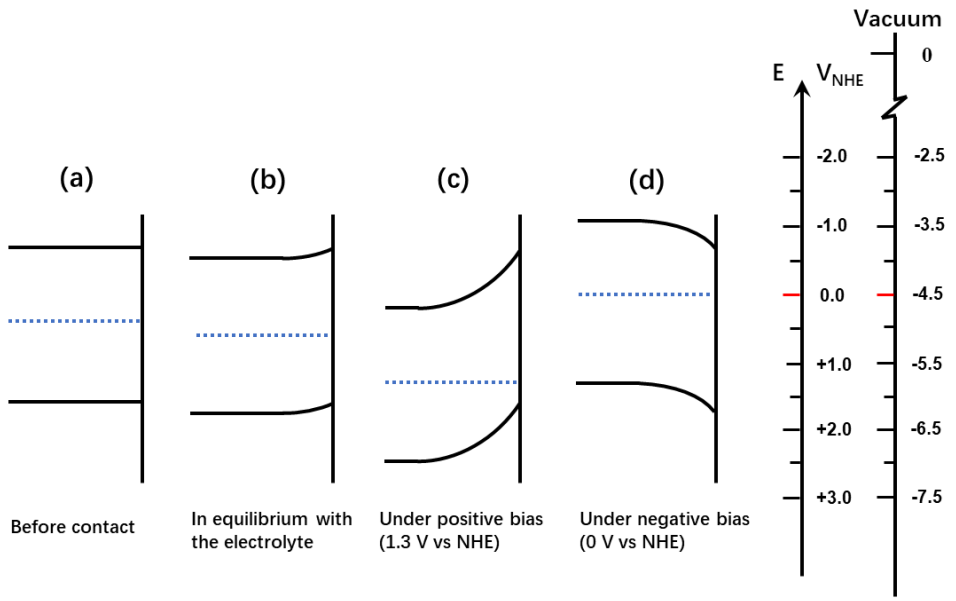


**Figure 4.7 Schematic band diagrams of (a) a bare $BiFeO_3$ electrode (b) $BiFeO_3$ electrode in equilibrium with the electrolyte ($Na_2SO_4$ solution) (c) $BiFeO_3$ electrode under bias positive of the flat band potential (1.3 $V_{NHE}$) (d) $BiFeO_3$ electrode under bias negative of the flat band potential (0 $V_{NHE}$).**

The position of the Fermi level within the bandgap is determined by the electron concentrations, which is a function of the donor and acceptor concentrations in extrinsic semiconductor[8]. For a typical n-type semiconductor, the donor concentration is dominating and the position of Fermi level is close to the CBM, and the difference between them is about ~ 0.1 to 0.2 eV[8,125]. However, in compensated semiconductors such as $BiFeO_3$, the Fermi level position can be varied depending on the doping concentration of the cation vacancy (Bi and Fe vacancy) as acceptor and the oxygen vacancy as donor. $BiFeO_3$ is well known for its complexity arising from the ease defects

formation. P-type conductivity is usually observed under normal (oxygen-rich) processing conditions with Bi and Fe vacancies dominating, and n-type conductivity is usually observed under oxygen-poor processing conditions with oxygen vacancy dominating[92,131,132]. In our study, the $BiFeO_3$ film is slightly p-doped, with the Fermi level position slightly positive than the middle of band gap. This allows the upward and downward band bending at the electrode/electrolyte interface when it works as the photoelectrode and presenting switchable photocurrents at different applied bias.

## 4.4. **Summary**

In this chapter, a switchable photocurrent in $BiFeO_3$ photoelectrode was reported for the first time. The origin of the ambipolar behavior has been investigated by electrochemical method and explained from the perspective of energy band diagrams. APXPS characterisation has been carried out to obtain the VBM and Fermi level position of the $BiFeO_3$ film. Measurement of the VBM and Fermi level position gives out direct information of the $BiFeO_3$ band structure and it agrees well with the PEC results.

The specific bandgap structure of the $BiFeO_3$ photoelectrode provides it with the advantage of generating either anodic or cathodic photocurrents as a function of applied bias. Since the CBM and VBM of $BiFeO_3$ straddle the water redox potential, it is possible

to promote either the hydrogen or the oxygen evolution at one electrode just by tuning the applied potentials and thus allow for selective PEC oxidation or reduction, arousing particular interest for its future application in solar energy conversion. Furthermore, this finding can be adapted to understand and predict other semiconductor photoelectrodes with analogous ambipolar behavior. It also gives a hint of the way to prepare switchable photoelectrode materials in the future, especially for the compensated semiconductors.

# Chapter 5 Photoanode Performance of $Bi_2Fe_4O_9$ Thin Films with Visible Light Activity

## 5.1. Introduction

Compounds containing $Bi^{3+}$ have been found to be narrow-band-gap semiconductors. It has been suggested that $Bi^{3+}$ containing compounds can show high PEC performance under visible light due to the strong hybridization between O-2p and Bi-6s orbitals[133,134]. It has also been found that hybridized energy bands can increase the separation of photoexcited holes and electrons and further improve the PEC conversion efficiency[135]. Therefore, in addition to $BiVO_4$, other Bi-based compounds, $CuBi_2O_4$[136], $BiFeO_3$[81], and $Bi_2WO_6$[137] have attracted interest as possible visible light photocatalysts.

The Bi-based compounds, $Bi_2Fe_4O_9$ has attracted attention for a number of applications such as semiconductor gas sensors and catalyst for ammonia oxidation to NO[95,96,138]. Like many other Bi-based compounds, $Bi_2Fe_4O_9$ exhibits a narrow indirect band gap with reported values ranging from ca. 1.9 to ca. 2.1 eV[99,139]. Nanoparticles of $Bi_2Fe_4O_9$ have been reported to be highly visible-light active photocatalysts with a near-infrared absorption. These particles show good photocatalytic activity for organic contaminants degradation[100,140,141]. However, to date there has been no reported studies on the use of

$Bi_2Fe_4O_9$ thin films as photoelectrodes for PEC applications.

In this chapter, $Bi_2Fe_4O_9$ thin films were prepared using CSD method. The morphology, structure, elemental composition and chemical states and optical properties have been characterised. The photoelectrochemical performance of the as-produced thin films has been investigated through the PEC test system.

## 5.2. **Characterisation of $Bi_2Fe_4O_9$ Thin Film**

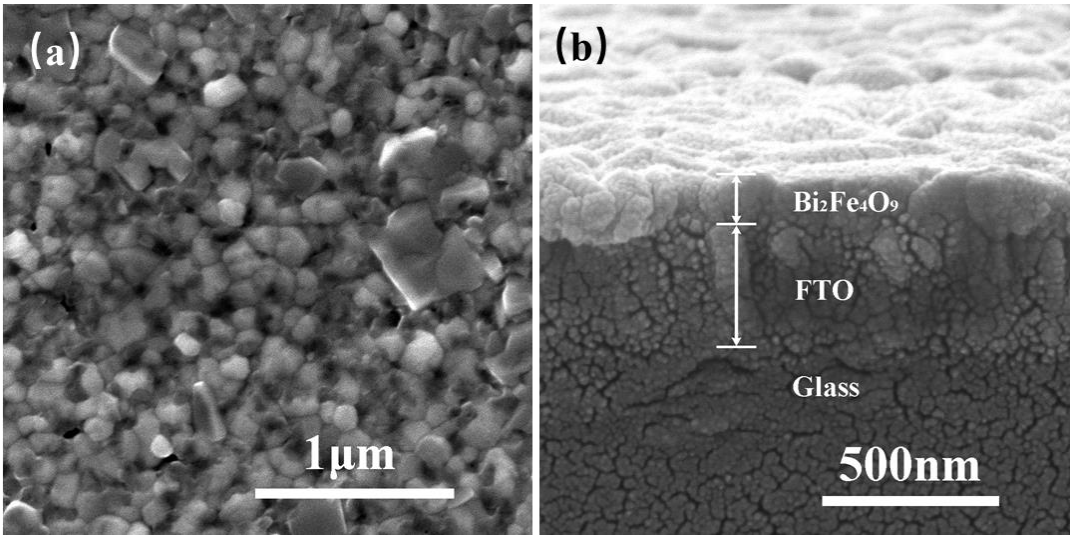


**Figure 5.1 SEM image of the $Bi_2Fe_4O_9$ film (a) top view (b) cross section view.**

The morphology and structure of the $Bi_2Fe_4O_9$ film was characterised using SEM and X-ray diffraction. Figure 5.1a shows a typical surface SEM image of $Bi_2Fe_4O_9$ exhibiting limited surface texture and a grain structure from 50 – 200 nm. Figure 5.1b shows a

cross-section of a typical film indicating that the film is *ca.* 150 nm thick and consists of a number of small crystallites. X- ray diffraction pattern of the as-produced film (Figure 5.2) confirms that a phase pure sample of $Bi_2Fe_4O_9$ has been produced with an orthorhombic structure (ICDD 74-1098; space group: *Pbam*) and lattice constants of a = 7.950 Å, b = 8.428 Å, and c = 6.005 Å. All additional peaks in the diffraction pattern can be attributed to the substrate.

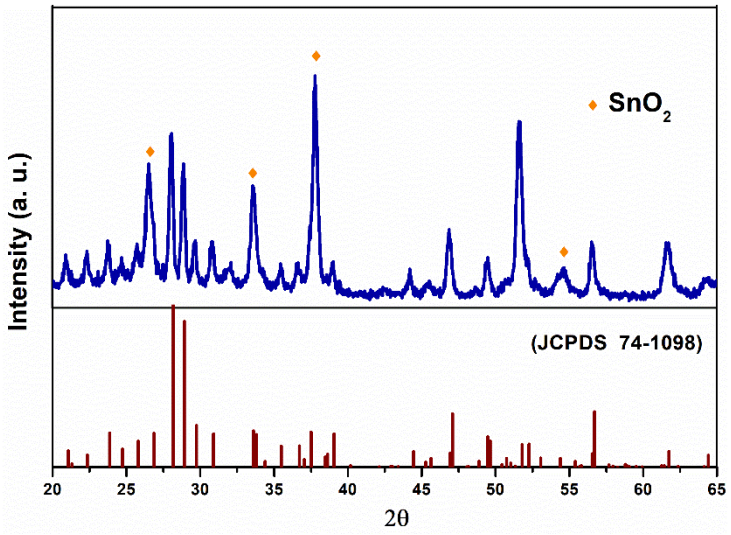


**Figure 5.2 XRD pattern of the $Bi_2Fe_4O_9$ film.**

XPS was undertaken to characterise the elemental composition and chemical states of the $Bi_2Fe_4O_9$ film. The XPS spectra of a typical sample is shown in Figure 5.3, with the XPS full survey spectrum shown in Figure 5.3a. A detailed view of the bismuth 4f spectrum is given in Figure 5.3b and shows two distinct peaks: the Bi $4f_{7/2}$ peak at 158.9 eV and the

Bi $4f_{5/2}$ peak at 164.2 eV. Both of the two peaks and their positions are characteristic of the presence of bismuth in the + 3 oxidation state, as expected for $Bi_2Fe_4O_9$.

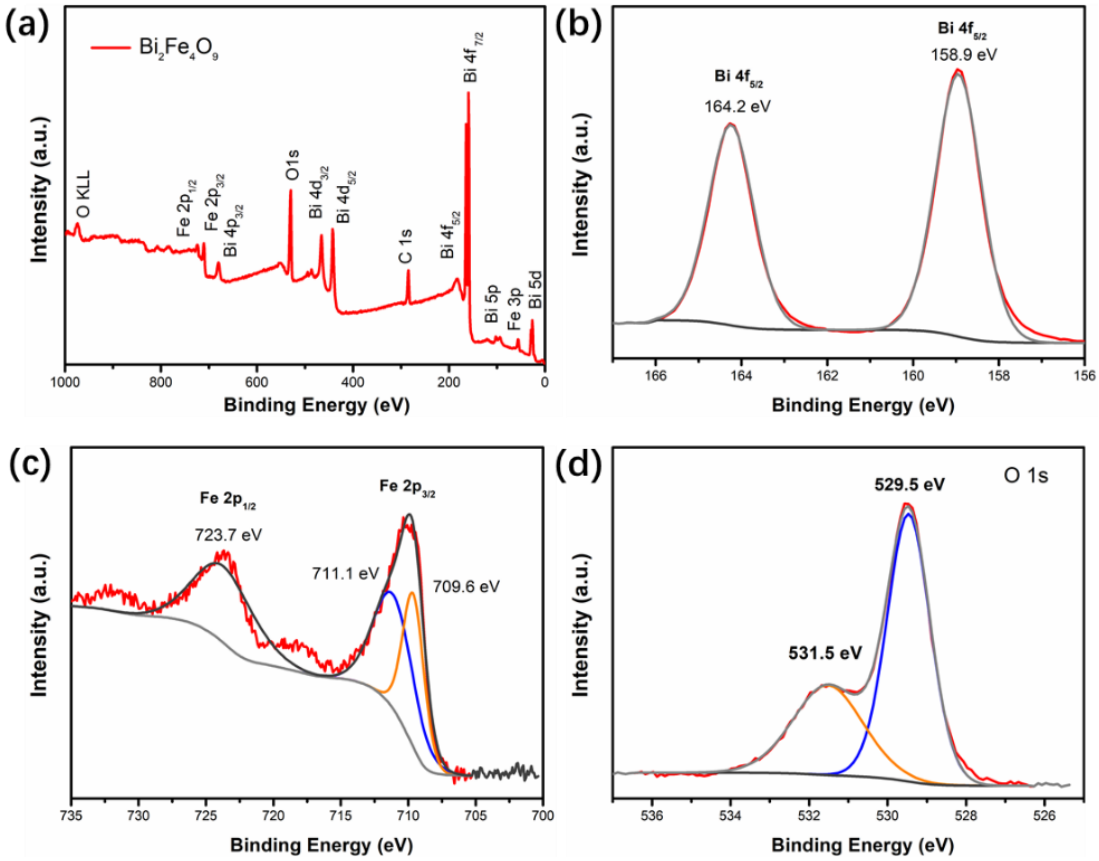


**Figure 5.3 (a) Survey spectrum, (b) Bi 4f, (c) Fe 2p and (d) O 1s XPS spectra of $Bi_2Fe_4O_9$ film.**

The Fe 2p core level, shown in Figure 5.3c, consists of two peaks located at 723.7 eV (Fe $2p_{1/2}$) and 710 eV (Fe $2p_{3/2}$). The Fe $2p_{3/2}$ peak was deconvoluted into two peaks located at 711.1 eV and 709.6 eV, corresponding to $Fe^{3+}$ and $Fe^{2+}$, respectively. The formation of $Fe^{2+}$ is attributed to the presence of oxygen vacancies commonly occurring in the deposition processes of perovskite thin films[142,143], which is further confirmed in

the O 1s spectrum (Figure 5.3d): the deconvolution of the O1s line results in peaks at 529.5 eV and 531.5 eV. The peak at 529.8 eV comes from the M-O-M bonds and that at 531.5 eV is due to a high number of defect sites with a low oxygen coordination, i.e. due to the presence of oxygen vacancies in accordance with the presence of $Fe^{2+}$.

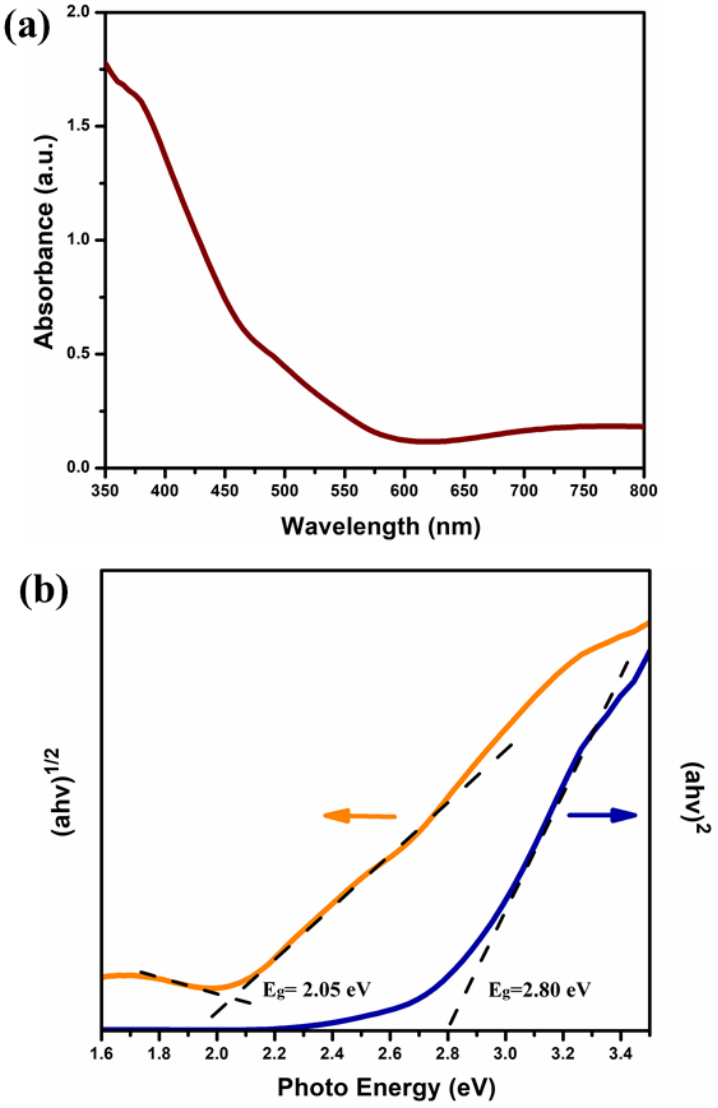


**Figure 5.4 UV-vis absorbance spectra and derived Tauc plots corresponding to the allowed direct (left insert) or allowed indirect (right insert) band gap.**

The optical absorption of the $Bi_2Fe_4O_9$ films was characterised using UV-vis spectroscopy. As shown in Figure 5.4a, the sample demonstrates light absorption over a wide range of frequencies ranging from the UV into the visible, consistent with the reported band gap of around 2 eV. It has been reported in previous studies that the $Bi_2Fe_4O_9$ nanoparticle samples had near-infrared light absorption, which was ascribed to the splitting of Fe 3d transitions[140,141]. For the $Bi_2Fe_4O_9$ thin film samples, a broad, shallow absorption peak can be observed between 650 nm to 800 nm, and a distinct absorption edge starts from ~ 600 nm and increases with decreasing wavelength. The good visible light absorption of the material indicates the possibility of photoactivity under visible-light illumination.

The linear regions in the derived Tauc plots (Figure 5.4b) indicate indirect and direct band gaps of 2.1 and 2.8 eV. The band gap associated with the indirect transition is close to ideal for solar water splitting[144], giving an indication that the material will be able to drive photochemical processes under visible light. However, the indirect transition means that there will be limited light absorption across the thin sample and gives some clues as to why nanoparticles have been of interest to date: the absorption cross section and scattering associated with nanoparticles can add to the effective pathlength and increase absorption. However, the presence of a direct transition at an only slightly higher energy of 2.8 eV means that there is still strong absorption within the visible region, as seen in the absorption spectrum (Figure 5.4a).

In order to understand the variety of photochemistry that can be driven on the surface of a photocatalyst, the band structure of the system must be understood. In order to estimate the relative band positions of the $Bi_2Fe_4O_9$ films, the optical band gap and flat band potential are required.

In Figure 5.5a, the extrapolation of the Mott-Schottky plot to the *x* intercept gives a flat band potential for $Bi_2Fe_4O_9$ of – 0.1 V (vs Ag/AgCl) or 0.1 V (vs NHE). The flat band potential for an n-type semiconductor approximates to the Fermi level ($E_F$) position[7,8]. Depending on the structure of the defects and contribution to $E_F$ there can be an energy difference from 0.2 eV (typically associated with oxygen vacancies) to a negligible gap (< 0.1 eV) between flat band potential and the conduction band for an n-type semiconductor[8]. It is therefore able to estimate the conduction band position of $Bi_2Fe_4O_9$. Based on this value and the measured indirect band gap of 2.1 eV, a band diagram was constructed, as shown in Figure 5.5b, indicating $Bi_2Fe_4O_9$ has significant overpotential for photocatalytic water oxidation.

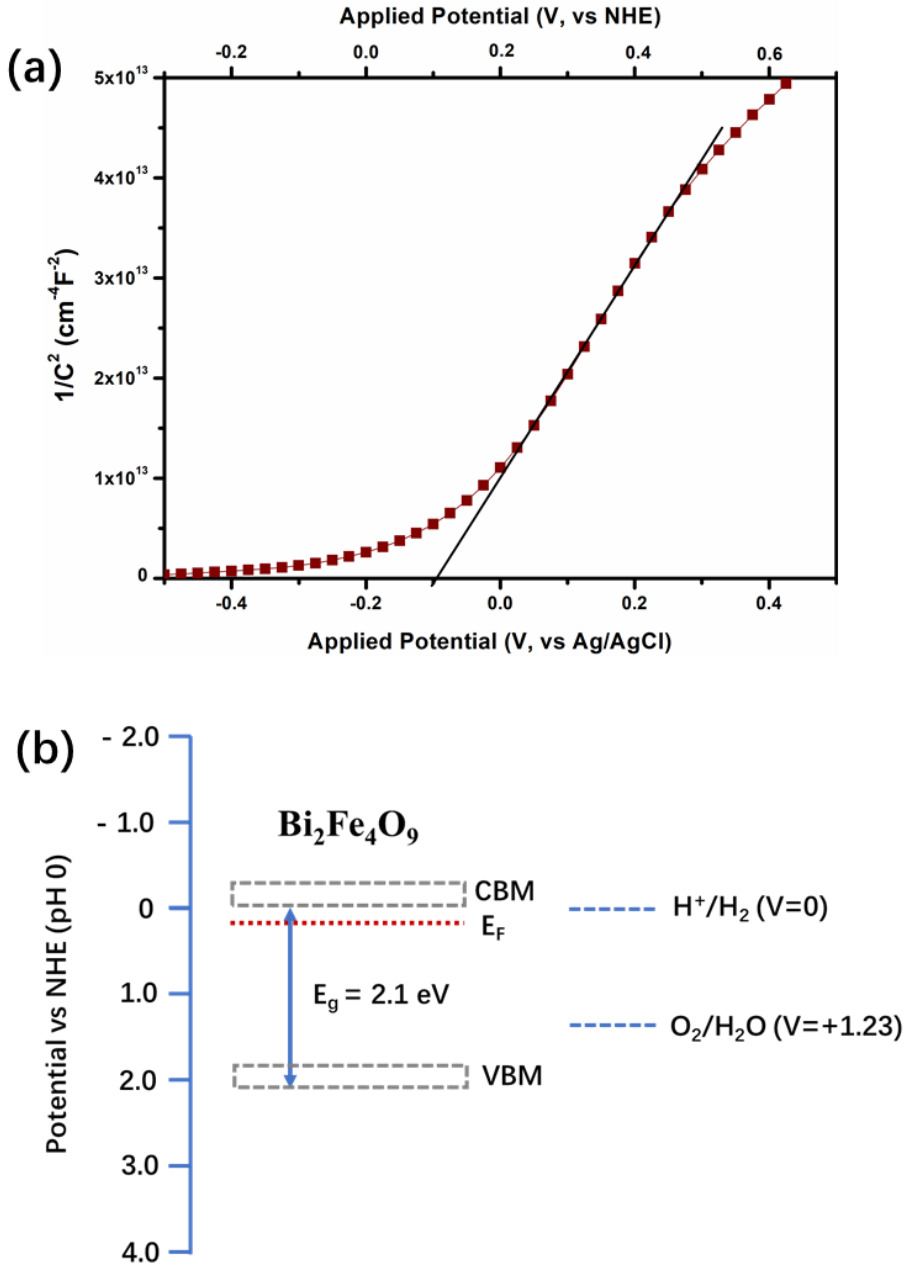


**Figure 5.5 (a) Mott-Schottky plot for $Bi_2Fe_4O_9$ electrode measured in the dark (b) schematic illumination of the estimated location of the conduction and valence bands in $Bi_2Fe_4O_9$ with respect to the redox potentials of water splitting.**

## 5.3. **Photoelectrochemical Measurements**

The photoanodic activity of $Bi_2Fe_4O_9$ films was investigated using a standard three electrode PEC cell. Figure 5.6 shows the photocurrent-voltage (I-V) curves of a $Bi_2Fe_4O_9$ photoelectrode illuminated using full AM1.5G and visible light only ($\lambda > 420$ nm) irradiation. The data shows a steady increase in photocurrents with increasing applied bias and the photocurrent at 1.23 V vs NHE reached 0.1 mA/cm$^2$ under full light illumination. When other bismuth ferrite films are considered, such as $BiFeO_3$, the values of photocurrent for $Bi_2Fe_4O_9$ are considerably larger or comparable depending on the film manufacture process. For example, Yu *et al.*[145] produced $BiFeO_3$ films deposited by pulsed laser deposition (PLD) and obtained ~ 0.09 mA/cm$^2$ at 1.23 V vs NHE under 1 sun, which was higher than that reported by Quynh[146] who also prepared $BiFeO_3$ by PLD giving ~0.06 mA/cm$^2$ at 1.1 V vs NHE under 1 sun. A $BiFeO_3$ film deposited on epitaxial $SrRuO_3/SrTiO_3$ substrate by sputtering has been reported to have a much lower value of ~ 0.01 mA at 1 V vs NHE[81]. When the UV was filtered from the AM1.5G illumination, the photocurrent from $Bi_2Fe_4O_9$ for pure visible light reached 0.05 mA/cm$^2$ at 1.23 V vs NHE. This indicates that changing the composition of this compound slightly to $Bi_2Fe_4O_9$ offers large benefits for PEC water oxidation performance, particularly considering the low-cost deposition method. To confirm the visible-light performance of the $Bi_2Fe_4O_9$ thin films, photocurrent was measured with the UV portion filtered from the AM1.5G

illumination ($\lambda$ > 420 nm) and it reached 0.05 mA/cm$^2$ at 1.23 V vs NHE. This photocurrent demonstrates the potential for $Bi_2Fe_4O_9$ to be a visible light active catalyst.

It can be seen from Figure 5.6 that the onset potential of $Bi_2Fe_4O_9$ is around 0.6 V vs NHE, while the flat-band potential derived from the Mott-Schottky plot is 0.1 V vs NHE, indicating an over potential of around 0.5 V exists between the onset potential and flat-band potential. This is analogous to the situation of a-$Fe_2O_3$ and $BiFeO_3$ electrodes: it has been reported that large over-potentials exist between the flat band and the onset potential of $Fe_2O_3$ photoelectrode as well as that of $BiFeO_3$ resulting from a number of limiting factors such as surface states[147,148]. Besides the large over-potential, the chopped light chronoamperometry curves also showed obvious transient photocurrent peaks upon turning the light on and off. Such peaks are known to be associated with a variation in the rates of carrier extraction across the semiconductor interface[18,149]. In order to investigated this in more detail, a typical hole-scavenger, $H_2O_2$, was added into the electrolyte solution for further study.

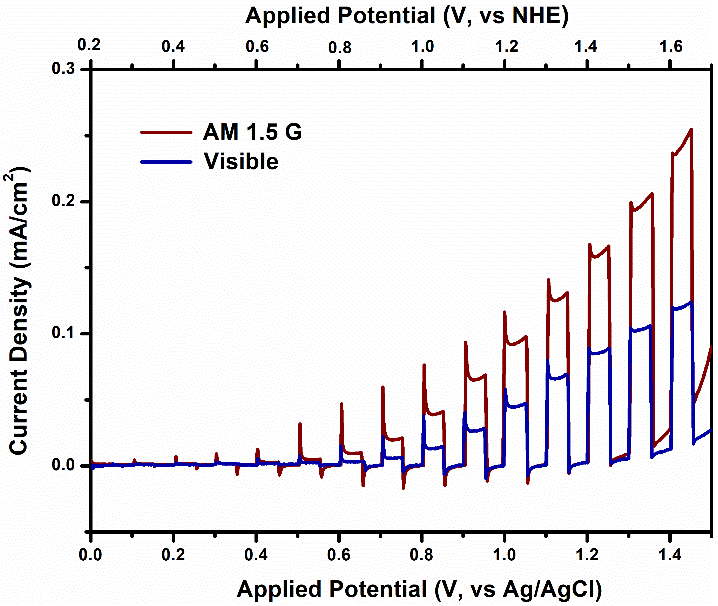


**Figure 5.6 I-V curve for $Bi_2Fe_4O_9$ under both 100 mW/cm$^2$ AM 1.5 G and visible light irradiation ($\lambda > 420$ nm) in $Na_2SO_4$ electrolyte (pH 6.5).**

Figure 5.7 shows a plot of current density vs applied potential under chopped illumination using two different electrolytes: 0.2 M $Na_2SO_4$ and 0.2 M $Na_2SO_4$-0.5 M $H_2O_2$. It can be seen that the addition of $H_2O_2$ to the electrolyte changes the onset potential of the photocurrent to 0.2 V vs NHE. This change in the onset potential aligns closely to the flat band potential that was measured using Mott Schottky of 0.1 V vs NHE. The transient photocurrents associated with the non-equilibrium extraction of holes and electrons have also been significantly reduced upon the addition of $H_2O_2$ and the photocurrent at 1.23 V vs NHE increased to 0.25 mA/cm$^2$. Transient photocurrents under chopped illumination have been observed in a range of photoanode materials such as $Fe_2O_3$[150] and $BiVO_4$[151].

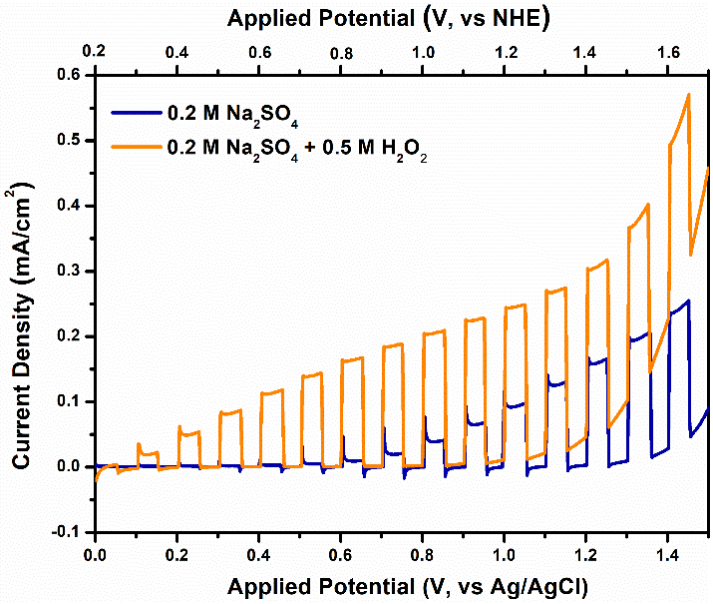


**Figure 5.7 Current density vs applied potential plots under chopped illumination (1 sun AM 1.5 G) for $Bi_2Fe_4O_9$ electrode without and with a hole scavenger ($H_2O_2$).**

This phenomenon was attributed to the hole accumulation at the photoanode/electrolyte interface[149]. As demonstrated by the experimental results, the producing of transient photocurrents can be suppressed either by applying sufficient potential or adding hole scavengers.

The inhibition of transient photocurrents or the reduced hole accumulation at large applied potentials can be understood from the view of energy band bending diagram. A schematic illustration is presented in Figure 5.8 for understanding the origin of the transient photocurrents and the migration pathways of photoexcited carriers under different applied potentials. There are mainly three pathways of the photoexcited

electrons and holes: ① extraction to redox reactions; ② bulk recombination and ③ back electron-hole recombination. Only the path way ① contributes to the effective photocurrents. Both of the bulk recombination and back electron-hole recombination limit the photocurrents generation. Under moderate applied potentials, for example, + 0.7 $V_{NHE}$ (Figure 5.8a), the band bending is small and there is a high chance for the photoexcited charge carriers to either recombine in the bulk (②) or on the surface (③). In this case the photocurrents produced has a small value (0.005 mA/cm$^2$ under full light irradiation) and the transient photocurrents are obvious. When the applied potential increased to a larger value, i.e. +1.4 $V_{NHE}$ (Figure 5.8b), the band bending increases and the depletion region will increase correspondingly. The charge carriers will get more chance to migrate to the depletion region and be separated more efficiently due to the increasing driving force arising from the increased band bending. The holes arrived on the electrode surface will be more energetically favorable for the water oxidation reaction. Accordingly, the back electron-hole recombination will be largely inhibited, resulting in an increased photocurrent (0.15 mA/cm$^2$ under full light irradiation).

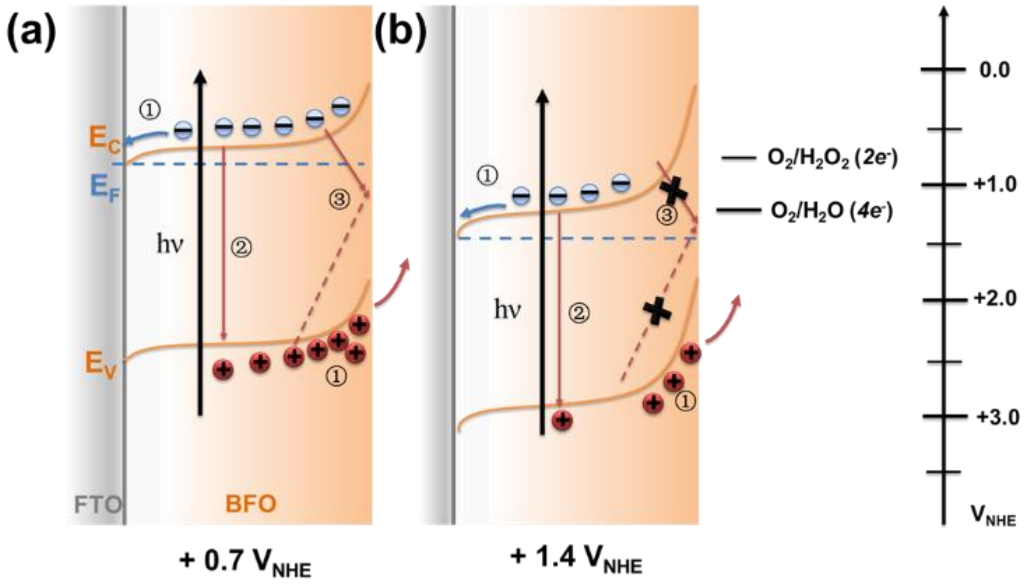


**Figure 5.8 A schematic illustration of the energy diagrams and processes involving the migration of the photogenerated charge carriers in the $Bi_2Fe_4O_9$ photoelectrode under different applied potentials. (a) +0.7 $V_{NHE}$ (b) +1.4 $V_{NHE}$**

The addition of a hole scavenger can speed the kinetics of water oxidation. It is well known that the 4-hole oxidation of water to molecular oxygen has a sluggish kinetics, which means that there is an excess generation of photoexcited holes over the rate of extraction to perform the electrochemical reaction[152]. As stated in section 4.3, $H_2O_2$ is an ideal hole scavenger since it has much higher rate constant for oxidation than water (10 to 100 times) and a relatively negative reduction potential than that of water[147]. The addition of $H_2O_2$ as a hole scavenger can promote the reaction of accumulated holes at the electrode/electrolyte interface and suppress back electron-hole recombination. The addition of a hole scavenger demonstrates that the photocurrents of $Bi_2Fe_4O_9$ electrode

can be further improved by eliminating the hole injection barrier at the electrode/electrolyte interface, for example by combination with co-catalysts or reduction in surface trap states.

A key consideration for the use of photocatalytic materials is the stability of the system under illumination. The stability of the $Bi_2Fe_4O_9$ electrode was tested by measuring the photocurrent over time (*I-t*), as shown in Figure 5.9. The I-t curve was obtained under full sunlight illumination in a 0.2 M $Na_2SO_4$ electrolyte. It can be seen from the I-t results that there is no loss of the photocurrents during the 3 hours test, indicating the good stability of $Bi_2Fe_4O_9$ films under illumination as a photoanode.

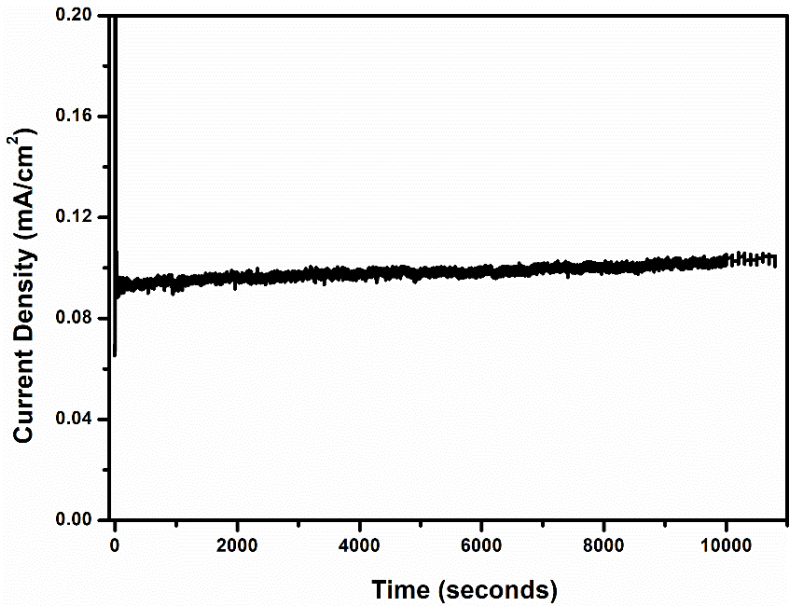


**Figure 5.9 Photocurrent density–time curves of $Bi_2Fe_4O_9$ electrode measured at an applied potential of 1 V (vs Ag/AgCl) for 3h in 0.2 M $Na_2SO_4$ solution under 1sun illumination.**

## 5.4. **Summary**

This chapter has outlined the development of $Bi_2Fe_4O_9$ as a novel photoanode for photoelectrochemical water oxidation. Phase-pure $Bi_2Fe_4O_9$ films have been synthesized via a simple CSD method using a stoichiometric Bi/Fe molar ratio of 0.5:1 for the precursor preparation. The $Bi_2Fe_4O_9$ photoanode exhibits an indirect bandgap of 2.1 eV and direct transition at 2.8 eV leading to a strong visible light response. The measured band positions indicate suitability for water oxidation.

PEC tests demonstrate high activity of the $Bi_2Fe_4O_9$ electrode under AM1.5G and visible light illumination. The photocurrent at 1.23 $V_{NHE}$ reached 0.1 mA/cm$^2$ under full light illumination and it reached 0.05 mA/cm$^2$ under visible light. The photocurrent values of $Bi_2Fe_4O_9$ are considerably higher or comparable compared to other bismuth ferrite films reported in literature. Though the photocurrent of $Bi_2Fe_4O_9$ is not comparable to $Fe_2O_3$, which is the representative photoanode material currently, considering it is a planar film with no nanostructuring, there's a high chance for the improvement of photocurrent by obtaining films of higher surface area and more light scattering centers.

By adding a hole scavenger, we have demonstrated that a hole injection barrier exists at the surface of the $Bi_2Fe_4O_9$ electrode. This indicates that the PEC performance of the

material can be further improved by methods such as modification of surface states to enhance carrier extraction. The $Bi_2Fe_4O_9$ combines strong light absorption, easy fabrication and good stability under illumination, making it a promising candidate for photoanodes in application of practical solar energy-driven PEC water splitting.

# Chapter 6 Effects of Ferroelectricity on Photocatalytic Activity of Nanoscale $Ba_xSr_{1-x}TiO_3$ Powders

## 6.1. Introduction

The effect of ferroelectricity on photocatalytic activity has been reported in several material systems such as $BaTiO_3$ and $BiFeO_3$, including that of particles and thin films. When considering the ferroelectric effect on the photocatalytic activity, there are two factors/contributions must not be overlooked. One is grain size effect, the other is domain wall contribution. As reviewed in chapter 2, the ferroelectric polarization can be suppressed in some degree when the material size reducing to nanoscale, making it difficult to characterise by common techniques such as XRD. Thus it is important to confirm the polar/non-polar structure of the ferroelectrics before further comparison of their photocatalytic activity. Besides, the domain wall contribution can be dominating in performance of ferroelectrics[42], which have not been taken into account in the previous studies of ferroelectric photocatalyst. Thus, it is of our interest to obtain ferroelectric materials of single-domain-single-grain structure to eliminate the contribution from domain walls and probe the effect of ferroelectric polarization on the photocatalytic activity in a simplest system.

# Chapter 6

In this chapter, nanoscale barium strontium titanate powders have been prepared to investigate the ferroelectric effect on photocatalytic activity in single-grain-single-domain structures. Samples of two compositions, $Ba_{0.8}Sr_{0.2}TiO_3$ ($T_c$ ~ 72 °C) and $Ba_{0.2}Sr_{0.8}TiO_3$ ($T_c$ ~ -148 °C) have been chosen as the target material. The polar, non-polar structures of the as-obtained samples have been studied by various methods and confirmed by Raman spectra. Photocatalytic activity of the two samples was evaluated by comparing the photodegradation rate of Rhodamine B (Rh B). The $Ba_{0.8}Sr_{0.2}TiO_3$ sample with polar structure showed enhanced degradation rate compared to $Ba_{0.2}Sr_{0.8}TiO_3$ with non-polar structure. By obtaining both of the nonpolar- and polar-structured $Ba_xSr_{1-x}TiO_3$ nanoscale powders, the effect of ferroelectricity on the photocatalytic activity can be ascertained directly, demonstrating the potential for ferroelectrics to increase the solar energy conversion efficiency.

## 6.2. **Characterisation of $Ba_xSr_{1-x}TiO_3$ Powders**

### 6.2.1. Structure, composition and optical properties

Phase compositions of the two samples were analyzed using XRD and shown in Figure 6.1. No obvious peak splitting was observed at the peak of $2\theta$ = 45 for the $Ba_{0.8}Sr_{0.2}TiO_3$ sample as expected for a ferroelectric material with tetragonal phase below its curie point.

The loss of ferroelectric feature in nanosized ferroelectric materials in the XRD patterns has been reported in a number of previous researches[44]. This is mainly attributed to the decreased spontaneous polarization in ultrafine ferroelectric particles, which can lead to a reduced c/a ratio and make it difficult to be distinguished in the XRD patterns. Thus, further confirmation of the polar/non-polar structure of the samples is needed.

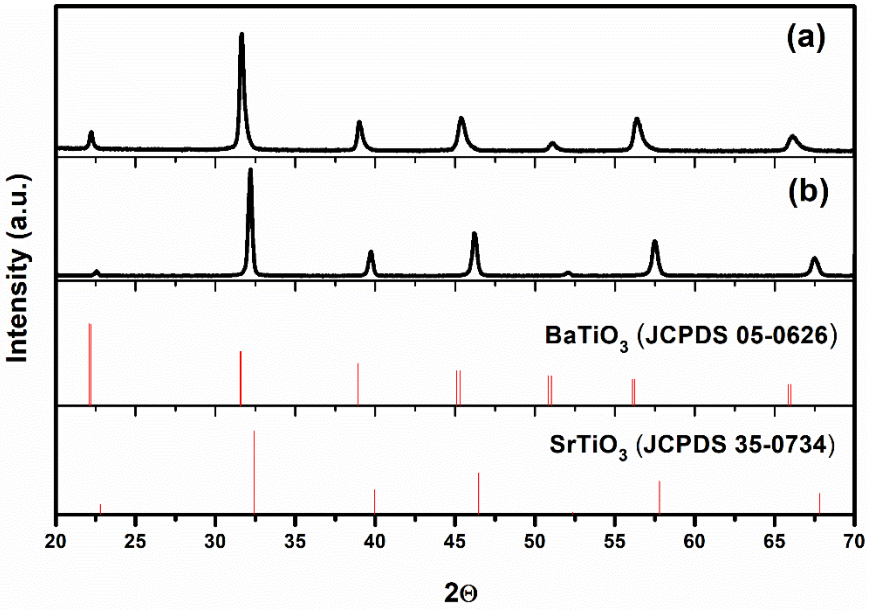


**Figure 6.1 XRD pattern of (a) $Ba_{0.8}Sr_{0.2}TiO_3$ (b) $Ba_{0.2}Sr_{0.8}TiO_3$**

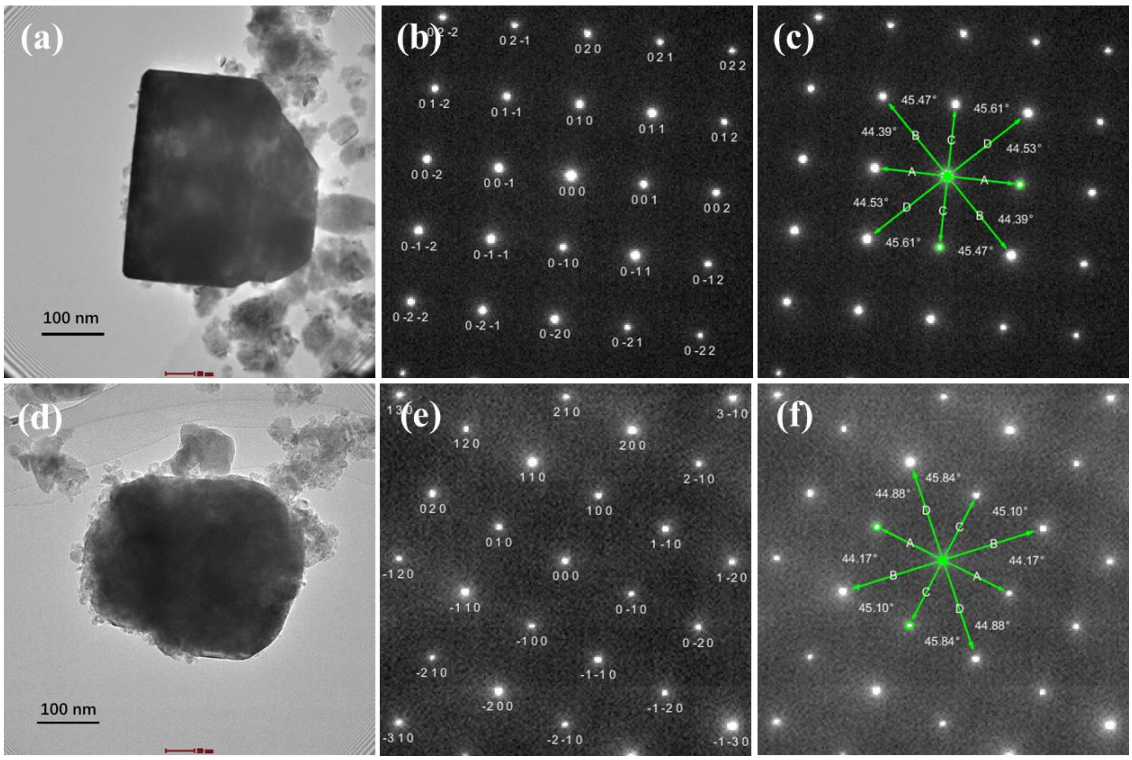


**Figure 6.2 TEM images and diffraction patterns of $Ba_{0.8}Sr_{0.2}TiO_3$ (a)(b)(c) and $Ba_{0.2}Sr_{0.8}TiO_3$ (d)(e)(f). (a)(d) bright-field TEM image; (b)(c) selected area electron diffraction pattern ([100] direction); (e)(f) selected area electron diffraction pattern ([001] direction).**

Microstructure of the two $Ba_xSr_{1-x}TiO_3$ samples were investigated by TEM (Figure 6.2). According to electron diffraction patterns (see Figure 6.2c and Figure 6.2f), both of the two samples are single-crystalline. Absence of domain wall features in the TEM image and superlattice diffraction spots in diffraction patterns suggests that they are both single domain structure[153]. It is noteworthy that the diffraction patterns also show a cubic structure for both samples, which is consistent with XRD results. Again, this is related to the size effect and the polar structure will need further confirmation.

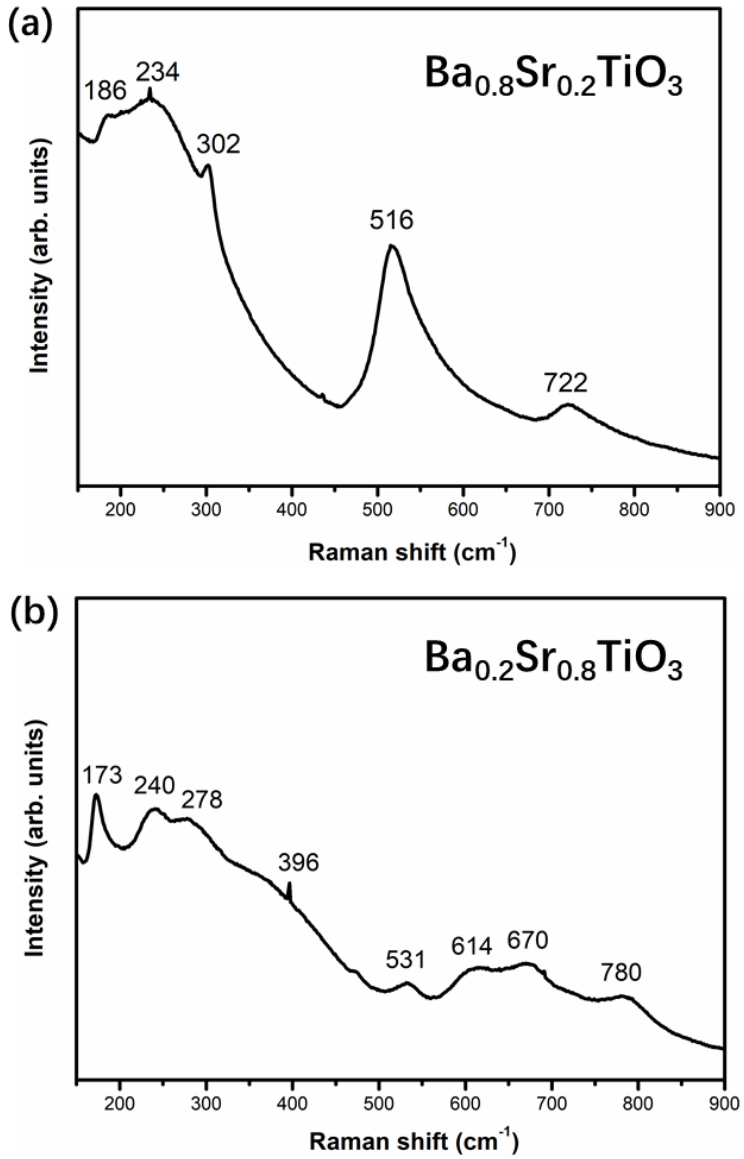


**Figure 6.3 Raman spectra at room temperature for (a) $Ba_{0.8}Sr_{0.2}TiO_3$ (b) $Ba_{0.2}Sr_{0.8}TiO_3$**

Raman spectroscopy is a useful tool for study of the lattice dynamics of the nanoscale ferroelectric systems, owing to its sensitivity to short-range distortions resulting from microstructural defects. Compared to XRD, it is more suitable to probe local structure and subtle symmetry changes[44]. Raman spectra of $Ba_{0.8}Sr_{0.2}TiO_3$ and $Ba_{0.2}Sr_{0.8}TiO_3$

collected at room temperature are shown in Figure 6.3a and Figure 6.3b. In the spectra of $Ba_{0.8}Sr_{0.2}TiO_3$, the two peaks at 302 $cm^{-1}$ and 722 $cm^{-1}$ are the characteristic peaks of the tetragonal phase, indicating the polar nature of $Ba_{0.8}Sr_{0.2}TiO_3$ powder. The peaks centered at 234 and 516 $cm^{-1}$ are attributed to disorder of titanium. Peak at 186 $cm^{-1}$ is resulted from impurity in the sample. In the spectra of $Ba_{0.2}Sr_{0.8}TiO_3$, both first- and second-order Raman scattering have been observed. Though for a ferroelectric material with perovskite structure, the Raman spectra obtained above $T_c$ should be dominated by second-order scattering which consists of a low-frequency band at 79 $cm^{-1}$ and two broad bands centered in the 200-400 $cm^{-1}$ and 600-800 $cm^{-1}$ regions, first order Raman peaks at ~ 173, 278, 531 and 780 $cm^{-1}$, which is expected for $Ba_{0.2}Sr_{0.8}TiO_3$ below $T_c$, are observed as well. This phenomenon is analogous to that reported for nanocrystalline $SrTiO_3$ particles[154] and is believed to resulting from the defect-induced polar microregions, especially for samples prepared by molten-salt method.

SEM images of the two $Ba_xSr_{1-x}TiO_3$ samples are shown in Figure 6.4. Table 6.1 lists the mean particle sizes and the BET surface areas of the two samples. It can be seen that particle size of the two samples has a close value, and so does the surface area. For a catalyst, particle size and surface area are important factors when evaluating the catalytic efficiency of a system. Thus here, the preparation of two $Ba_xSr_{1-x}TiO_3$ samples with close surface area and particle size allows for comparison of influence from other contributions

such as their polar/non-polar structure on the photocatalytic activity.

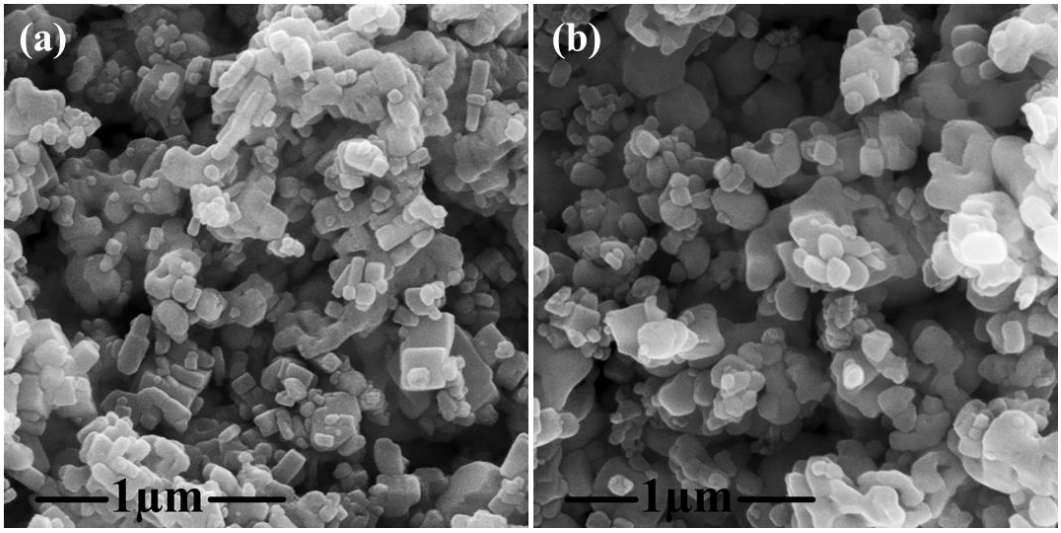


**Figure 6.4 SEM micrographs of (a) $Ba_{0.8}Sr_{0.2}TiO_3$ (b) $Ba_{0.2}Sr_{0.8}TiO_3$.**

**Table 6.1 Particle Size and Surface Area of $Ba_{0.8}Sr_{0.2}TiO_3$ and $Ba_{0.2}Sr_{0.8}TiO_3$**

| Sample | Average particle size (nm, SEM) | BET surface area ($m^2/g$) |
|---|---|---|
| $Ba_{0.8}Sr_{0.2}TiO_3$ | 70.8 | 7.3904 |
| $Ba_{0.2}Sr_{0.8}TiO_3$ | 65.2 | 7.9646 |

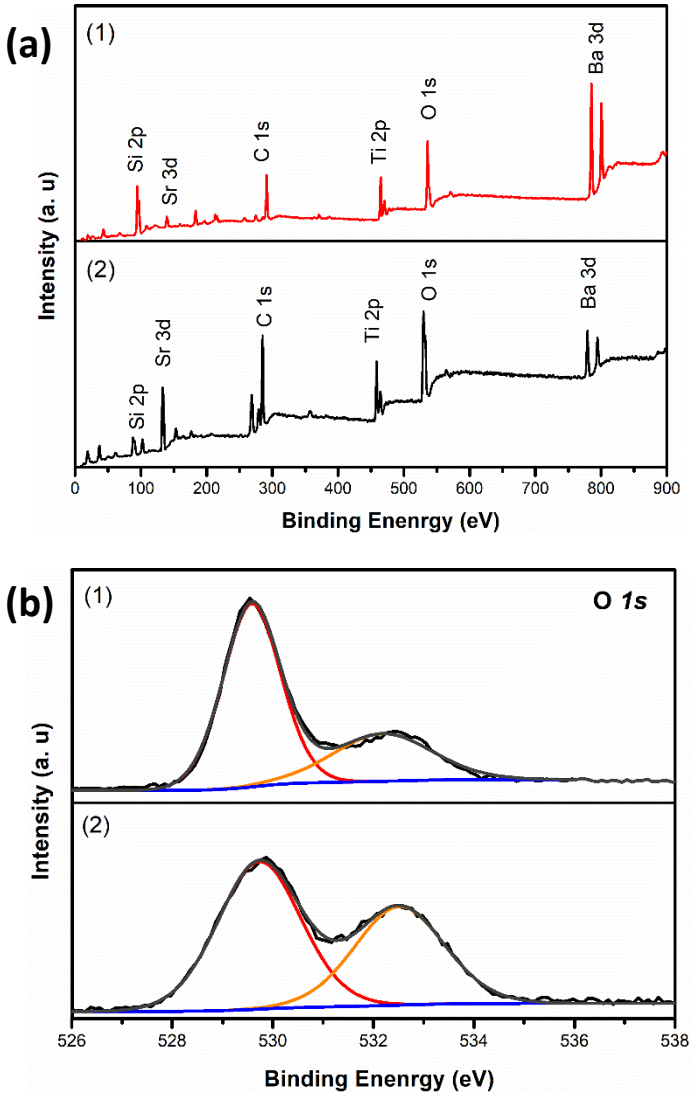


**Figure 6.5 XPS spectra of $Ba_xSr_{1-x}TiO_3$ (1) survey spectra (2) O 1s spectra**

**(a) $Ba_{0.8}Sr_{0.2}TiO_3$ (b) $Ba_{0.2}Sr_{0.8}TiO_3$.**

XPS was used to identify the composition of the as-synthesized $Ba_xSr_{1-x}TiO_3$ samples. Figure 6.5(1) gives a XPS survey spectrum of the $Ba_{0.8}Sr_{0.2}TiO_3$ (a) and $Ba_{0.2}Sr_{0.8}TiO_3$ (b) in the binding energy range of 0-900 eV. It can be seen that the $Ba_xSr_{1-x}TiO_3$ samples

contain only Ba, Sr, Ti, and O elements except for the C and Si signal, which is from the carbon adsorption from atmosphere and the siloxane tape used. Figure 6.5(2) shows the XPS spectrum of the two samples in the O 1s core level region. For $Ba_{0.8}Sr_{0.2}TiO_3$, two peaks at 529.58 eV and 532.18 eV are observed. And for $Ba_{0.2}Sr_{0.8}TiO_3$, the two peaks located at 529.73 eV and 532.52 eV. For both samples, the O 1s binding energy of around 529 eV is assigned to lattice oxygen, while the binding energy of around 532 eV is ascribed to oxygen vacancy. The existence of oxygen vacancies in perovskite materials is common, especially in those prepared by molten-salt method. This is due to the reducing atmosphere arising from the decomposition of oxalate, which can yield CO and $CO_2$[155].

UV-vis diffuse reflectance spectra of the two samples are shown in Figure 6.6a. Their band gaps were derived from the Tauc plot. As shown in Figure 6.6, the band gaps of $Ba_{0.8}Sr_{0.2}TiO_3$ and $Ba_{0.2}Sr_{0.8}TiO_3$ are both estimated to be 3.24 eV. The UV-vis data demonstrated that the two $Ba_xSr_{1-x}TiO_3$ samples have very close light absorption intensity and thus almost the same band-gap value. This allows the comparison of their photoactivity based on the same light absorption ability.

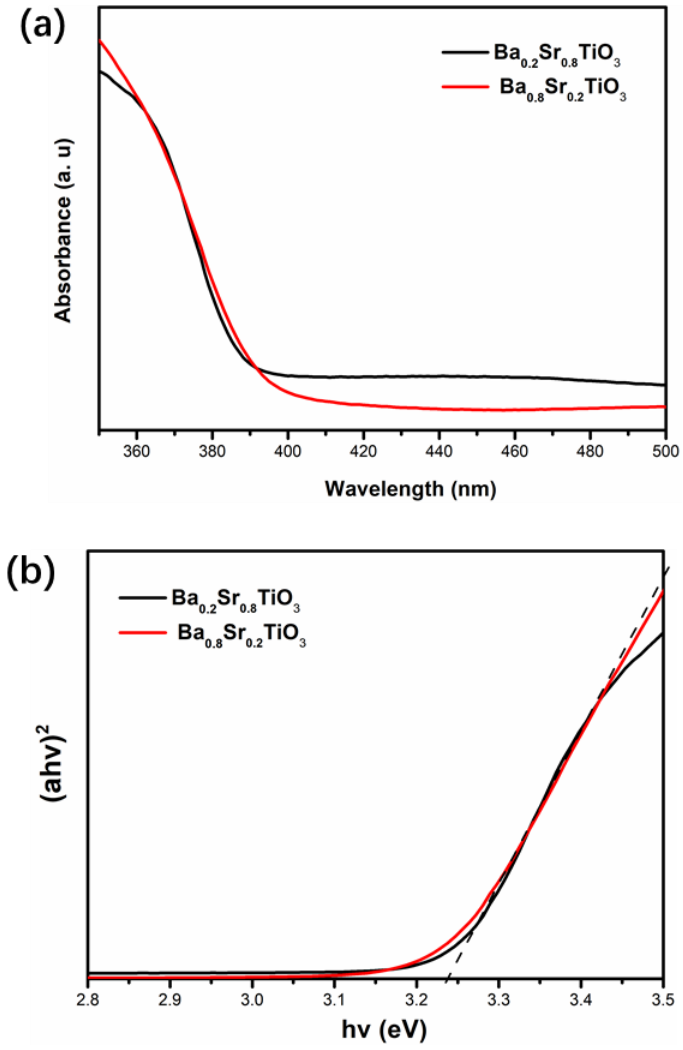


**Figure 6.6 UV-vis absorption spectrum and the derived Tauc plots of (a) $Ba_{0.8}Sr_{0.2}TiO_3$ and (b) $Ba_{0.2}Sr_{0.8}TiO_3$.**

### 6.2.2. Characterisation of the polar structure dependence of $Ba_{0.8}Sr_{0.2}TiO_3$ powders on grain size and temperature

As reviewed in section 2.2.4, when a ferroelectric material such as $BaTiO_3$ is cooled down through the Curie temperature, it will transform from cubic to tetragonal structure. The

strain and stress produced in this transformation can be released by the formation of ferroelectric domains, including the 180°and non-180° domains. The non-180° domains are usually primarily formed since it can minimize both of the elastic and electrostatic energy. It was demonstrated by Arlt *et al.* that the width of 90° domain in $BaTiO_3$ ceramics is proportional to the square root of the grain size[49]. Thus, the domain size decreases with decreasing grain size. When the grain size reduced down to a sufficiently small size, single domain will be more energetically favored than multi-domain structure. The grain size below which the single domain structure appeared was reported to be around 400 nm for $BaTiO_3$ ceramic by Zhao *et al.*[45]. It is of our interest to investigate the grain size at which multidomain to single domain transformation happens in $Ba_{0.8}Sr_{0.2}TiO_3$ samples, since we want to assess the photocatalytic activity based on a single domain structure.

To carry out the study of the dependence of polar structure on grain size, $Ba_{0.8}Sr_{0.2}TiO_3$ powders of different grain sizes were obtained by post-annealing the $Ba_{0.8}Sr_{0.2}TiO_3$ powders (possessed at 750 ℃) in different temperatures. The $Ba_{0.8}Sr_{0.2}TiO_3$ samples were post-annealed at 950 ℃, 1200 ℃ and 1350 ℃ for 10 hours, respectively. SEM graphs of the as-obtained samples are shown in Figure 6.7. It can be seen from the figures that the $Ba_{0.8}Sr_{0.2}TiO_3$ grain sizes increase dramatically with annealing temperature ranging from 750 ℃ to 1350 ℃. Though large grains with a sub-micro/micro size can be observed in all four samples, it is obvious that ultrafine grains with size smaller than

100 nm are dominating in the 750 ℃ sample and larger grains subsequently become the majority with increasing temperature, with micro-grains obtained in the 1350 ℃ sample.

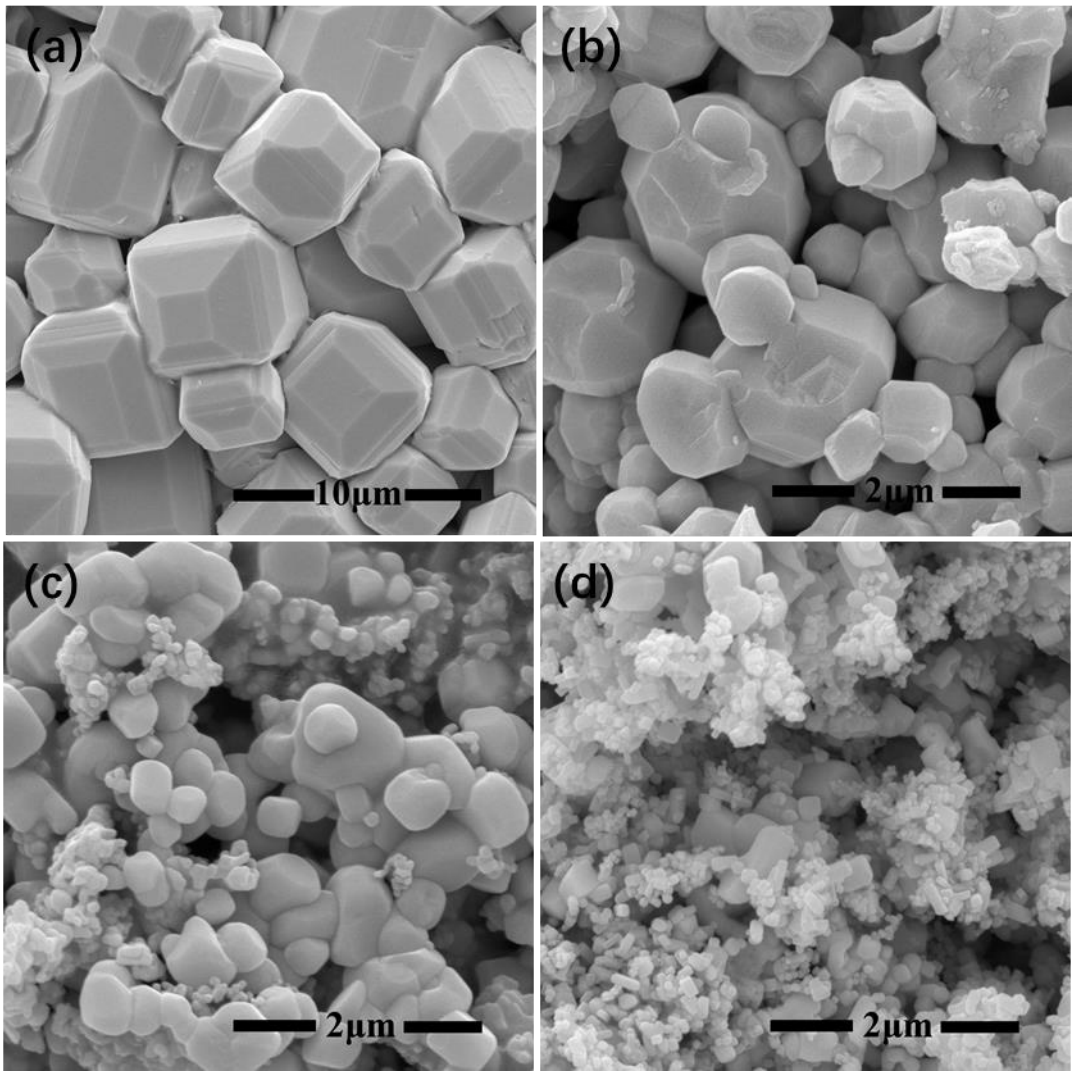


**Figure 6.7 SEM images of $Ba_{0.8}Sr_{0.2}TiO_3$ crystals processed at:**

**(a) 1350 ℃ (b) 1200 ℃ (c) 950 ℃ (d) 750 ℃.**

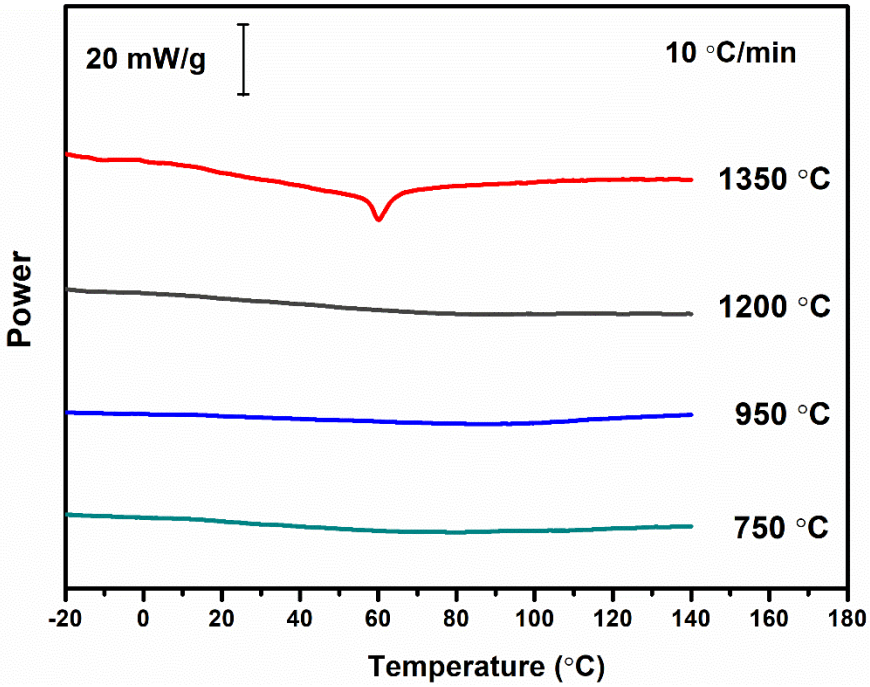


**Figure 6.8 DSC data for $Ba_{0.8}Sr_{0.2}TiO_3$ samples processed with increasing temperature.**

DSC measurement was done to check the dependence of phase transition thermal characteristics of the $Ba_{0.8}Sr_{0.2}TiO_3$ samples processed at different temperatures. Figure 6.8 gives DSC data for $Ba_{0.8}Sr_{0.2}TiO_3$ samples. It can be seen that the endothermic feature near 60 ℃ which is attributed to the tetragonal-cubic transformation is only observed in the sample post-annealed at 1350 ℃. With decreased post-annealing temperatures, the endothermic peak disappeared, this has been suggested to be the multi- to single- domain transformation characteristic, as reported in the study of M. H. Frey *et al.*[44] In their study, $BaTiO_3$ particles of different grain sizes exhibited multi- to single- domain transformation at the size of ~ 100 nm, demonstrated by the hot-stage TEM since the domain twining

disappeared when the particle size decreased to ~ 100 nm. In the meantime, the DSC results showed a broadened and shifted thermal peak associated with the cubic-tetragonal phase transformation, in consistence with the TEM results. Thus, it can be suggested that the particle size at which the DSC phase transition peak broadened or even disappeared is the size where multi- to single- domain transformation happens. From Figure 6.8 it can be seen that $Ba_{0.8}Sr_{0.2}TiO_3$ samples annealed at 1200 ℃ or lower temperatures showed no phase transition peak, suggesting a single domain structure formed from the annealing temperature of 1200 ℃. Thus it can be concluded the $Ba_{0.8}Sr_{0.2}TiO_3$ samples annealed at 750 ℃ has a single-domain-single-grain structure.

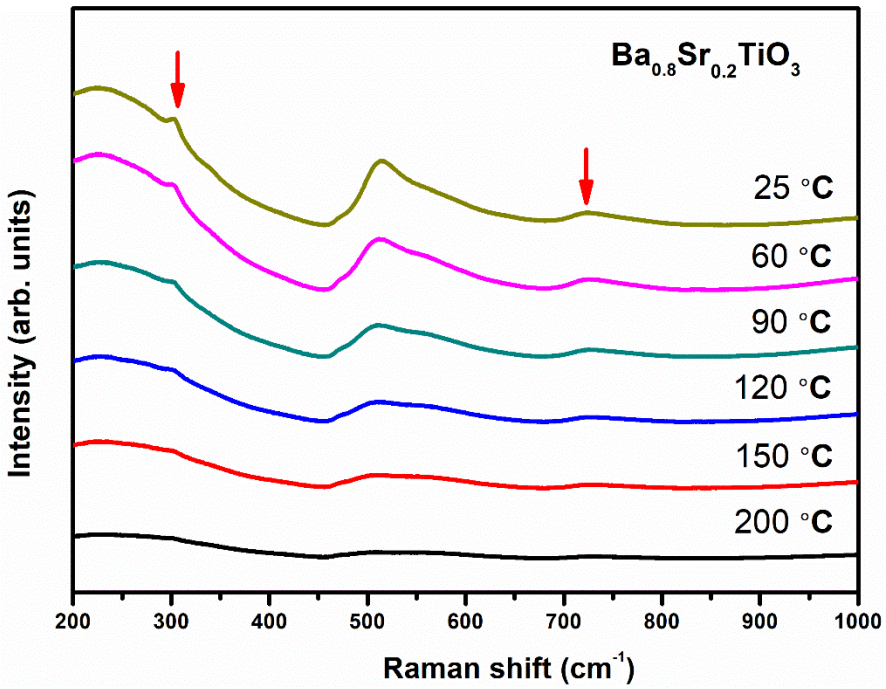


**Figure 6.9 Raman spectra for $Ba_{0.8}Sr_{0.2}TiO_3$ (processed at 750 ℃) at different temperatures.**

Raman spectra of the $Ba_{0.8}Sr_{0.2}TiO_3$ sample (processed at 750 ℃) collected over a range of temperatures between 25 and 200 ℃ have been obtained to reveal its phase transformation with temperature changing through the Curie point (shown in Figure 6.9). With increasing temperature, the two peaks (at 302 and 722 $cm^{-1}$) exhibit larger linewidths, indicating that the tetragonality is accompanied by a decreased structural coherence[53]. And the two peaks gradually vanish when the temperature increase from 25 ℃ to 90 ℃, demonstrating a tetragonal to cubic phase transition, which in turn, demonstrating that the $Ba_{0.8}Sr_{0.2}TiO_3$ specimen has a tetragonal/polar structure at room temperature.

## 6.3. **Photocatalytic Activity Assessment**

The photocatalytic activities of the two $Ba_xSr_{1-x}TiO_3$ photocatalysts (750 ℃ processed) are assessed by photodegradation of a target dye molecule – Rhodamine B under simulated solar light. The two samples were dispersed in Rh B and the mixtures were stirred under dark for 30 minutes to achieve the equilibrium between adsorption and desorption of the dye molecules on the photocatalyst surface. The degradation procedure then started by placing the mixture under the simulated solar light. It can be observed that the dye colour faded with time going on, indicating the decreasing concentration of the dye solution. Change of the dye solution concentration can be characterized by the UV vis measurement, by comparing the absorption intensity of the dye solution obtained in

different degradation stages.

Figure 6.10a and Figure 6.10b give the UV-vis absorption spectra of Rh B dye solutions degraded for different time using $Ba_{0.8}Sr_{0.2}TiO_3$ and $Ba_{0.2}Sr_{0.8}TiO_3$ as the photocatalysts. It can be seen that maximum absorption peak for Rh B was located at 554 nm and the light absorption intensity decreased with the irradiation time. The absorbance at zero time relates to the initial concentration of the Rh B dye and its intensity at $\lambda_{max}$ (554 nm) was recorded as $C_0$. The concentrations of other samples, taken as $C_i$, are determined from the absorption measurement at 540 nm as well.

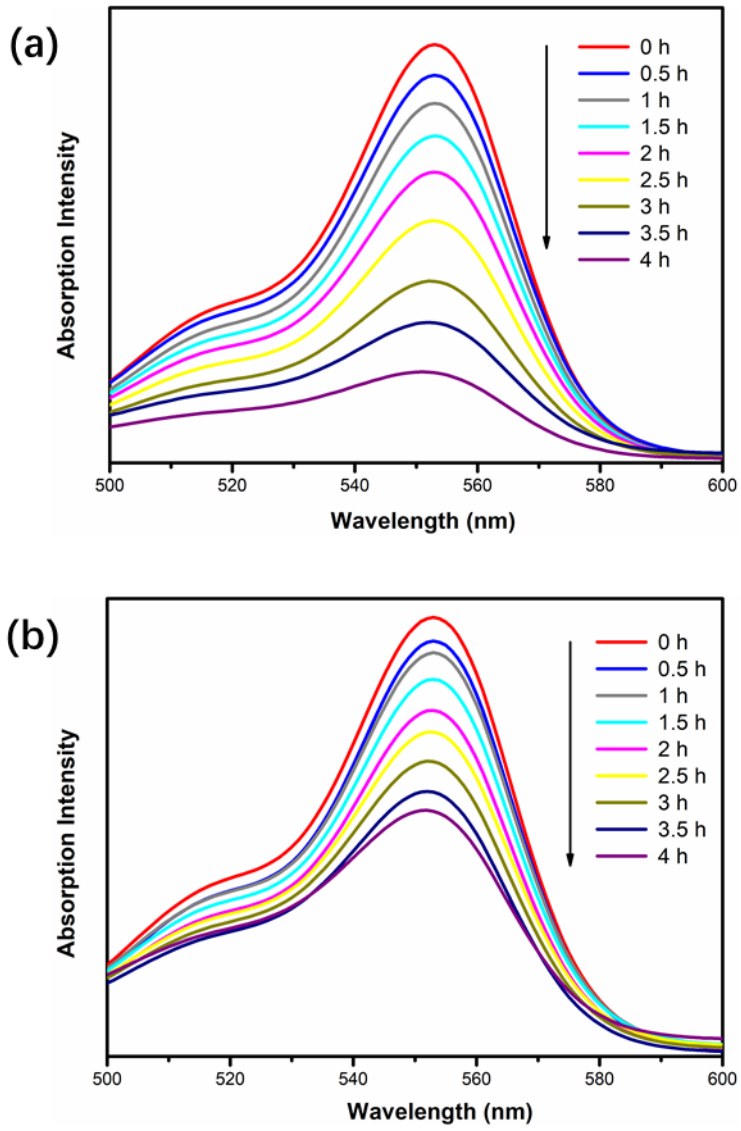


**Figure 6.10 UV-vis absorption spectra of Rh B dye solutions collected in different degradation stages by use of $Ba_{0.8}Sr_{0.2}TiO_3$ (a) and $Ba_{0.2}Sr_{0.8}TiO_3$ (b).**

The photodegradation intensity *X* at different stages can be obtained following the equation below:

$$X(\%) = (1\text{-}C_i/C_0) * 100 \qquad \text{Eqn (6.1)}$$

The photodegradation curves of Rh B of the two $Ba_xSr_{1-x}TiO_3$ samples are shown in Figure 6.11. It can be seen that $Ba_{0.8}Sr_{0.2}TiO_3$ showed higher rate in Rh B degradation.

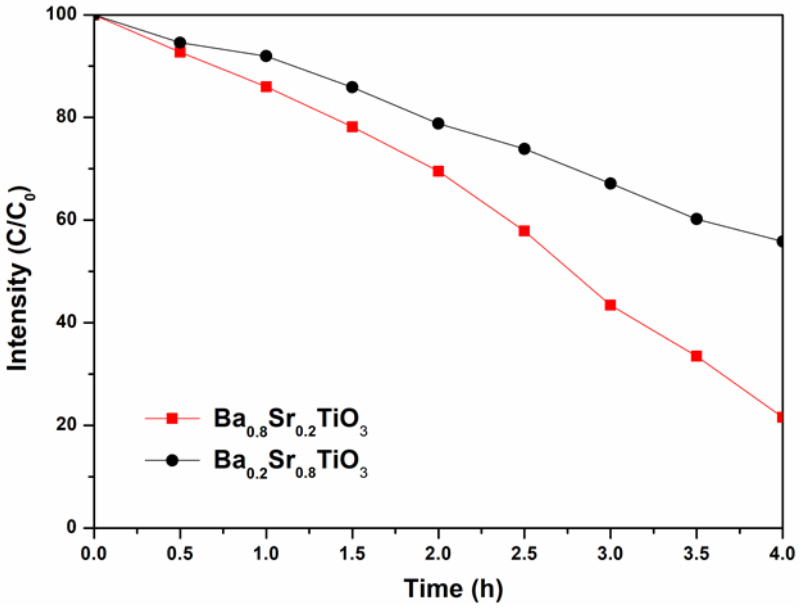


**Figure 6.11 Comparison of degradation profiles of Rh B with the two catalysts under solar simulator.**

A Langmuir-Hinshelwood model is usually used to reveal the dye degradation kinetics, from which a simplified relationship between the dye concentrations and the reaction rate $k$ can be obtained[156]:

$$\ln\left(\frac{C_0}{C}\right) = kt \qquad \text{Eqn (6.2)}$$

The derived $k$ of the two degradation process is shown in Table 6.2.

**Table 6.2 Photodegradation rate *k* of the two samples**

| Photocatalyst | k ($min^{-1}$) |
|---|---|
| $Ba_{0.8}Sr_{0.2}TiO_3$ | 0.1794 |
| $Ba_{0.2}Sr_{0.8}TiO_3$, | 0.1147 |

By comparing the photodegradation rate *k* in Table 6.2, it can be seen that $Ba_{0.8}Sr_{0.2}TiO_3$ powders with polar structure has larger reaction rate than that of non-polar $Ba_{0.2}Sr_{0.8}TiO_3$. In our previous characterizations, we have evaluated other possible factors that can affect the photocatalytic performance of the two samples, such as the morphology, surface area and band gap. The two $Ba_xSr_{1-x}TiO_3$ samples possess close surface area and the same band gap values. Besides, the two samples are single-grain single-domain structure, allowing for the comparison of ferroelectric effect without the contribution from domain walls. Thus, the enhanced photocatalytic performance of the $Ba_{0.8}Sr_{0.2}TiO_3$ can be attributed to the effect from its polar structure.

Effect of ferroelectricity on photocatalytic activity mainly comes from two contributions. The first is presence of the internal electric field within ferroelectric materials, which can aid the separation of photoexcited electrons and holes in the bulk of the photocatalyst and reduce their recombination chances. As reviewed in section 2.2.6, spontaneous polarization arises from the polar structure of the ferroelectric material and has a direction

pointing from the negative charge to the positive charge. An internal electric field is then produced between the positive and negative charges, pointing from the positive charge to the negative charge. This electric field will drive the photoexcited electrons and holes to opposite directions in the bulk of the ferroelectric photocatalyst, reducing the charge carrier recombination and promoting the solar energy conversion efficiency.

The second is the ferroelectric polarization induced band bending at the surface, which can act as thermal barrier to charge recombination. The spontaneous polarization will induce internal and external screening. Internal screening comes from the moving of free electrons and holes in the conduction and valence bands, and the accumulation of electrons and holes at opposite sides of the material will lead to surface band bending. Surface band bending will create the space charge region which can help to separate the carriers produced in or drifted to this area and can thus inhibit the recombination of charge carriers.

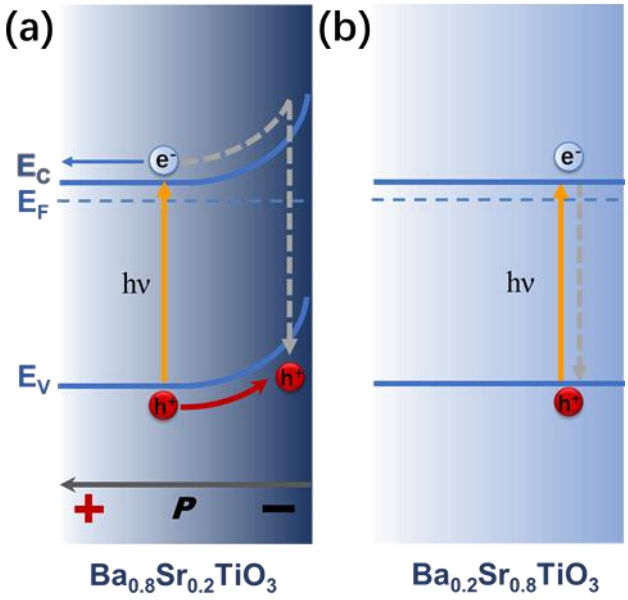


**Figure 6.12 Schematic illustration of migration of the photoexcited electrons and holes in (a) polar $Ba_{0.8}Sr_{0.2}TiO_3$ and (b) non-polar $Ba_{0.2}Sr_{0.8}TiO_3$.**

Figure 6.12 gives a schematic graph of the photoexcited charge carriers migration in the two $Ba_xSr_{1-x}TiO_3$ samples. For carriers generated in $Ba_{0.2}Sr_{0.8}TiO_3$ with non-polar structure, they have a much higher recombination chance since no barriers present within the photocatalyst. While in $Ba_{0.8}Sr_{0.2}TiO_3$, the polarization induced surface band bending will act as a thermal barrier to reduce the charge carrier recombination chances.

## 6.4. **Summary**

In this chapter, the effect of ferroelectricity on photocatalytic activity was investigated using barium strontium titanate single crystal particles as the target photocatalysts.

# Chapter 6

Nanoscale $Ba_xSr_{1-x}TiO_3$ particles have been synthesized successfully by a molten-salt method and their domain structure and polar/non-polar structure have been investigated.

It was demonstrated that the $Ba_xSr_{1-x}TiO_3$ samples processed at 750 ℃ are single-domain structure, and the $Ba_{0.8}Sr_{0.2}TiO_3$ has a polar structure at room temperature. The ferroelectric effect on photocatalytic activity is then evaluated in the single-grain-single-domain structured ferroelectric photocatalyst for the first time, without possible contribution from the domain walls.

The photocatalytic activity of the two $Ba_xSr_{1-x}TiO_3$ samples, $Ba_{0.8}Sr_{0.2}TiO_3$ with polar structure and $Ba_{0.2}Sr_{0.8}TiO_3$ with nonpolar structure, has been evaluated by photodegradation of Rh B. The results showed that the dye degradation rate was significantly enhanced by using $Ba_{0.8}Sr_{0.2}TiO_3$ with polar structure. The enhanced rate can be attributed to the internal electric field present in the polar structured ferroelectrics which can aid the separation of the photoexcited charge carriers and the ferroelectric spontaneous polarization induced band bending at the photocatalyst surface which can act as thermal barriers to reduce the carrier recombination. The photodegradation rate/activity of the BST powders are not comparable to the P 25 (commercialized $TiO_2$ powders, which have a powder size of ~ 20 nm and a total degradation of RhB in 5 minutes). The size difference can be a main contribution to their different photocatalytic

activity. Other possible factors, such as the catalytical activity, carrier diffusion length and mobility need a further study. It is worthy to note that, the focus of this work is to study the effect of polar structure on photocatalytic activity. The sample system has been made simple to carry out the mechanism study and thus no optimization of the materials has been made to achieve high photocatalytic activity. Based on our conclusion, the polar structure can contribute to the photocatalytic activity. Thus the $Ba_{0.8}Sr_{0.2}TiO_3$ with polar structure can be used for further improvement of its photocatalytic performance or other narrow band gap ferroelectrics can be utilized to achieve high photocatalytic performance catalysts.

In conclusion, we demonstrate the effect of ferroelectricity on photocatalytic activity in single-grain-single-domain structured ferroelectric photocatalysts. This provides the very original proof that it is the internal electric field within the single domain rather than other possible contributions such as the domain walls that enhances the photocatalytic efficiency. Besides, our study gives out the suggested characterization methods that are important in evaluating the ferroelectric effect on photocatalytic activity when using small sized ferroelectrics, which can benefit future studies of ferroelectric photocatalysts.

# Chapter 7 Conclusions and Future Work

## 7.1. Conclusions

Photocatalytic performance of three photocatalysts, $BiFeO_3$ thin films, $Bi_2Fe_4O_9$ thin films and nanoscale $Ba_xSr_{1-x}TiO_3$ powders have been investigated to study the effect of polar structure on photocatalytic properties of ferroelectric semiconductors.

### 7.1.1. The ambipolar photoelectrode performance of $BiFeO_3$ and the understanding of it

$BiFeO_3$ was chosen as the first target material in this research. A switchable photocurrent in $BiFeO_3$ photoelectrode was observed and the origin of the ambipolar behavior has been investigated by electrochemical method and explained from the perspective of unique electronic structure of the as-prepared $BiFeO_3$ film. Different from typical semiconductor photocatalysts, the Fermi level position of the as-prepared $BiFeO_3$ is not close to the minimum conduction band, which gives the possibility for formation of depletion region arising from both of the upward and downward band bending at the electrode/electrolyte solution interface. This provides it with the advantage of generating either anodic or cathodic photocurrents as a function of applied bias.

The derived band energy diagram shows that the conduction and valence bands of $BiFeO_3$ straddle the water redox potential, thus it is possible to promote either the hydrogen or oxygen evolution at one electrode just by tuning the applied potentials. Selective PEC oxidation or reduction based on one single material can be carried out, which is promising for application in solar energy conversion.

This finding can be adapted to understand and predict other semiconductor photoelectrodes with analogous ambipolar behavior. It also gives a hint of the way to prepare switchable photoelectrode materials in the future, especially for the compensated semiconductors.

### 7.1.2. Photoanode performance of $Bi_2Fe_4O_9$

$Bi_2Fe_4O_9$ thin film has been synthesized and applied as a photoanode for photoelectrochemical water oxidation for the first time in this research. It is of our interest to investigate the photocatalytic property of $Bi_2Fe_4O_9$ mainly because it is the most often reported bismuth ferrite besides $BiFeO_3$, and it is also a small band gap material with the ability to absorb visible light.

The $Bi_2Fe_4O_9$ photoelectrode exhibits an indirect bandgap of 2.05 eV and direct transition

at 2.80 eV leading to a strong visible light response. The measured band positions indicate it is able to conduct overall water splitting. A high photocatalytic activity under visible light illumination was demonstrated in the PEC tests. Possibility to further improve PEC performance of the $Bi_2Fe_4O_9$ photoelectrode has been studied. It shows that a hole injection barrier exists at the surface of the $Bi_2Fe_4O_9$ electrode and methods such as modification of surface states can be expected to enhance carrier extraction and promote the overall efficiency.

In conclusion, the $Bi_2Fe_4O_9$ combines strong light absorption, easy fabrication and good stability under illumination, making it a promising candidate for photoanodes application.

### 7.1.3. Investigation of the effect of ferroelectricity on photocatalytic activity in single-domain $Ba_xSr_{1-x}TiO_3$ (x = 0.2 and 0.8)

The effect of ferroelectricity on photocatalytic activity was investigated using barium strontium titanate particles with single-grain single-domain structure. $Ba_xSr_{1-x}TiO_3$ powders have been synthesized successfully by a molten-salt method and their domain structure and polar/non-polar structure have been studied. It was demonstrated that the $Ba_xSr_{1-x}TiO_3$ sample processed at 750 °C is a single-domain structure, and the $Ba_{0.8}Sr_{0.2}TiO_3$ has a polar structure at room temperature. Photocatalytic activity of the two

$Ba_xSr_{1-x}TiO_3$ samples, $Ba_{0.8}Sr_{0.2}TiO_3$ with polar structure and $Ba_{0.2}Sr_{0.8}TiO_3$ with nonpolar structure, was evaluated by photodegradation of Rh B. The degradation rate was significantly enhanced in $Ba_{0.8}Sr_{0.2}TiO_3$. This enhancement was attributed to the improved charge carriers separation due to the internal electric field present in the polar structured ferroelectrics.

In conclusion, the effect of ferroelectricity on photocatalytic activity in single-grain-single-domain structured ferroelectric photocatalysts has been demonstrated. This allows for the assessing of ferroelectric effect in a single domain scale, which can eliminate the possible contributions from domain walls. Besides, our study addressed the importance of the characterisation of nanoscale ferroelectrics due to the possible size effect and suggested several characterisation methods for assessment of the ferroelectric structure, which can benefit the future studies on ferroelectric photocatalysts.

## 7.2. **Future Work**

- Investigation of the controllable synthesis of $BiFeO_3$ film with different doping levels for use in practical photocatalytic systems, such as the selective photoreduction or photooxidation of water. The findings of this work show that the conductive type of the $BiFeO_3$ film can be adjusted through processing, thus can influence the associated

photocatalytic performance owing to the band bending variations at the semiconductor/electrolyte solution interface. Detailed work, for example the oxygen pressure and annealing time could be further done to find out the dependence of electronic structure of $BiFeO_3$ film on processing parameters for controllable film synthesis, building up a connection between the film synthesis and photocatalytic performance. The as-obtained $BiFeO_3$ electrodes with controllable p or n photoresponses can be expected to perform as the photoanode and photocathode simultaneously in one Photoelectrochemical cell for water splitting.

- Improvement of the photocatalytic performance of the $Bi_2Fe_4O_9$ photoelectrode. Since it is the first time for $Bi_2Fe_4O_9$ film synthesis and application as photoelectrode, optimization of the film synthesis such as the film thickness and annealing procedure could be conducted to achieve a better photocatalytic performance. Furthermore, as demonstrated in the previous work, one main limitation for the as-prepared $Bi_2Fe_4O_9$ electrode is the slow hole transfer kinetics at the electrode/electrolyte solution interface. Addition of co-catalysts such as Co-Pi on the photoelectrode surface is expected to enhance the photocurrents significantly. With the as-known suitable band gap diagram of the $Bi_2Fe_4O_9$ and an enhanced photocurrent, $Bi_2Fe_4O_9$ can be expected to be a promising candidate photocatalyst for practical water splitting.

- Improvement of the photocatalytic performance of the $Ba_xSr_{1-x}TiO_3$ powders. The molten salt synthesis procedure can be adjusted to obtain $Ba_xSr_{1-x}TiO_3$ powders with smaller/optimized grain size to achieve larger surface area, which can help to improve the photocatalytic activity by reduce the charge carrier transfer length. Also, surface modification of $Ba_xSr_{1-x}TiO_3$ by noble metals such as Ag or co-catalyst could be expected to promote the surface redox reactions and enhance the photocatalytic activity further.

# List of Publications and Presentations

## Publications

1. Cui, Y., Briscoe, J., **Wang, Y.**, Tarakina, N. V. & Dunn, S. Enhanced Photocatalytic Activity of Heterostructured Ferroelectric BaTiO3/α-Fe2O3 and the Significance of Interface Morphology Control. ACS Applied Materials & Interfaces (2017). 9, 24518-24526.[157]

2. Zhang, Ye, **Wang, Yaqiong**, Qi, Shaojun, Dunn, Steve, Dong, Hanshan, Button, Tim. Enhanced discharge energy density of rGO/PVDF nanocomposites: The role of the heterointerface. Applied Physics Letters (2018). 112, 202904.

3. **Yaqiong Wang**, Haixue Yan, Steve Dunn, Joe Briscoe. $Bi_2Fe_4O_9$ thin films as novel visible-light-active photoanodes for solar water splitting, to be submitted.

4. **Yaqiong Wang**, Joe Briscoe, Steve Dunn, Haixue Yan. Origin of the switchable photocurrent direction in $BiFeO_3$ thin films, to be submitted.

5. **Yaqiong Wang**, Bing Yang, Feng Li, Lars Riekehr, Zhen Zhang, Jianqi Qi, Haixue Yan. Effects of Ferroelectricity on Photocatalytic Activity of Single-Domain

$Ba_xSr_{1-x}TiO_3$ Crystals, to be submitted.

6. **Yaqiong Wang**, Amit Mahajan, Steve Dunn, Haixue Yan. Ferroelectricity in nanostructured single phase $BiFeO_3$ thin film on transparent substrate, to be submitted.

**Presentations**

1. Ferroic Photocatalyst for Photoelectrochemical Applications. ***Sustainable Functional Materials 2016, 5-6th April 2016, Spa Complex, Scarborough, UK***. **(Poster Presentation)**

2. Study of Ambipolar BiFeO3 Photoelectrodes - the Role of Oxygen Vacancies. ***Advanced Energy Materials 2017, 11-13th September 2017, University of Surrey, UK.*** **(Oral Presentation)**

## Reference


1 Li, J. & Wu, N. Semiconductor-based photocatalysts and photoelectrochemical cells for solar fuel generation: a review. *Catalysis Science & Technology* (2015). **5**, 1360-1384.

2 Fujishima, A. & Honda, K. Electrochemical Photolysis of Water at a Semiconductor Electrode. *Nature* (1972). **238**, 37.

3 Inoue, T., Fujishima, A., Konishi, S. & Honda, K. Photoelectrocatalytic reduction of carbon dioxide in aqueous suspensions of semiconductor powders. *Nature* (1979). **277**, 637.

4 Stafford, U., Gray, K. A. & Kamat, P. V. Photocatalytic degradation of organic contaminants: Halophenols and related model compounds. *Heterogeneous Chemistry Reviews* (1996). **3**, 77-104.

5 Hoffmann, M. R., Martin, S. T., Choi, W. & Bahnemann, D. W. Environmental Applications of Semiconductor Photocatalysis. *Chemical Reviews* (1995). **95**, 69-96.

6 Maeda, K. & Domen, K. Photocatalytic Water Splitting: Recent Progress and Future Challenges. *The Journal of Physical Chemistry Letters* (2010). **1**, 2655-2661.

7 Bott, A. W. Electrochemistry of Semiconductors. *Current Separations* (1998). **17**, 87-91.

8 Neamen, D. A. *Semiconductor physics and devices: basic principles*. (McGraw Hill, 2003).

9 Bott, A. W. Electrochemistry of Semiconductors. *Current Separations*. **17**, 87-91.

10 Mills, A. & Le Hunte, S. An overview of semiconductor photocatalysis. *Journal of Photochemistry and Photobiology A: Chemistry* (1997). **108**, 1-35.

11 Morrison, S. R. Electrochemistry at semiconductor and oxidized metal electrodes. (1980).

12 Li, L., Salvador, P. A. & Rohrer, G. S. Photocatalysts with internal electric fields. *Nanoscale* (2014). **6**, 24-42.

13 Zhang, Z. & Yates, J. T. Band Bending in Semiconductors: Chemical and Physical Consequences at Surfaces and Interfaces. *Chemical Reviews* (2012). **112**, 5520-5551.

14 Sivula, K. & van de Krol, R. Semiconducting materials for photoelectrochemical energy conversion. *Nature Reviews Materials* (2016). **1**, 15010.

15 Chen, Z. *et al.* Accelerating materials development for photoelectrochemical hydrogen production: Standards for methods, definitions, and reporting protocols. *Journal of Materials Research* (2011). **25**, 3-16.

16 Hisatomi, T., Kubota, J. & Domen, K. Recent advances in semiconductors for photocatalytic and photoelectrochemical water splitting. *Chemical Society Reviews* (2014). **43**, 7520-7535.

17 Grätzel, M. Photoelectrochemical cells. *Nature* (2001). **414**, 338.

18 Dotan, H., Sivula, K., Grätzel, M., Rothschild, A. & Warren, S. C. Probing the photoelectrochemical properties of hematite (α-Fe 2 O 3) electrodes using hydrogen peroxide as a hole scavenger. *Energy & Environmental Science* (2011). **4**, 958-964.

19 Zhang, L. *et al.* Quantifying and Elucidating Thermally Enhanced Minority Carrier Diffusion Length Using Radius-Controlled Rutile Nanowires. *Nano Letters* (2017). **17**, 5264-5272.

20 Abdi, F. F., Savenije, T. J., May, M. M., Dam, B. & van de Krol, R. The Origin of Slow Carrier Transport in BiVO4 Thin Film Photoanodes: A Time-Resolved Microwave Conductivity Study. *The Journal of Physical Chemistry Letters* (2013). **4**, 2752-2757.

21 Tayade, R. J. & Gandhi, V. *Photocatalytic Nanomaterials for Environmental Applications*. (Materials Research Forum LLC, 2018).

22 Albery, W. J. & Bartlett, P. N. The transport and kinetics of photogenerated carriers in colloidal semiconductor electrode particles. *Journal of the Electrochemical Society* (1984). **131**, 315-325.

23 Jang, J. S., Joshi, U. A. & Lee, J. S. Solvothermal Synthesis of CdS Nanowires for Photocatalytic Hydrogen and Electricity Production. *The Journal of Physical Chemistry C* (2007). **111**, 13280-13287.

24 Kenanakis, G. & Katsarakis, N. ZnO nanowires on glass via chemical routes: A prospective photocatalyst for indoors applications. *Journal of Environmental Chemical Engineering* (2014). **2**, 1416-1422.

25 Jung, H. S. *et al.* Photocatalysis Using GaN Nanowires. *ACS Nano* (2008). **2**, 637-642.

26 Hua, T. *et al.* Nano-photocatalytic Materials: Possibilities and Challenges. *Advanced Materials* (2012). **24**, 229-251.

27 Li, R. *et al.* Spatial separation of photogenerated electrons and holes among {010} and {110} crystal facets of BiVO4. *Nature Communications* (2013). **4**, 1432.

28 Gao, L. & Zhang, Q. Effects of amorphous contents and particle size on the photocatalytic properties of TiO2 nanoparticles. *Scripta Materialia* (2001). **44**, 1195-1198.

29 Zhang, Q., Gao, L. & Guo, J. Effects of calcination on the photocatalytic properties of nanosized TiO2 powders prepared by TiCl4 hydrolysis. *Applied Catalysis B: Environmental* (2000). **26**, 207-215.

30 Ajmal, A., Majeed, I., Malik, R. N., Idriss, H. & Nadeem, M. A. Principles and mechanisms of photocatalytic dye degradation on TiO2 based photocatalysts: a comparative overview. *RSC Advances* (2014). **4**, 37003-37026.

31 Pan, Y.-X. *et al.* Photocatalytic CO2 Reduction by Carbon-Coated Indium-Oxide Nanobelts. *Journal of the American Chemical Society* (2017). **139**, 4123-4129.

32 Bowen, C. R., Kim, H. A., Weaver, P. M. & Dunn, S. Piezoelectric and ferroelectric materials and structures for energy harvesting applications. *Energy & Environmental Science* (2014). **7**, 25-44.

33 Samara, G. A. in *Solid State Physics* Vol. 56 (eds Henry Ehrenreich & Frans Spaepen) 239-458 (Academic Press, 2001).

34 Ahn, C. H., Rabe, K. M. & Triscone, J.-M. Ferroelectricity at the Nanoscale: Local Polarization in Oxide Thin Films and Heterostructures. *Science* (2004). **303**, 488-491.

35 Yang, W. C., Rodriguez, B. J., Gruverman, A. & Nemanich, R. J. Photo electron emission microscopy of polarity-patterned materials. *Journal of Physics: Condensed Matter* (2005). **17**, S1415.

36 Glinchuk, M. D., Eliseev, E. A. & Stephanovich, V. A. The depolarization field effect on the thin ferroelectric films properties. *Physica B: Condensed Matter* (2002). **322**, 356-370.

37 Shun-Yu, C., New-Jin, H. & Hong-Yang, L. Transformation-Induced Twinning: The 90° and 180° Ferroelectric Domains in Tetragonal Barium Titanate. *Journal of the American Ceramic Society* (2006). **89**, 2177-2187.

38 Dipankar, G. *et al.* Domain Wall Displacement is the Origin of Superior Permittivity and Piezoelectricity in BaTiO3 at Intermediate Grain Sizes. *Advanced Functional Materials* (2014). **24**, 885-896.

39 Bhatnagar, A., Roy Chaudhuri, A., Heon Kim, Y., Hesse, D. & Alexe, M. Role of domain walls in the abnormal photovoltaic effect in BiFeO3. *Nature Communications* (2013). **4**, 2835.

40 Frost, J. M. *et al.* Atomistic Origins of High-Performance in Hybrid Halide Perovskite Solar Cells. *Nano Letters* (2014). **14**, 2584-2590.

41 Rojac, T. *et al.* Domain-wall conduction in ferroelectric BiFeO3 controlled by accumulation of charged defects. *Nature Materials* (2016). **16**, 322.

42 Catalan, G., Seidel, J., Ramesh, R. & Scott, J. F. Domain wall nanoelectronics. *Reviews of Modern Physics* (2012). **84**, 119-156.

43 Kneikamp, H. & Heywang, W. Depolarization effects in polycrystalline BaTi03. *Z. Angew. Phys* (1954). **6**, 385.

44 Frey, M. H. & Payne, D. A. Grain-size effect on structure and phase transformations for barium titanate. *Physical Review B* (1996). **54**, 3158-3168.

45 Zhao, Z. *et al.* Grain-size effects on the ferroelectric behavior of dense nanocrystalline BaTiO 3 ceramics. *Physical Review B* (2004). **70**, 024107.

46 Lin, S., Lü, T., Jin, C. & Wang, X. Size effect on the dielectric properties of BaTiO 3 nanoceramics in a modified Ginsburg-Landau-Devonshire thermodynamic theory. *Physical Review B* (2006). **74**, 134115.

47 Zhong, W. L., Wang, Y. G. & Zhang, P. L. Size effects on phase transitions in ferroelectric films. *Physics Letters A* (1994). **189**, 121-126.

48 Chattopadhyay, S., Ayyub, P., Palkar, V. R. & Multani, M. Size-induced diffuse phase transition in the nanocrystalline ferroelectric ${\mathrm{PbTiO}}_{3}$. *Physical Review B* (1995). **52**, 13177-13183.

49 Arlt, G., Hennings, D. & De With, G. Dielectric properties of fine-grained barium titanate ceramics. *Journal of applied physics* (1985). **58**, 1619-1625.

50 Shaw, T. M., Trolier-McKinstry, S. & McIntyre, P. C. The Properties of Ferroelectric Films at Small Dimensions. *Annual Review of Materials Science* (2000). **30**, 263-298.

51 Tan, Y. *et al.* Unfolding grain size effects in barium titanate ferroelectric ceramics. *Scientific Reports* (2015). **5**, 9953.

52 Zhong, W. L., Wang, Y. G., Zhang, P. L. & Qu, B. D. Phenomenological study of the size effect on phase transitions in ferroelectric particles. *Physical Review B* (1994). **50**, 698-703.

53 Smith, M. B. *et al.* Crystal structure and the paraelectric-to-ferroelectric phase transition of nanoscale BaTiO3. *J Am Chem Soc* (2008). **130**, 6955-6963.

54 Polking, M. J. *et al.* Ferroelectric order in individual nanometre-scale crystals. *Nature Materials* (2012). **11**, 700.

55 Kenji, U., Eiji, S. & Terukiyo, H. Dependence of the Crystal Structure on Particle Size in Barium Titanate. *Journal of the American Ceramic Society* (1989). **72**, 1555-1558.

56 Spanier, J. E. *et al.* Ferroelectric Phase Transition in Individual Single-Crystalline BaTiO3 Nanowires. *Nano Letters* (2006). **6**, 735-739.

57 Batra, I., Wurfel, P. & Silverman, B. Phase transition, stability, and depolarization field in ferroelectric thin films. *Physical Review B* (1973). **8**, 3257.

58 Hennings, D. & Schreinemacher, S. Characterization of hydrothermal barium titanate. *Journal of the European Ceramic Society* (1992). **9**, 41-46.

59 Wada, S., Tsurumi, T., Chikamori, H., Noma, T. & Suzuki, T. Preparation of nm-sized BaTiO3 crystallites by a LTDS method using a highly concentrated aqueous solution. *Journal of Crystal Growth* (2001). **229**, 433-439.

60 Marssi, M. E., Marrec, F. L., Lukyanchuk, I. A. & Karkut, M. G. Ferroelectric transition in an epitaxial barium titanate thin film: Raman spectroscopy and x-ray diffraction study. *Journal of Applied Physics* (2003). **94**, 3307-3312.

61 Nasby, R. & Quinn, R. K. Photoassisted electrolysis of water using a BaTiO3 electrode. *Materials Research Bulletin* (1976). **11**, 985-992.

62 Brady, J. J. & Moore, W. H. Actinoelectric Effects in Tartaric Acid Crystals. *Physical Review* (1939). **55**, 308-311.

63 Glass, A. M., Linde, D. v. d. & Negran, T. J. High-voltage bulk photovoltaic effect and the photorefractive process in LiNbO3. *Applied Physics Letters* (1974). **25**, 233-235.

64 Zenkevich, A. *et al.* Giant bulk photovoltaic effect in thin ferroelectric BaTiO 3 films. *Physical Review B* (2014). **90**, 161409.

65 Dubovik, E., Fridkin, V. & Dimos, D. The bulk photovoltaic effect in ferroelectric Pb(Zr, Ti)O3 thin films. *Integrated Ferroelectrics* (1995). **8**, 285-290.

66 Wei, J., Kui, Y. & C., L. Y. Bulk Photovoltaic Effect at Visible Wavelength in Epitaxial Ferroelectric BiFeO3 Thin Films. *Advanced Materials* (2010). **22**, 1763-1766.

67 Yang, S. Y. *et al.* Photovoltaic effects in BiFeO3. *Applied Physics Letters* (2009). **95**, 062909.

68 Butler, K. T., Frost, J. M. & Walsh, A. Ferroelectric materials for solar energy conversion: photoferroics revisited. *Energy & Environmental Science* (2015). **8**, 838-848.

69 Tiwari, D. & Dunn, S. Photochemistry on a polarisable semi-conductor: what do we understand today? *J Mater Sci* (2009). **44**, 5063-5079.

70 Yun, Y., Kampschulte, L., Li, M., Liao, D. & Altman, E. I. Effect of Ferroelectric Poling on the Adsorption of 2-Propanol on LiNbO3(0001). *The Journal of Physical Chemistry C* (2007). **111**, 13951-13956.

71 Dunn, S., Jones, P. M. & Gallardo, D. E. Photochemical Growth of Silver Nanoparticles on c- and c+ Domains on Lead Zirconate Titanate Thin Films. *Journal of the American Chemical Society* (2007). **129**, 8724-8728.

72 Giocondi, J. L. & Rohrer, G. S. Spatial Separation of Photochemical Oxidation and Reduction Reactions on the Surface of Ferroelectric BaTiO3. *The Journal of*

*Physical Chemistry B* (2001). **105**, 8275-8277.

73 Cui, Y., Briscoe, J. & Dunn, S. Effect of Ferroelectricity on Solar-Light-Driven Photocatalytic Activity of BaTiO3—Influence on the Carrier Separation and Stern Layer Formation. *Chemistry of Materials* (2013). **25**, 4215-4223.

74 Morris, M. R., Pendlebury, S. R., Hong, J., Dunn, S. & Durrant, J. R. Effect of Internal Electric Fields on Charge Carrier Dynamics in a Ferroelectric Material for Solar Energy Conversion. *Advanced materials* (2016). n/a-n/a.

75 Cao, D. *et al.* Switchable Charge-Transfer in the Photoelectrochemical Energy-Conversion Process of Ferroelectric BiFeO3 Photoelectrodes. *Angewandte Chemie* (2014). **126**, 11207-11211.

76 Liu, Q. *et al.* Enhanced ferroelectric photoelectrochemical properties of polycrystalline BiFeO3 film by decorating with Ag nanoparticles. *Applied Physics Letters* (2016). **108**, 022902.

77 Inoue, Y., Sato, K., Sato, K. & Miyama, H. Photoassisted water decomposition by ferroelectric lead zirconate titanate ceramics with anomalous photovoltaic effects. *The Journal of Physical Chemistry* (1986). **90**, 2809-2810.

78 Stock, M. & Dunn, S. Influence of the Ferroelectric Nature of Lithium Niobate to Drive Photocatalytic Dye Decolorization under Artificial Solar Light. *The Journal of Physical Chemistry C* (2012). **116**, 20854-20859.

79 Yang, S. Y. *et al.* Above-bandgap voltages from ferroelectric photovoltaic devices. *Nat Nano* (2010). **5**, 143-147.

80 Catalan, G. & Scott, J. F. Physics and Applications of Bismuth Ferrite. *Advanced Materials* (2009). **21**, 2463-2485.

81 Ji, W., Yao, K., Lim, Y.-F., Liang, Y. C. & Suwardi, A. Epitaxial ferroelectric BiFeO3 thin films for unassisted photocatalytic water splitting. *Applied Physics Letters* (2013). **103**, 062901.

82 Loh, L., Briscoe, J. & Dunn, S. Enhanced performance with bismuth ferrite perovskite in ZnO nanorod solid state solar cells. *Nanoscale* (2014). **6**, 7072-7078.

83 Li, Z. *et al.* Significant enhancement in the visible light photocatalytic properties of BiFeO3-graphene nanohybrids. *Journal of Materials Chemistry A* (2013). **1**, 823-829.

84 Yan, W., Bian, W., Jin, C., Tian, J.-H. & Yang, R. An Efficient Bi-functional Electrocatalyst Based on Strongly Coupled CoFe2O4/Carbon Nanotubes Hybrid for Oxygen Reduction and Oxygen Evolution. *Electrochimica Acta* (2015). **177**, 65-72.

85 Neaton, J. B., Ederer, C., Waghmare, U. V., Spaldin, N. A. & Rabe, K. M. First-principles study of spontaneous polarization in multiferroic BiFeO3. *Physical Review B* (2005). **71**, 014113.

86 Seshadri, R. & Hill, N. A. Visualizing the Role of Bi 6s “Lone Pairs” in the Off-Center Distortion in Ferromagnetic BiMnO3. *Chemistry of Materials* (2001). **13**, 2892-2899.

87 Ederer, C. & Spaldin, N. A. Weak ferromagnetism and magnetoelectric coupling in bismuth ferrite. *Physical Review B* (2005). **71**, 060401.

88 Lee, C.-C. & Wu, J.-M. Studies on leakage mechanisms and electrical properties of doped BiFeO3 films. *Electrochemical and solid-state letters* (2007). **10**, G58-G61.

89 Carvalho, T. & Tavares, P. Synthesis and thermodynamic stability of multiferroic BiFeO3. *Materials Letters* (2008). **62**, 3984-3986.

90 Wang, Y. & Nan, C.-W. Enhanced ferroelectricity in Ti-doped multiferroic Bi Fe O 3 thin films. *Applied Physics Letters* (2006). **89**, 052903.

91 Ravalia, A. *et al.* Role of defects in BiFeO3 multiferroic films and their local electronic structure by x-ray absorption spectroscopy. *Journal of Applied Physics* (2014). **116**, 153701.

92 Paudel, T. R., Jaswal, S. S. & Tsymbal, E. Y. Intrinsic defects in multiferroic BiFeO3 and their effect on magnetism. *Physical Review B* (2012). **85**, 104409.

93 Xu, Q. *et al.* The role of Bi vacancies in the electrical conduction of BiFeO 3: a first-principles approach. *Dalton Transactions* (2014). **43**, 10787-10793.

94 Daniel, S. *et al.* Revisiting the Optical Band Gap in Epitaxial BiFeO3 Thin Films. *Advanced Optical Materials* (2018). **6**, 1700836.

95 Poghossian, A. S., Abovian, H. V., Avakian, P. B., Mkrtchian, S. H. & Haroutunian, V. M. Bismuth ferrites: New materials for semiconductor gas sensors. *Sensors and Actuators B: Chemical* (1991). **4**, 545-549.

96 Zakharchenko, N. I. Catalytic Properties of the Fe2O3–Bi2O3 System in Ammonia Oxidation to Nitrogen Oxides. *Kinetics and Catalysis* (2002). **43**, 95-98.

97 Irshad, Z., Shah, S. H., Rafiq, M. A. & Hasan, M. M. First principles study of structural, electronic and magnetic properties of ferromagnetic Bi2Fe4O9. *Journal of Alloys and Compounds* (2015). **624**, 131-136.

98 Wang, H. *et al.* Visible Light Photocatalytic Activity of Bismuth Ferrites Tuned by Bi/Fe Ratio. *Journal of the American Ceramic Society* (2016). **99**, 1133-1136.

99 Ruan, Q.-J. & Zhang, W.-D. Tunable Morphology of Bi2Fe4O9 Crystals for Photocatalytic Oxidation. *The Journal of Physical Chemistry C* (2009). **113**, 4168-4173.

100 Sun, S., Wang, W., Zhang, L. & Shang, M. Visible Light-Induced Photocatalytic Oxidation of Phenol and Aqueous Ammonia in Flowerlike Bi2Fe4O9

Suspensions. *The Journal of Physical Chemistry C* (2009). **113**, 12826-12831.

101 Ezhilvalavan, S. & Tseng, T.-Y. Progress in the developments of (Ba,Sr)TiO3 (BST) thin films for Gigabit era DRAMs. *Materials Chemistry and Physics* (2000). **65**, 227-248.

102 Wang, J. *et al.* Investigation on the dielectric properties of (Ba, Sr)TiO3 thin films on hybrid electrodes. *Materials Chemistry and Physics* (2010). **121**, 28-31.

103 Fujisawa, J.-i., Eda, T. & Hanaya, M. Comparative study of conduction-band and valence-band edges of TiO2, SrTiO3, and BaTiO3 by ionization potential measurements. *Chemical Physics Letters* (2017). **685**, 23-26.

104 Zhou, L., Vilarinho, P. M. & Baptista, J. L. Dependence of the Structural and Dielectric Properties of Ba1-xSrxTiO3 Ceramic Solid Solutions on Raw Material Processing. *Journal of the European Ceramic Society* (1999). **19**, 2015-2020.

105 Wu, J. *et al.* Strong pyro-catalysis of pyroelectric BiFeO3 nanoparticles under a room-temperature cold-hot alternation. *Nanoscale* (2016). **8**, 7343-7350.

106 Neville, R., Hoeneisen, B. & Mead, C. Permittivity of strontium titanate. *Journal of Applied Physics* (1972). **43**, 2124-2131.

107 Lahiry, S. & Mansingh, A. Dielectric properties of sol–gel derived barium strontium titanate thin films. *Thin Solid Films* (2008). **516**, 1656-1662.

108 Mao, Y., Park, T.-J., Zhang, F., Zhou, H. & Wong, S. S. Environmentally Friendly Methodologies of Nanostructure Synthesis. *Small* (2007). **3**, 1122-1139.

109 Harwell, J. R. *et al.* Probing the energy levels of perovskite solar cells via Kelvin probe and UV ambient pressure photoemission spectroscopy. *Physical Chemistry Chemical Physics* (2016). **18**, 19738-19745.

110 Tauc, J., Grigorovici, R. & Vancu, A. Optical properties and electronic structure of amorphous germanium. *physica status solidi (b)* (1966). **15**, 627-637.

111 Das, R. S. & Agrawal, Y. K. Raman spectroscopy: Recent advancements, techniques and applications. *Vibrational Spectroscopy* (2011). **57**, 163-176.

112 Proksch, R. Piezoresponse Force Microscopy with Asylum Research AFMs.

113 Kim, Y. L. *et al.* Voltage-switchable photocurrents in single-walled carbon nanotube–silicon junctions for analog and digital optoelectronics. *Nature Photonics* (2014). **8**, 239.

114 Beranek, R. & Kisch, H. A Hybrid Semiconductor Electrode for Wavelength-Controlled Switching of the Photocurrent Direction. *Angewandte Chemie International Edition* (2008). **47**, 1320-1322.

115 Yasutomi, S., Morita, T., Imanishi, Y. & Kimura, S. A Molecular Photodiode

System That Can Switch Photocurrent Direction. *Science* (2004). **304**, 1944-1947.

116 Szaciłowski, K., Macyk, W. & Stochel, G. Light-Driven OR and XOR Programmable Chemical Logic Gates. *Journal of the American Chemical Society* (2006). **128**, 4550-4551.

117 Seger, B. *et al.* An n-Type to p-Type Switchable Photoelectrode Assembled from Alternating Exfoliated Titania Nanosheets and Polyaniline Layers. *Angewandte Chemie International Edition* (2013). **52**, 6400-6403.

118 Efrati, A. *et al.* Electrochemical Switching of Photoelectrochemical Processes at CdS QDs and Photosystem I-Modified Electrodes. *ACS Nano* (2012). **6**, 9258-9266.

119 Nozik, A. J. & Memming, R. Physical Chemistry of Semiconductor−Liquid Interfaces. *The Journal of Physical Chemistry* (1996). **100**, 13061-13078.

120 Rajeshwar, K. Fundamentals of Semiconductor Electrochemistry and Photoelectrochemistry.

121 Clark, S. J. & Robertson, J. Band gap and Schottky barrier heights of multiferroic BiFeO3. *Applied Physics Letters* (2007). **90**, 132903.

122 Palai, R. *et al.* β phase and γ−β metal-insulator transition in multiferroicBiFeO3. *Physical Review B* (2008). **77**, 014110.

123 Moniz, S. J. A. *et al.* A simple, low-cost CVD route to thin films of BiFeO3 for efficient water photo-oxidation. *Journal of Materials Chemistry A* (2014). **2**, 2922-2927.

124 Rajeshwar, K. Fundamentals of semiconductor electrochemistry and photoelectrochemistry. *Encyclopedia of electrochemistry* (2007). **6**, 1-53.

125 W., S. S. Roy Morrison: Electrochemistry at Semiconductor and Oxidized Metal Electrodes. Plenum Press, New York, London 1980. *Berichte der Bunsengesellschaft für physikalische Chemie* (1981). **85**, 621-622.

126 Kment, S. *et al.* Photoanodes based on TiO 2 and α-Fe 2 O 3 for solar water splitting–superior role of 1D nanoarchitectures and of combined heterostructures. *Chemical Society Reviews* (2017). **46**, 3716-3769.

127 Kim, T. W. & Choi, K.-S. Nanoporous BiVO4 photoanodes with dual-layer oxygen evolution catalysts for solar water splitting. *Science* (2014). 1245026.

128 Iandolo, B., Wickman, B., Zoric, I. & Hellman, A. The rise of hematite: origin and strategies to reduce the high onset potential for the oxygen evolution reaction. *Journal of Materials Chemistry A* (2015). **3**, 16896-16912.

129 Berglund, S. P. *et al.* Comprehensive Evaluation of CuBi2O4 as a Photocathode Material for Photoelectrochemical Water Splitting. *Chemistry of Materials* (2016). **28**, 4231-4242.

130 S., P. M., Néstor, G. & Kevin, S. Enhancing the Performance of a Robust Sol–Gel-Processed p-Type Delafossite CuFeO2 Photocathode for Solar Water Reduction. *ChemSusChem* (2015). **8**, 1359-1367.

131 Xu, Q. *et al.* The role of Bi vacancies in the electrical conduction of BiFeO3: a first-principles approach. *Dalton Transactions* (2014). **43**, 10787-10793.

132 Zhang, Z., Wu, P., Chen, L. & Wang, J. Density functional theory plus U study of vacancy formations in bismuth ferrite. *Applied Physics Letters* (2010). **96**, 232906.

133 Kunioku, H. *et al.* Strong hybridization between Bi-6s and O-2p orbitals in Sillen-Aurivillius perovskite Bi4MO8X (M = Nb, Ta; X = Cl, Br), visible light photocatalysts enabling stable water oxidation. *Journal of Materials Chemistry A* (2018). **6**, 3100-3107.

134 Kang, D., Park, Y., Hill, J. C. & Choi, K.-S. Preparation of Bi-Based Ternary Oxide Photoanodes BiVO4, Bi2WO6, and Bi2Mo3O12 Using Dendritic Bi Metal Electrodes. *The Journal of Physical Chemistry Letters* (2014). **5**, 2994-2999.

135 Zahedi, E., Xiao, B. & Shayestefar, M. First-Principles Investigations of the Structure, Electronic, and Optical Properties of Mullite-Type Orthorhombic Bi2M4O9 (M = Al3+, Ga3+). *Inorganic Chemistry* (2016). **55**, 4824-4835.

136 Park, H. S., Lee, C.-Y. & Reisner, E. Photoelectrochemical reduction of aqueous protons with a CuO|CuBi2O4 heterojunction under visible light irradiation. *Physical Chemistry Chemical Physics* (2014). **16**, 22462-22465.

137 Zhang, L., Baumanis, C., Robben, L., Kandiel, T. & Bahnemann, D. Bi2WO6 Inverse Opals: Facile Fabrication and Efficient Visible-Light-Driven Photocatalytic and Photoelectrochemical Water-Splitting Activity. *Small* (2011). **7**, 2714-2720.

138 Park, T.-J., Papaefthymiou, G. C., Moodenbaugh, A. R., Mao, Y. & Wong, S. S. Synthesis and characterization of submicron single-crystalline Bi2Fe4O9 cubes. *Journal of Materials Chemistry* (2005). **15**, 2099-2105.

139 Li, Y. *et al.* Photo-to-current response of Bi2Fe4O9 nanocrystals synthesized through a chemical co-precipitation process. *New Journal of Chemistry* (2012). **36**, 1297-1300.

140 Zhang, Y. *et al.* Photoelectrochemical response and electronic structure analysis of mono-dispersed cuboid-shaped Bi2Fe4O9 crystals with near-infrared absorption. *RSC Advances* (2014). **4**, 28209-28218.

141 Kirsch, A., Murshed, M. M., Schowalter, M., Rosenauer, A. & Gesing, T. M. Nanoparticle Precursor into Polycrystalline Bi2Fe4O9: An Evolutionary Investigation of Structural, Morphological, Optical, and Vibrational Properties. *The Journal of Physical Chemistry C* (2016). **120**, 18831-18840.

142 Ederer, C. & Spaldin, N. A. Influence of strain and oxygen vacancies on the magnetoelectric properties of multiferroic bismuth ferrite. *Physical Review B*

(2005). **71**, 224103.

143 Enriquez, E. *et al.* Oxygen Vacancy-Tuned Physical Properties in Perovskite Thin Films with Multiple B-site Valance States. *Scientific Reports* (2017). **7**, 46184.

144 Walter, M. G. *et al.* Solar Water Splitting Cells. *Chemical Reviews* (2010). **110**, 6446-6473.

145 Chen, X. Y. *et al.* Application of weak ferromagnetic BiFeO3 films as the photoelectrode material under visible-light irradiation. *Applied Physics Letters* (2007). **91**, 022114.

146 Quynh, L. T. *et al.* Self-Assembled BiFeO3-ε-Fe2O3 Vertical Heteroepitaxy for Visible Light Photoelectrochemistry. *Advanced Energy Materials* (2016). **6**, 1600686-n/a.

147 Dotan, H., Sivula, K., Gratzel, M., Rothschild, A. & Warren, S. C. Probing the photoelectrochemical properties of hematite ([small alpha]-Fe2O3) electrodes using hydrogen peroxide as a hole scavenger. *Energy & Environmental Science* (2011). **4**, 958-964.

148 Klahr, B., Gimenez, S., Fabregat-Santiago, F., Hamann, T. & Bisquert, J. Water Oxidation at Hematite Photoelectrodes: The Role of Surface States. *Journal of the American Chemical Society* (2012). **134**, 4294-4302.

149 Le Formal, F., Sivula, K. & Grätzel, M. The Transient Photocurrent and Photovoltage Behavior of a Hematite Photoanode under Working Conditions and the Influence of Surface Treatments. *The Journal of Physical Chemistry C* (2012). **116**, 26707-26720.

150 Dunn, H. K. *et al.* Tin doping speeds up hole transfer during light-driven water oxidation at hematite photoanodes. *Physical Chemistry Chemical Physics* (2014). **16**, 24610-24620.

151 Ma, Y., Pendlebury, S. R., Reynal, A., Le Formal, F. & Durrant, J. R. Dynamics of photogenerated holes in undoped BiVO4 photoanodes for solar water oxidation. *Chemical Science* (2014). **5**, 2964-2973.

152 Sivula, K. Metal Oxide Photoelectrodes for Solar Fuel Production, Surface Traps, and Catalysis. *The Journal of Physical Chemistry Letters* (2013). **4**, 1624-1633.

153 Chen, Y. *et al.* Ferroelectric domain structures in< 001>-oriented K0. 15Na0. 85NbO3 lead-free single crystal. *AIP Advances* (2015). **5**, 037117.

154 Rabuffetti, F. A. *et al.* Synthesis-Dependent First-Order Raman Scattering in SrTiO3 Nanocubes at Room Temperature. *Chemistry of Materials* (2008). **20**, 5628-5635.

155 Rørvik, P. M. *et al.* Influence of Volatile Chlorides on the Molten Salt Synthesis of Ternary Oxide Nanorods and Nanoparticles. *Inorganic Chemistry* (2008). **47**, 3173-3181.

156 Herrmann, J.-M. Heterogeneous photocatalysis: fundamentals and applications to the removal of various types of aqueous pollutants. *Catalysis today* (1999). **53**, 115-129.

157 Zhang, Y. *et al.* Enhanced discharge energy density of rGO/PVDF nanocomposites: The role of the heterointerface. *Applied Physics Letters* (2018). **112**, 202904.